Exploring metal hydrides

using autoclave and multi-anvil hydrogenations

by

Kati Puhakainen

A Dissertation Presented in Partial Fulfillment
of the Requirements for the Degree
Doctor of Philosophy

Approved May 2013 by the
Graduate Supervisory Committee:

Ulrich Häussermann, Co-Chair
Dong Seo, Co-Chair
John Kouvetakis
George Wolf

ARIZONA STATE UNIVERSITY

August 2013

ABSTRACT

Metal hydride materials have been intensively studied for hydrogen storage applications. In addition to potential hydrogen economy applications, metal hydrides offer a wide variety of other interesting properties. For example, hydrogen-dominant materials, which are hydrides with the highest hydrogen content for a particular metal/semimetal composition, are predicted to display high-temperature superconductivity. On the other side of the spectrum are hydrides with small amounts of hydrogen (0.1 – 1 at.%) that are investigated as viable magnetic, thermoelectric or semiconducting materials. Research of metal hydride materials is generally important to gain fundamental understanding of metal-hydrogen interactions in materials.

Hydrogenation of Zintl phases, which are defined as compounds between an active metal (alkali, alkaline earth, rare earth) and a p-block metal/semimetal, were attempted by a hot sintering method utilizing an autoclave loaded with gaseous hydrogen (< 9 MPa). Hydride formation competes with oxidative decomposition of a Zintl phase. The oxidative decomposition, which leads to a mixture of binary active metal hydride and p-block element, was observed for investigated aluminum (Al) and gallium (Ga) containing Zintl phases. However, a new phase Li_2Al was discovered when Zintl phase precursors were synthesized. Using the single crystal x-ray diffraction (SCXRD), the Li_2Al was found to crystallize in an orthorhombic unit cell (*Cmcm*) with the lattice parameters a = 4.6404(8) Å, b = 9.719(2) Å, and c = 4.4764(8) Å.

Increased demand for materials with improved properties necessitates the exploration of alternative synthesis methods. Conventional metal hydride synthesis methods, like ball-milling and autoclave technique, are not responding to the demands of finding new materials. A viable alternative synthesis method is the application of high pressure for the preparation of hydrogen-dominant materials. Extreme pressures in the gigapascal ranges can open access to new metal hydrides with novel structures and properties, because of the drastically increased chemical potential of hydrogen. Pressures up to 10 GPa can be easily achieved using the multi-anvil (MA) hydrogenations while maintaining sufficient sample volume for structure and property characterization.

Gigapascal MA hydrogenations using ammonia borane (BH_3NH_3) as an internal hydrogen source were employed in the search for new hydrogen-dominant materials. Ammonia borane has high gravimetric volume of hydrogen, and additionally the thermally activated decomposition at high pressures lead to a complete hydrogen release at reasonably low temperature. These properties make ammonia borane a desired hydrogen source material.

The missing member Li_2PtH_6 of the series of A_2PtH_6 compounds (A = Na to Cs) was accessed by employing MA technique. As the known heavier analogs, the Li_2PtH_6 also crystallizes in a cubic K_2PtCl_6-type structure with a cell edge length of 6.7681(3) Å. Further gigapascal hydrogenations afforded the compounds K_2SiH_6 and Rb_2SiH_6 which are isostructural to Li_2PtH_6. The cubic K_2SiH_6 and Rb_2SiH_6 are built from unique hypervalent SiH_6^{2-} entities with the lattice parameters of 7.8425(9) Å and 8.1572(4) Å, respectively. Spectroscopic analysis of hexasilicides confirmed the presence of hypervalent bonding. The Si-H stretching frequencies at 1550 cm^{-1} appeared considerably decreased in comparison with a normal-valent (2e2c) Si-H stretching frequencies in SiH_4 at around 2200 cm^{-1}. However, the observed stretching modes in hypervalent hexasilicides were in a reasonable agreement with $Ph_3SiH_2^-$ (1520 cm^{-1}) where the hydrogen has the axial (3e4c bonded) position in the trigoal bipyramidal environment.

ACKNOWLEDGMENTS

First, I would like to thank my advisor Dr. Ulrich Häussermann for all the support during these years. It has given me the opportunity to grow as a researcher. I would also like thank my Co-chair Dr. Dong Seo and Supervisory Committee members Dr. Kouvetakis and Dr. Wolf, for their guidance.

I am grateful to Dr. Thomas Groy for his invaluable assistance during these years. I would also like to thank Dr. Kurt Leinenweber for sharing his expertise in the high pressure field.

There are many past and present group members who helped me during these years. I would like to thank you all for your support. The high-pressure crew - Sumit, Kristina, Dr. Stoyanov, Dr. Sato and Dr. Wu – thanks for your kind words of encouragement. I would like to thank Dr. Johanna Nylén for sharing her expertise in the powder diffraction field, and for her friendship. Verina, thanks for listening to me and helping me through the tough days in the lab. Last, but not least, the special thanks to Daryn Benson for the theoretical calculations.

I'd also like to thank my close friends, especially SW Slam Ladies, for giving me a way to vent and recharge.

Lastly, I would like to thank my supporting family - Petri, Niko and Joni - thanks for your patience and showing me the right direction when I most needed it. I am also extremely grateful for the support from my grandparents, parents, sisters and other extended family members. Love you all.

TABLE OF CONTENTS

Page

LIST OF TABLES vii

LIST OF FIGURES viii

CHAPTER

1 INTRODUCTION 1

- 1.1 Introduction 1
- 1.2 Overview of Metal Hydrides 4
- 1.3 Binary (Metal/Semimetal) Hydrides 5
- 1.4 Ternary Hydrides 6
- 1.4.1 Hydrogenous Zintl Phases 7
- 1.4.1.1 Interstitial Hydrides 8
- 1.4.1.2 Polyanionic Hydrides 10
- 1.4.2 Complex Metal Hydrides 11
- 1.4.2.1 Main Group Systems 11
- 1.4.2.2 Transition Metal Systems 12
- 1.5 Gigapascal Hydrogenations 15
- 1.6 Summary 20
- 1.7 Outline 21
- 1.8 References 22

2 EXPERIMENTAL 28

- 2.1 Introduction 28
- 2.2 Synthesis 28
- 2.2.1 Precursor Synthesis 29
- 2.2.2 Low-pressure Hydrogenations 32
- 2.2.3 High-pressure Hydrogenations 33
- 2.3 Analysis 39
- 2.3.1 Powder X-ray Diffraction (PXRD) 39

2.3.2 Single Crystal X-ray Diffraction (SCXRD) 40

2.3.3 Spectroscopy 40

2.3.4 Thermal Analysis 42

2.3.5 Theoretical Calculations 42

2.4 References 43

3 HYDROGENOUS ZINTL PHASES 45

3.1 Introduction 45

3.2 Synthesis of Precursors 47

3.3 Characterization of a New Phase Li_2Al 48

3.4 Hydrogenation of Zintl Phase Containing Al or Ga 54

3.5 Conclusions 58

3.6 References 59

4 TRANSITION METAL HYDRIDES BY GIGAPASCAL HYDROGENATIONS 61

4.1 Introduction 61

4.2 Synthesis of Platinum Hexahydrides 63

4.2.1 Synthesis of Known Na_2PtH_6 to Optimize High-pressure Conditions 64

4.2.2 Synthesis of Li_2PtH_6 and $Li_2PtH_nD_{6-n}$ 65

4.3 Strucural Analysis of Li_2PtH_6 66

4.4 Conclusions 74

4.5 References 75

5 MAIN GROUP HYDRIDES BY GIGAPASCAL HYDROGENATIONS 79

5.1 Introduction 79

5.2 Hydrogen-dominant Materials Based on Silicon 79

5.3 Synthesis and Analysis of Hydrogen-dominant Materials Based on Silicon 80

5.4 Structural Analysis of K_2SiH_6 and Rb_2SiH_6 82

5.5 Result of NaSi Gigapascal Hydrogenations 94

5.6 Hydrogen-dominant Materials Based on Boron 98

5.7 Synthesis and Analysis of Li-B-H System 100

5.8 Conclusions 103

5.9 References 104

6 SUMMARY.. 109

6.1 Summary.. 109

6.2 References.. 111

COMPREHENSIVE REFERENCES……………………………………………………………………113

APPENDIX

A PXRD OF Li_2Al AND Li_9Al_4.. 127

B SCXRD REFINEMENT FOR Li_2Al and Li_9Al_4 129

C THEORETICAL CALCULATIONS OF SILICON HEXAHYDRIDES 132

D PERMISSION: FIGURE 1.8 139

E PERMISSION: FIGURE 1.9 141

F PERMISSION: FIGURE 2.7 143

G PERMISSION: FIGURE 4.6 145

H PERMISSION: Li_2Al 147

I PERMISSION: Li_2PtH_6 149

J PERMISSION: A_2SiH_6 (A = K or Rb] 151

LIST OF TABLES

Table Page

1.1 Calibration parameters.......... 37

3.1 Crystallographic data for Li_2Al and Li_9Al_4.......... 50

4.1 Li_2PtH_6 crystal data and structure refinement.......... 67

4.2 Vibrational Modes of A_2PtH_6 (A = alkali metal).......... 70

4.3 Pt-H T_{1u} streching and bending modes (cm^{-1}) for A_2PtH_6.......... 71

4.4 Decomposition products of Li_2PtH_6.......... 73

5.1 Collection of Si-H stretching and bending frequencies (IR/Raman).......... 86

5.2 Atomic charges according to Bader analysis.......... 90

LIST OF FIGURES

Figure Page

1.1 Structure of LiAl 8

1.2 Interstitial Zintl phase hydride $Ba_5Ga_6H_2$ 9

1.3 The orthorhombic $SrAl_2$ (a) and trigonal $SrAl_2H_2$ (b) 10

1.4 The tetragonal Na_3AlH_6 (a) and an orthorhombic $LiBH_4$ (b). 12

1.5 A cubic A_2PtH_6 (left) and an orthorhombic A_2PtH_2 (right) 14

1.6 The $[Pt_2H_9]^{2-}$ unit 15

1.7 Ammonia borane structure 16

1.8 Decompositon scheme of ammonia borane at high pressures 17

1.9 Chemical potential of molecular hydrogen as a function of pressure and temperature 18

2.1 Isothermal melt centriguation system with the sample space (a) and centrifugate space (b) 31

2.2 Stainless steel autoclave for low pressure hydrogenations 32

2.3 Sample and hydrogen source pellet arrangement 34

2.4 The MA 18/12 assembly parts 34

2.5 Schematic drawing of MA 18/12 assembly 35

2.6 Walker 6-8 type multi-anvil apparatus 36

2.7 Calibration of MA 18/12 assembly at three different pressure conditions 37

3.1 Zintl phase hydrogenation routes starting with Zintl phase precursor 46

3.2 Lithium-rich part of Li-Al phase diagram 48

3.3 Li_2Al (a - e) and Li_9Al_4 structures (f) 51

3.4 The DCS trace for Li_9Al_4 in which the red line represents heating and the blue line represents cooling trace 53

3.5 The DSC trace for Li_2Al in which the red line represents heating and the blue line cooling trace 53

3.6 A modified Li-Al phase diagram where a new phase, Li_2Al, is shown in grey 54

3.7 Density of states for Li_3Al_2 (a) and hypothetical Li_3Al_2H (b)............................ 55

3.8 Oxidative decomposition of Li_3Al_2 56

3.9 Structure of Ca_3Ga_5 (a) and hypothetical Ca_3Ga_5H (b)................................. 57

4.1 Experimental Na_2PtH_6 (5 GPa and 500 ºC) compared to the theoretical pattern (blue) of Na_2PtH_6 reported in literature 65

4.2 Rietveld fit for the x-ray pattern of Li_2PtH_6 (Cu$K\alpha_1$) 66

4.3 Li_2PtH_6 and Cs_2PtH_6 structures.. 67

4.4 The structural trends in relation to Pauling ionic radii 68

4.5 IR spectra of Na_2PtH_6 (a), Li_2PtH_6 (b) and "Li_2PtD_6" (c)................................. 71

4.6 The IR spectra of homoleptic K_2PtH_6, homoleptic K_2PtD_6 and heteroleptic $K_2PtH_nD_{6-n}$ 73

5.1 Rietveld fit to a PXRD pattern for a sample obtained from a reaction $2KH+Si+BH_3NH_3$ at 8.1 GPa and 400 ºC.. 83

5.2 Rietveld fit to a PXRD pattern for a sample obtained from a reaction $2KSi+BH_3NH_3$ at 7.6 GPa and 450ºC 83

5.3 PXRD pattern for a sample obtained from a reaction $2RbSi+BH_3NH_3$ at 5.8 GPa and 450ºC 84

5.4 Raman (lower) and IR (upper) spectrum of K_2SiH_6...................................... 85

5.5 Raman and IR spectrum of Rb_2SiH_6 86

5.6 The calculated phonon dispersion relations for K_2SiH_6 (left) and Rb_2SiH_6 (right) at the computed ZPE volume... 87

5.7 The electronic band structure of K_2SiH_6 and K_2SiF_6...................................... 88

5.8 Contour maps of MLWF's associated with Si-H and Si-F.............................. 89

5.9 Temperature-dependent energies for $K2SiH_6$ and Rb_2SiH_6........................... 91

5.10 Gibbs free energy (G) at ambient, 1 GPa, 5 GPa and 10 GPa pressures 93

5.11 The calculated phonon dispersion curves for Na_2SiH_6 94

5.12 NaSi hydrogenations at constant pressure 7.6 GPa with varied temperatures 95

5.13 NaSi hydrogenations at constant temperature 450 ºC with varied pressures . 96

5.14 Result of two independent hydrogenations of NaSi at 5.8 GPa and 450 ºC .. 97

5.15 The $LiBH_4$ phase diagram 99

5.16 Powder XRD patterns of LiH-B hydrogenated at 6 GPa and 600 ºC 101

5.17 IR spectum of hydrogenation at 6 GPa and 600 ºC LiH and B precursors ... 102

5.18 Raman spectrum of hydrogenation at 6 GPa and 600 ºC from LiH and B

precursors 103

CHAPTER 1

INTRODUCTION

1.1 Introduction

Metal hydride materials offer a wide range of properties, the most obvious being application as hydrogen storage materials. Hydrogen is the most abundant element on the Earth and provides a clean fuel source. However, energy potential of hydrogen has not been fully utilized. Hydrogen is gaseous in its natural state and storing a gas takes a large volume. This makes solid metal hydrides attractive and promising materials for storage applications. The DOE guidelines of hydrogen storage materials for on board applications are 5.5 wt.% gravimetric and 40 g/L volumetric content of hydrogen by 2017.[1]

Lightweight alkali metal hydrides are particularly promising hydrogen storage materials due to high volumetric and gravimetric content of hydrogen. The alanates and the borohydrides, like $NaAlH_4$ and $LiBH_4$, have a storage capacity of 7.4 wt.% and 18.3 wt.% of hydrogen, respectively.[2-4] The synthesis of sodium alanate by reacting mixtures of sodium hydride (NaH) and aluminum chloride ($AlCl_3$) in the presence of non-hydrous solvent has been known since the early-'60s.[5] The alanates and borohydrides can be prepared using wet mechanochemical synthesis in the presence of solvent, like tetrahydrofuran (THF). Often, a tedious isolation and purification process of the product is needed.[5.6] The first dry ball-milling synthesis for sodium alanate was reported in 2005 by Felderhoff[7], and for lithium borohydride by Friedrichs[8] in 2007. $LiBH_4$ was obtained at 700ºC and 15 MPa of H_2 from the reaction between elemental lithium and boron.[8] Subsequently, Friedrichs, et al.,[8] also noticed that when using LiB as a precursor (instead of the elements) $LiBH_4$ can be obtained at the lower temperature (450 ºC). The reversibility of alanates and borohydrides remains one of the most difficult challenges for their applications as hydrogen storage materials. In recent years, improving the reversibility and kinetic properties of $NaAlH_4$ and $LiBH_4$ has been extensively studied.[9-11] Ultimately, new and improved synthesis methods are needed for the direct synthesis of existing and/or new metal hydride materials. One viable option to consider is the synthesis of metal hydrides at high pressure conditions.

The benefits of high hydrogen pressures in the synthesis of metal hydrides can be demonstrated by using Mg_2FeH_6 as an example. Early ball-milling procedures afforded low yields with poor crystallinity.[12] The structure of the Mg_2FeH_6 (a cubic K_2PtCl_6-type) was originally characterized by Yvon, et al.,[13] in 1984. These authors applied hot sintering of a Mg/Fe powder mixture (2Mg:Fe) at ~ 500 ºC and H_2 pressures of 12 MPa for extended periods of time (up to 10 days). Compared to ball-milling, the crystallinity of obtained Mg_2FeH_6 was improved but the yield remained rather low (~ 50%).[13] It was not until 2010 when Retuerto, et al.,[14] were able to obtain highly crystalline Mg_2FeH_6 with yields in excess of 80% utilizing the piston-cylinder high-pressure technique. This synthesis was carried out at 2 GPa and ~ 800 ºC from the precursors MgH_2 and Fe enclosed in gold or platinum capsules. In addition to higher crystallinity, a shorter reaction time (1 hr) was achieved.[14] Oftentimes, shorter times are sufficient for a complete reaction because applying higher pressure and temperature improve the solubility of hydrogen. Another advantage of applying higher pressure is that higher reaction temperatures can be used without decomposing the product. The advantages of applying high pressure will be discussed in Chapter 1.5.

In addition to the promising nature of metal hydrides as fuel storage materials, they can also be used in electrochemical applications. As early as the 1970s, metal-hydrogen studies were initiated to find hydrogen containing alloys for electrochemical applications. One of the most intensively studied system in this respect was the formation of $LaNi_5$ hydride.[15] $LaNi_5$ adopts the hexagonal $CaCu_5$-type structure and can absorb up to 6 hydrogen atoms per formula unit at comparatively low temperatures. However, $LaNi_5H_6$ is a relatively expensive material with poor cyclic durability. Therefore, no commercial application as a battery material was established but $LaNi_5H_6$ served as an important prototype for developing hydride materials for electrochemical applications.[16,17] In the late 1980s research of nickel based alloys lead to the development of NiMH (M being a mixture of rare earth metals) as preferred material in the batteries[8,16,18] In recent years, NiMH batteries have largely been replaced by lithium-ion batteries.[19]

In the late 1960s, N.W. Ashcroft[20] proposed high-temperature superconductivity in metallic hydrogen. Metallic hydrogen has a predicted superconducting transition temperature (T_c)

around 230K which is most likely the highest value achievable by classic electron-phonon superconductivity.[21] The extreme threshold pressure for metallization of elemental hydrogen (400 GPa) may be overcome by “chemical precompression” in hydrogen-dominant metallic alloys while the underlying physical principles for achieving a high-T_c are retained.[22] Earlier PdH_x was the only known metal hydride displaying superconductivity and served as a model system for studying hydrogen-induced changes in properties.[23,24] When the amount of hydrogen (x) was increased from x = 0.75 to 1, the superconducting transition temperature of PdH_x increased from 0 to 9 K.[25] In recent times, densified molecular semimetal hydrides (e.g. SiH_4, GeH_4, AlH_3) have been identified as promising examples for “chemical precompression”.[26] Indeed, recently it was found that SiH_4 transforms to a metal at 50 GPa and becomes superconducting above 96 GPa at an appreciably high T_c of 17 K.[21,27]

Hydrogen-induced structural changes have been studied extensively in the past decades. The hydrogen-induced amorphization[28] and crystallization[29] of solids is well known. For example, hydrogenated silicon films synthesized by the plasma deposition technique are used in electronic and optoelectronic devices.[30,31] The hydrogen-induced crystallization of amorphous silicon is used to control the nanocrystalline and amorphous SiH ratio in SiH films. It has been shown that the ratio and the grain size dictate the structure and properties of SiH films.[29]

A wide range of structural variations and bonding schemes can be observed due to incorporation of hydrogen into intermetallic compounds. Corbett, et al.,[33-35] studied the phase stabilization effect of hydrogen impurities in Zintl phases which are main group intermetallic compounds between electropositive metals (alkaline, alkaline earth, rare earth) and p-element main group metals.[32] It was realized that some Zintl phase structures were characterized erroneously due to a hydrogen impurity that was not taken into account.[33,34] The hydrogen impurity was a result of either improper handling of chemicals or impurities in precursors which were left unnoticed.[34,35] An example are the M_5Pn_3-type compounds (M = Ca, Sr, Eu, Yb, Sm; Pn = As, Sb, Bi)[36]. These intermetallics adopt a hexagonal structure when absolutely hydrogen-free conditions are used in preparation. However, when hydrogen as an impurity is introduced, an orthorhombic $M_5Pn_3H_x$ is obtained. The amount of hydrogen impurity (x) for stabilizing the orthorhombic structure type is less than 1.[36]

Hydrogen-induced property changes include metal-semiconductor transitions which can be employed in switchable mirrors.[37] Further, main group hydrides display wide range of band gap sizes and therefore are potential materials as semiconductors.[38] Metal hydrides can also have applications as thermoelectric and magnetic materials.[39] In general, it is also important to increase the fundamental understanding of hydrogen-metal interactions to gain a deeper understanding of hydrogen-induced structure and property changes, and to understand metal-hydrogen bonding in novel hydrogen-dense materials. Experimental research is crucial in establishing relationships between the structure and properties.

This study will first focus on the hydrogenations of main group Zintl phases at low H_2 gas pressures. The overview of metal hydrides proceeds later in this chapter, and is combined with information regarding how these main group metal hydrides can be synthesized.

In the quest for novel hydrogen-dominant materials, gigapascal hydrogenations using the multi-anvil (MA) technique were initiated. In MA hydrogenations, an internal solid hydrogen source is employed. The advantage of gigapascal hydrogenation is the drastic increase of the hydrogen activity above 1 GPa[40] which offers new prospects for metal hydride synthesis. The experimental aspect of the MA technique will be explained in Chapter 2. Past developments and overview of ternary hydrides are discussed later in this chapter.

1.2 Overview of Metal Hydrides

There are several papers dedicated to the classification of metal hydrides, for example, by Yvon[41] and Bronger[42]. The overview of hydrides here is done to best describe the scope of this study. The binary hydrides are composed of the hydrogen and a non-hydrogen element. The ternary hydrides are composed of three elements, one of them being the hydrogen, and two others are non-hydrogen metal or semimetal elements.

1.3 Binary (Metal/Semimetal) Hydrides

Most of the elements form binary hydrides, except noble gases. Binary (metal/semimetal) hydrides can be divided into three different types - ionic, covalent and metallic hydrides - depending where the metal/semimetal element is located in the periodic table. The structural differences derive from the electronegativity differences between hydrogen and the metal/semimetal.

Ionic (salt-like) hydrides are formed between electropositive s-block metals (excluding Be) and rare earth elements, and hydrogen. These hydrides are of type MH or MH_2 like, for example, NaH and CaH_2. Rare earth hydrides can adopt type MH_3 binary hydrides. These hydrides can be synthesized directly by exposing the metallic element to hydrogen gas at elevated temperatures (up to 700 ˚C) and low pressures (< 2 MPa H_2). Typically, ionic hydrides of the s-block elements are thermally stable and display high decomposition temperatures.

Covalent hydrides form between an electronegative p-block main group metal and hydrogen. The general formula is $AH_{8\text{-}N}$, where N is the number of a main group, and 8-N is number of bonds that are formed. Usually, covalent hydrides are synthesized indirectly through solution chemistry and represent often volatile liquids and gases at ambient conditions. Dimeric and polymeric strctures, like BeH_2, BeH_3, AlH_3 and GaH_3, are rather common. Recently, the direct synthesis of AlH_3 was achieved by exposing elemental aluminum to H_2 atmosphere at extreme pressure (9 GPa) and 600ºC.[43]

Metallic hydrides are composed of a transition metal (d-block element) and hydrogen. The transition metal element (T), typically crystallizing in a close-packing of atoms, absorbs hydrogen into interstitial vacancies. Almost all 3d- and 4d-transition metals are known to form binary hydrides, except ruthenium.[44] These metallic hydrides typically display non-stoichiometric compositions, TH_x, in which the composition (x) varies depending on the pressure and the temperature conditions applied. At extreme pressures the compositions eventually reach the stoichiometric compositions like, for example, in case of titanium (TiH_2) and vanadium (VH_3) hydrides.[43] Often, a high hydrogen pressure (gigapascal range) is needed to achieve compound formation, except for palladium hydride.[43] Middle and late transition metal hydrides prepared at high pressures are not stable at ambient conditions but can be retained in a metastable state at atmospheric pressure by cooling to a liquid nitrogen temperature while under high pressure.[45,46]

As a peculiarity, in the early 1990s Fukai, et al.,[47] reported the formation of superabundant vacancies (SAV) in palladium hydride. In their study, the MA technique utilizing a solid hydrogen source ($LiAlH_4$) was employed. It was observed that higher pressures induced more SAVs and promoted the diffusion of the hydrogen into the Pd lattice. Superabundant vacancies in palladium formed at 5 GPa pressure and temperatures between 700 ºC to 800 ºC, and on subsequent cooling a separation into PdH and vacancy-ordered (Vac) structure occur.[47] The vacancy-ordered phase, $Pd_3VacH_{4,}$ corresponds to the Cu_3Au-type structure at elevated pressures and temperatures[47,48] The vacancy-ordered structure was recovered at ambient conditions and depleted of hydrogen in order to determine the vacancy concentration.[47] In addition to Pd, the formation of SAVs has been found in other transition metals, and is now considered one of the fundamental properties of transition metal hydrides. The mechanism behind the SAV formation is supposedly the trapping of H atoms by metal atom vacancies which are promoted by increased pressure.[48] The pressure induced changes in materials, including increased hydrogen corporation into metals, can possibly lead to novel and/or improved properties in hydrogen containing materials.

In this dissertation study, a major focus is in utilizing gigapascal MA hydrogenations in search of new hydrogen-dominant ternary transition metal and main group complexes which are discussed in Chapter 4 and Chapter 5, respectively.

1.4 Ternary Hydrides

Ternary metal hydrides are here classified into complex hydrides (consisting of homoleptic complexes with either transition or main group metal central atoms) and hydrogenous Zintl phases. The latter are further divided into interstitial and polyanionic metal hydrides. Hydrogenous Zintl phases are obtained from either the hydrogenation of Zintl phases, or sintering active metal hydrides with semimetals. These hydrides often form at low H_2 pressures and at slightly elevated temperatures.[41,42] As for complex hydrides those corresponding to main group systems, like alanates and borohydrides, are usually synthesized using wet mechanochemical synthesis[5,6] as described earlier in this chapter. Ternary transition metal hydrides can be prepared by hot sintering techniques. The applied hydrogen pressure is an important variable to achieve specific oxidation state of the transition metal central atom. MA technique can be used to provide high pressure conditions.

1.4.1 Hydrogenous Zintl Phases

As earlier discussed, hydrogenous Zintl phases are obtained from a direct hydrogenation of a Zintl phase, or sintering active metal hydrides with semimetals. A Zintl phase is defined as a compound between an electropositive s-block active metal (alkali, alkaline earth or rare earth metal) and an electronegative p-block metal/semimetal from groups 13 to 16.[32] Zintl phases typically display high melting points, brittleness and poor conductivity (salt-like properties), but they also have the luster of the metals.[49] Most Zintl phases are line compounds displaying a narrow range of homogeneity and fulfill the octet rule. Zintl phases are mostly diamagnetic and have the characteristic of normal valence compounds, meaning that there is a defined relationship between the chemical and electronic structure based on fulfilled octet rule.[49]

In the early 1930s, Eduard Zintl studied the structure and bonding of NaTl and observed that the thallium atoms form a tetrahedral diamond network,[32] in which a Na atom donates its valence electron to Tl, and thallium becomes isoelectronic to a group 14 element (Na^+Tl^-). Zintl also found that LiAl, LiGa, LiIn and NaIn crystallized in the same structure type as NaTl. In 1975, the structural characterization of LiAl by Kuriyama and Masaki[50] confirmed that LiAl displays a cubic NaTl-type structure with a cell edge of 6.37 Å (Z=8) (Figure 1.1).[49,50]

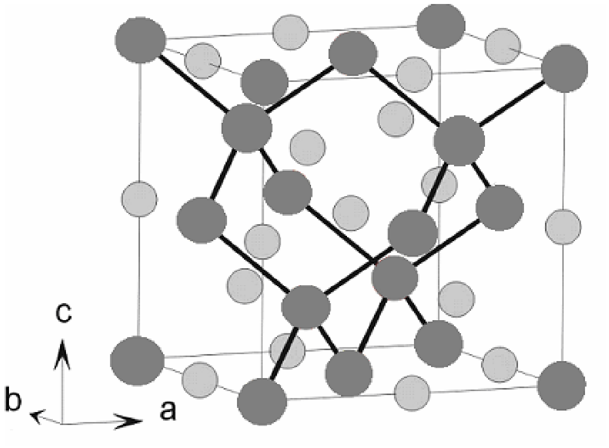

Figure 1.1. Structure of LiAl. Light grey and dark grey spheres represent Li and Al atoms, respectively.

Which role can hydrogen play in combination with Zintl phases? There are two scenarios for hydrogenous Zintl phases.[49] In the first case, an interstitial hydride is formed where hydrogen is exclusively coordinated by active metals and hydridic (H^-) hydrogen acts as an electron sink. In the second case, hydrogen is a covalently bonded ligand to a p-block element and thus part of the polyanionic framework. In both cases, the hydrogen content is fairly low. However, incorporating hydrogen into Zintl phases can induce interesting changes in the structure and properties which can lead to potential appications.[49]

1.4.1.1 Interstitial Hydrides

As mentioned above, in interstitial hydrides, the hydrogen is exclusively coordinated by the active metal component of the Zintl phase.[32,49] Interstitial hydrogenous Zintl phase can attain a completely different structure than the precursor, or the structure can hold but changes in the unit cell volume occur. The formation of interstitial hydrides can be considered as a first step in a series of oxidation reactions. Hydride formation competes with the oxidative decomposition of the Zintl phase eventually leading to a mixture of binary active metal hydride and p-block element. Actually, the oxidative decomposition is commonly observed in hydrogenations.[51]

A known interstitial hydride $Ba_5Ga_6H_2$ was first erroneously characterized as Ba_5Ga_6 in 1994.[52] In 1997, as a result of neutron diffraction studies, Henning, et al.,[53] revealed that Ba_5Ga_6 contains hydrogen as an interstitial impurity. The actual composition was determined to contain two hydrogen atoms per formula unit, $Ba_5Ga_6H_2$. This is a classic example of the structure stabilization by hydrogen impurity. The hydrogen-induced stabilization of Zintl phase hydrides is found to be present in many compounds, and has been extensively studied by Leon-Escamilla and Corbett.[38,54]

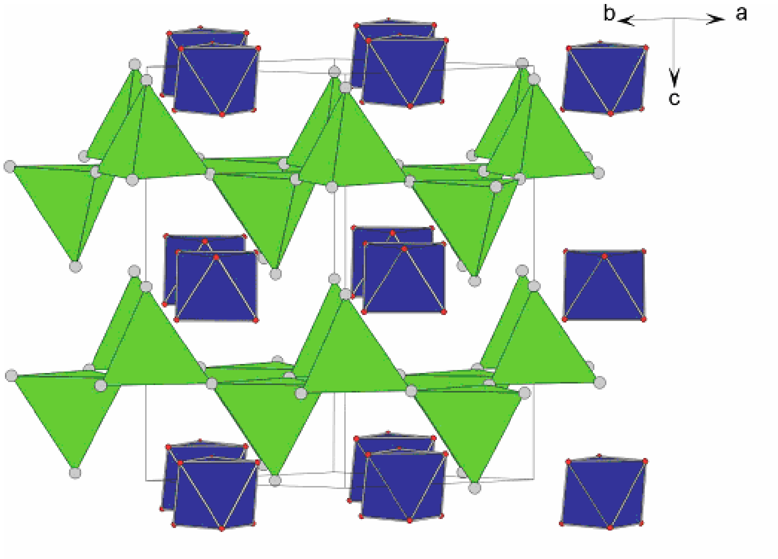

Figure 1.2. Interstitial Zintl phase hydride $Ba_5Ga_6H_2$. Polyanionic octahedral $[Ga_6]^{8-}$ clusters in blue, and HBa_4 tetrahedron in green.[53]

The $(Ba^{2+})_5(Ga_6)^{8-}(H^-)_2$ unit cell contains isolated polyanionic octahedral $[Ga_6]^{8-}$ clusters and tetrahedral HBa_4 units (Figure 1.2). Tetrahedral voids are created by the arrangement of Ba atoms, and a hydrogen atom occupies the center of each tetrahedron. Therefore, the hydrogen atom is exclusively coordinated by four s-block barium atoms. Each HBa_4 is corner-connected and organized in two layers.[53] Similarly, M_5Pn_3-type compounds (M = Ca, Sr, Eu, Yb, Sm; Pn = As, Sb, Bi)[35,55] adopt an orthorhombic $M_5Pn_3H_x$ when hydrogen impurity (x) less than 1 is absorbed. When absolutely hydrogen-free conditions are used in preparation these intermetallics adopt a hexagonal structure.

Other known interstitial hydrides include M_3TtH_2 (M = divalent Ca, Yb; Tt = Sn, Pb)[56] and Li_4TtH (Tt = Si, Ge)[57] which adopt an orthorhombic structure. Further examples of hydrogen-induced structures are CaSiH and $CaSiH_{1.2}$ which both can be completely dehydrogenated to CaSi.[58] Recently, it has been reported that SrSi, BaSi and EuSi incorporate substantially larger amounts of hydrogen than CaSi.[59]

1.4.1.2 Polyanionic Hydrides

In polyanionic hydrides, the hydrogen is covalently bonded to the p-block element, and belongs to an extended polyanionic network. These structures display bonds between p-elements (E-E), and additionally the terminating hydrogen bonds (E-H) exist.[49,51] Polyanionic hydrides can usually be synthesized from Zintl phases as precursors at low hydrogen pressures.

The first polyanionic hydride, $SrAl_2H_2$, was synthesized in 2000 by Gingl, et al.,[60] (Figure 1.3). A trigonal $SrAl_2H_2$ ($P\text{-}3m1$, Z=1)[60] was obtained from the hydrogenation of an orthorhombic $SrAl_2$ (*Imma*, Z=4)[61] precursor at low temperature (< 200 ºC) under 5 MPa of H_2.

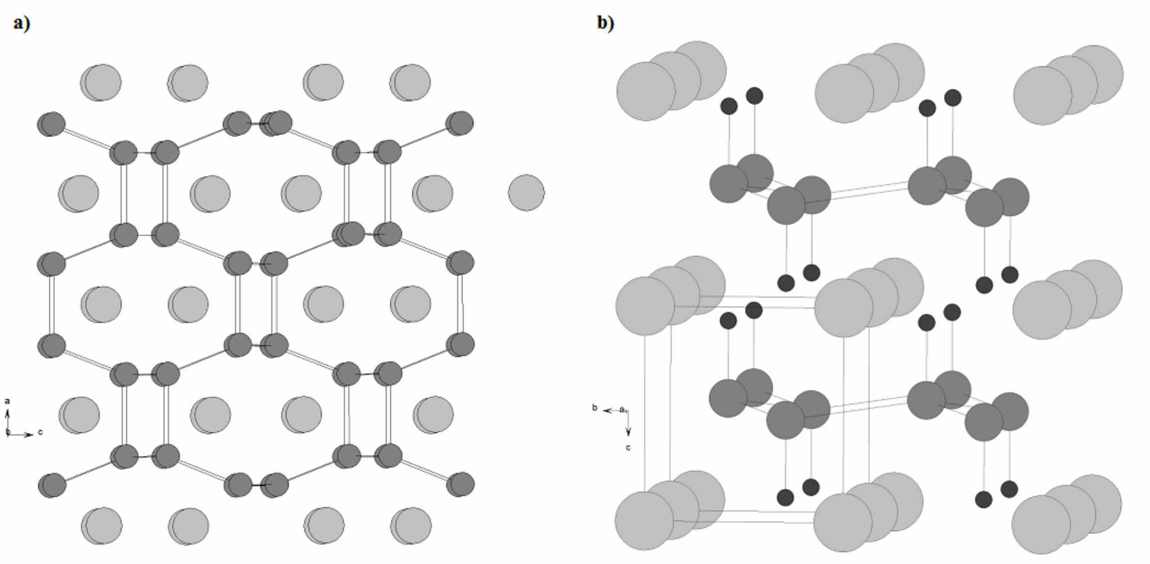

Figure 1.3. The orthorhombic $SrAl_2$ (a) and trigonal $SrAl_2H_2$ (b). Sr, Al and H atoms are noted in light grey, medium grey, and dark grey, respectively.

In an orthorhombic $Sr^{2+}[Al^{-}]_2$ each Al atom is connected to four other Al atoms in a 3-dimensional network. In trigonal $SrAl_2H_2$, the aluminum network has been reduced to a 2-dimensional polyanionic $[Al_2H_2]^{2-}$ network in which Al atoms are arranged as a puckered hexagonal layers.[60,61] The polyanionic $[Al_2H_2]^{2-}$structure has three Al-Al bonds, and one terminating Al-H bond. Strontium atoms are located between Al-Al layers to charge balance the structure.[61,62] Isostructural MGa_2H_2 (M = Sr, Ba) are also known.[63]

Recently, Fahlquist, et al.,[64] discovered a cubic $Rb_8Ga_5H_{15}$ structure displaying a new class of gallium hydride clusters with direct Ga-Ga bonds. A $Ga(Ga_3H_3)_4$ cluster has a neopentane $[C(CH_3)_4]$ molecular structure. $Rb_8Ga_5H_{15}$ is also the first compound where the polyanionic and interstitial features are combined in the same structure/compounds. In the same study, another hydrocarbon-like cluster-ion, $(RbGaH_2)_n$, adopting a polyethylene structure was discovered.[64]

1.4.2 Complex Metal Hydrides

In complex hydrides, the hydrogen ion (H^-) forms an isolated anionic complex with the transition metal, and the electropositive metal to the electropositive metal bonds do not coexist. Instead, the isolated anionic complexes are balanced by the electropositive (alkali or alkaline earth) metal positioned in between the complexes. The properties are mostly determined by the center atom, and the counter-ion contributes to the stability of the material.[41,42,65-67]

1.4.2.1 Main Group Systems

Alanates and borohydrides are the most studied main group complex hydrides due to their interest as hydrogen storage materials. As mentioned earlier, traditionally alanates and borohydrides have been synthesized using wet mechanochemical synthesis in the presence of a solvent. In recent years, a direct synthesis using elemental precursors has been established.[7,8] However, the reversibility of alanates and borohydrides remains one of the most difficult challenges for their applications as hydrogen storage materials. Improving the reversibility and kinetic properties of $NaAlH_4$ by doping using transition metals, and the doping of $LiBH_4$ by SrH_2 has been extensively studied.[9-11] Also, alanates with different alkali-metal-to-aluminum compositions exist. For example, Na_3AlH_6 which crystallizes in a tetragonal unit cell ($P2_1/n$) and displays octahedral $[AlH_6]^{3-}$ complexes.[68] The room temperature $LiBH_4$ crystallizes in an orthorhombic unit cell (*Pnma*) with tetrahedral $[BH_4]^-$ units (Figure 1.4).[69]

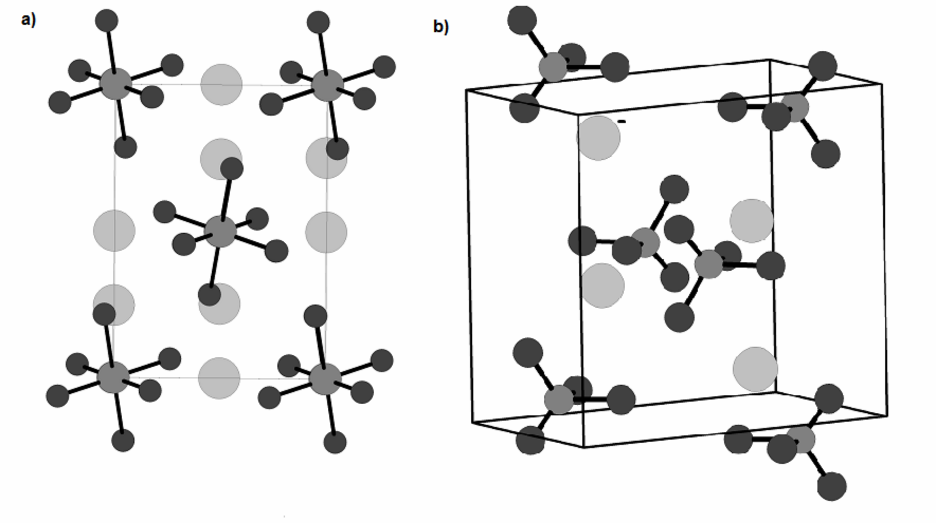

Figure 1.4. The tetragonal Na_3AlH_6 (a) and an orthorhombic $LiBH_4$ (b). Light grey circles represent alkali metals (Na, Li), medium grey represents Al or B, and dark grey represents hydrogen atom.

In the end, new and improved methods are needed for the synthesis in order to fully utilize the potential of these hydrides. Prospective high-pressure phases of $LiBH_4$ are predicted to display improved reversibility and kinetics (compared to ambient pressure phase).[70] Employing MA techniques for the synthesis of existing and/or new alanates and borohydrides is a viable option to gain access to these materials.

1.4.2.2 Transition Metal Systems

Transition metal systems can be divided into intermetallic compounds (hydrogen-in-metal systems) and complex hydrides. In intermetallic compound hydrides, the active s-block metal is combined with an early transition metal. A wide range of intermetallics with varied compositions of an active metal and early transition metal can be used. The hydrogen is diffused into interstitial vacancies in the metal lattice and intermetallic hydrides often display non-stoichiometric compositions in which the amount of hydrogen is dependent on the pressure and temperature applied in synthesis.[67] It has been observed that the Mn/Tc/Re triad in the periodic table has been the dividing line between the transition metals that form complexes and the ones that do not form complexes.[65] The early transition metals (left of the triad) form hydrogen-in-metal structures. In this study, the late transition metals (right of the triad) that form complex hydrides are investigated.[65]

In 1964, the first ternary complex hydride K_2ReH_9 was discovered by Knox.[71] It was synthesized from a solution at low yield, and the isolation and purification of the product was challenging. Two decades later Bronger, et al.,[72] were able to characterize the structure of K_2ReH_9 in which the isolated $[ReH_9]^{2-}$ anion complexes are balanced by K^+ cations.[71,72] The rhenium attains a high oxidation state of +VII.[72]

Ternary complex hydrides often are air and moisture sensitive materials, and therefore it is not surprising that it took two decades after wet synthesis of K_2ReH_9 for the ternary complex hydride research to fully start developing. In the 1980s, a solid state synthesis method in which the precursors are protected from air and moisture made it possible to discover new ternary hydride complexes.[73] Additionally, this new method eliminated the need for isolation and purification of the product, and also the yield and crystallinity of the products were improved.[73] At the same time, the analysis methods improved and several new structures were revealed.

In this new autoclave system developed by Bronger, et al., the high gaseous hydrogen pressures up to ~ 0.5 GPa were accessible.[73] Several autoclaves were connected in line and the alternating heating and cooling cycles were used to increase the H_2 pressure. Liquid nitrogen was employed for the cooling and the achieved pressure depended on the number of cooling and heating cycles. This ability to apply H_2 pressures up to 0.5 GPa lead to discovery of a series of new ternary hydrides.[72-74]

In 1984, the first ternary alkali metal/transition metal hydride complex, Na_2PtH_4, using above described autoclave method, was synthesized and characterized.[73] This finding was followed by the discovery of a homologous platinum ternary hydride series of A_2PtH_4 in which the alkali metal A is an element from Na to Rb.[74] In A_2PtH_4 structures, the platinum displays oxidation state +II.[74] Subsequently, new ternary metal hydrides were obtained for other transition metals in addition to platinum. For example, a series of palladium and more platinum ternary hydrides were synthesized displaying chemical formulas A_xTH_y where A is alkaline or alkaline earth metal, and T is either platinum or palladium.[41,75] A series of A_2TH_2 hydrides are known for alkali metals lithium and sodium in which the transition metal has zero oxidation state (T^0).[75] These structures are isotypical to Na_2HgO_2 oxide, and consist of linear $[TH_2]^{2-}$ complexes. Also, a series of A_2PtH_6

(K_2PtCl_6-type structure) with octahedral $[TH_6]^{2-}$ complexes (T^{+IV}) are known for alkali metals from sodium to cesium.[76,77] In Figure 1.5, the structures of a tetragonal A_2PtH_2 with a linear complex anion $[PtH_2]^{2-}$ and a cubic A_2PtH_6 with an octahedral complex anion $[PtH_6]^{2-}$ are shown. The A_2PtH_4 structure with a square planar complex anion $[PtH_4]^{2-}$ can be viewed as A_2PtH_6 structure with ⅔ of the hydrogen positions occupied.

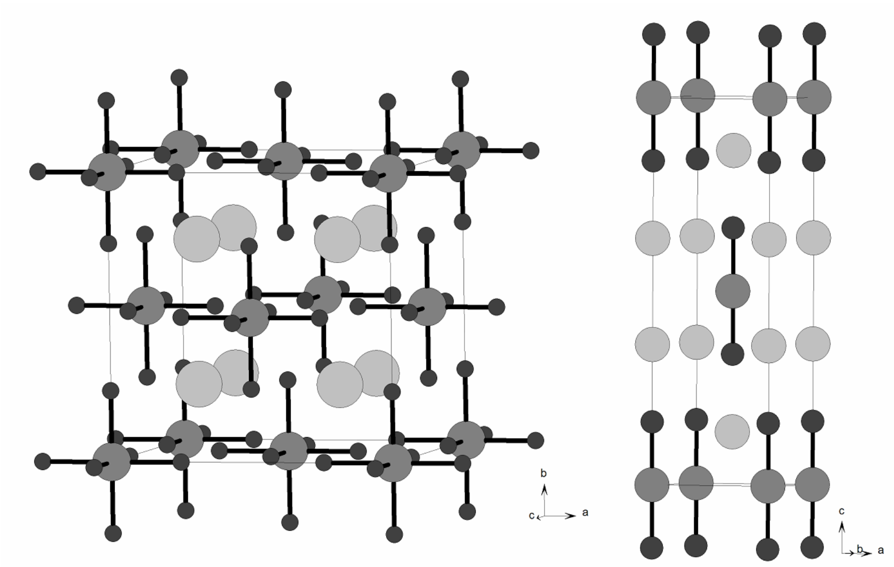

Figure 1.5. A cubic A_2PtH_6 (left) and an orthorhombic A_2PtH_2 (right). Alkali metal noted as light grey, Pt medium grey and H dark grey.

For the series A_2PtH_6 (A = Na to Cs), the lithium hexahydride complex was not found by Bronger, et al.,[76,77] Instead, $Li_5Pt_2H_9$ displaying a polynuclear $[Pt_2H_9]^{5-}$ was obtained. In anionic $[Pt_2H_9]^{5-}$ units, the Pt^{+II} atom is surrounded by five hydrogen atoms. One hydrogen atom acts as a bridge whereas four hydrogen atoms have a square-planar arrangement forming a planar pyramid polyhedron (Figure 1.6). Two planar pyramids are connected via common vertex and Pt atoms occupy the center of each pyramid. Lithium atoms occupy two different positions (4c 0, 0, 0; 16l 0.349, 0.849, 0.159).[78] It was thought that the $Li_5Pt_2H_9$ would be an intermediate en route to hexahydride and it was suggested that using even higher pressures would make the lithium hexahydride synthesis possible.[78]

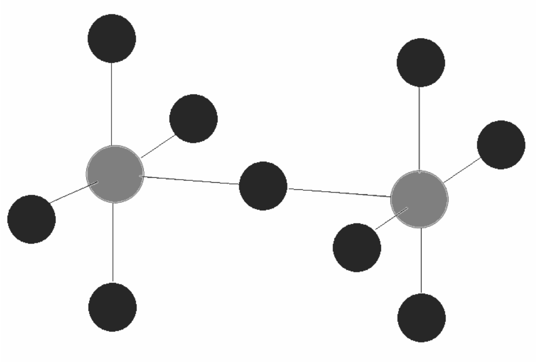

Figure 1.6. The $[Pt_2H_9]^{5-}$ unit. Platinum atoms are noted in medium grey and hydrogen in dark grey spheres.

In this study, the MA technique was used to apply high pressure conditions leading to a discovery of the lithium platinum hexahydride[79] which will be discussed in Chapter 4.

1.5 Gigapascal Hydrogenations

In this study, gigapascal hydrogenations were performed using a Walker-type multi-anvil (MA) apparatus.[80] Chapter 2 contains detailed information regarding the experimental setup. The principles related to gigapascal hydrogenations and differences between existing studies and this study are presented here.

Gigapascal MA hydrogenations are performed employing a solid internal hydrogen source. Suitable source material should display high hydrogen content, a low decomposition temperature, and release irreversibly hydrogen. Furthermore, decomposition products (other than hydrogen) should be inert towards the sample and products. In the past, alanates and borohydrides have been commonly used as an internal hydrogen source because they are easily available and have relatively high hydrogen content.[2-4] However, to lower the hydrogen release temperature a use of a catalyst is often required which increases the mass of used source. This, in turn, limits the used sample size in the experiments. For example, in the case of sodium borohydride the combined source and catalyst, which is used to lower the hydrogen release temperature, are bulky.[2]

$$NaBH_4 + 2\,Ca(OH)_2 \rightarrow NaBO_2 + 2\,CaO + 4H_2 \qquad \text{Equation 1.1}$$

Additionally, the use of the catalyst can also lead to the formation of undesired byproducts. For example, in addition to hydrogen release, sodium borohydride decomposes into $NaBO_2$ and CaO which can lead to unwanted reactions and/or hinder the analysis.

Binary hydrides, like AlH_3, are also used as internal hydrogen source.

$AlH_3 \rightarrow Al + 3/2\ H_2$ *Equation 1.2*

Even though alane is a simple two component hydride, it is not easy to synthesize. Another major disadvantage is the decomposition into reactive aluminum metal after the hydrogen release.[43]

In this research, ammonia borane (BH_3NH_3) is exclusively used as an internal hydrogen source. Ammonia borane has a large hydrogen capacity (~ 19 wt.%) and the properties and thermal behavior of ammonia borane are well studied because of its interest as a hydrogen storage material.[81] However, the hydrogen storage application of ammonia borane has not been successful because hydrogen absorption and desorption are irreversible which consequently is a desired property for the MA hydrogen source material. After irreversibly releasing the hydrogen, the ammonia borane decomposes into boron nitride (BN) which is rather inert.[81,82]

$BH_3NH_3 \rightarrow BN + 3H_2$ *Equation 1.3*

Ammonia borane is isostructural with gaseous ethane, C_2H_6. However, ammonia borane is a crystalline solid due to strong hydrogen bonding between positively polarized H bonded to nitrogen and negatively polarized H bonded to boron (dihydrogen-bonding) (Figure 1.7).

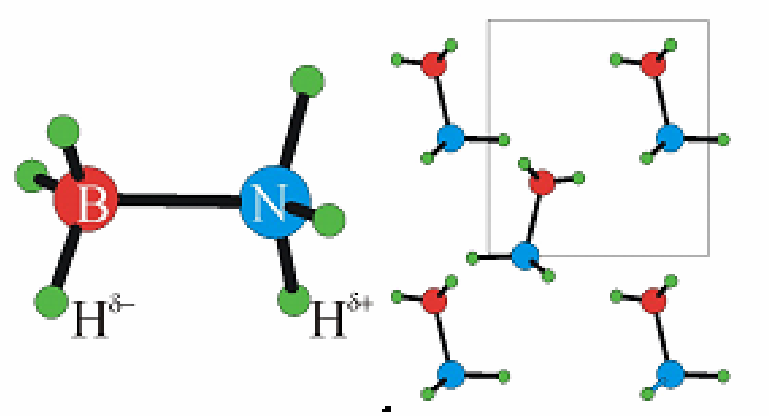

Figure 1.7. Ammonia borane structure.

The thermally activated decomposition of ammonia borane at high pressures has been studied by Nylen, et al.,[82] using a diamond anvil cell (DAC). The result is shown in Figure 1.8. Thermolysis under pressure releases almost the entire hydrogen content of the molecule in two distinct steps. The residual of the first decomposition is polymeric aminoborane, $(BH_2NH_2)_x$. The residual after the second decomposition correspond to macromolecular fragments of hexagonal BN where planar hexagon layers formed by B and N atoms are terminated by H atoms.[82] The salient feature is that at 1 GPa, temperatures around 200 ˚C are sufficient for a complete decompositions. Increasing pressure increases the temperature of both decomposition steps. At pressures between 9 GPa to 10 GPa, temperatures around 350 ˚C are required for a complete decomposition.[82] Compared to earlier mentioned hydrogen sources ($NaBH_4$ and AlH_3), the ammonia borane has favorable decomposition behavior at low temperatures and there is no need to use a catalyst. Also, ammonia borane decomposes into rather inert BN whereas the previously mentioned source materials have aluminum as a decomposition product after hydrogen release.

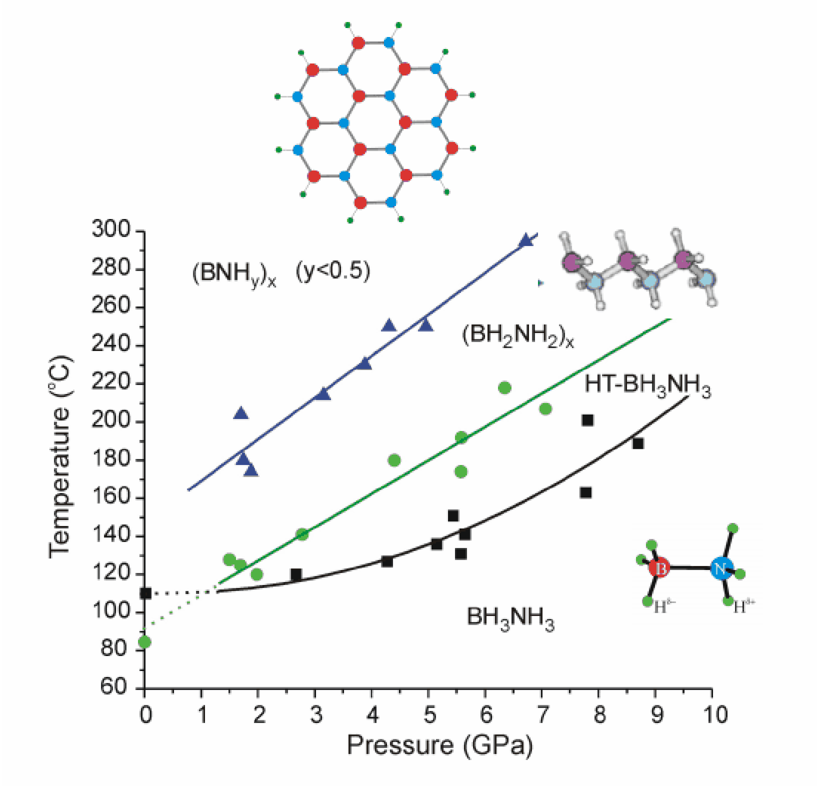

Figure 1.8. Decomposition scheme of ammonia borane at high pressures.[82]

The thermodynamic principles of high-pressure metal hydride synthesis have been described several times by Fukai et al.,[40,83-87] and Baranowski.[44] The critical point of hydrogen is well below room temperature (33K) and in all practical hydrogenation reactions hydrogen represents a gas/fluid.[88,89] Deviations from an ideal behavior are already noticeable above 0.1 MPa. There have been several attempts to establish the equation of state (EOS) for hydrogen at extreme conditions[84,90,91] which then allows derivation of relevant thermodynamical quantities. Although EOS in the literature differ, as a common feature, they yield a sharp increase of the chemical potential of hydrogen above around 1 GPa. Typically, the chemical potential decreases with increasing temperature but at above 1 GPa the chemical potential is almost independent from increase in temperature (Figure 1.9).[40] It is worth mentioning that in addition to applying high pressures, there are other ways to raise the chemical potential of hydrogen, even though those are out of the scope of this study. For example, electrolytic charging, where a sample constituting a cathode is placed into a solution, can be used. The excess voltage is applied to raise the chemical potential.[40]

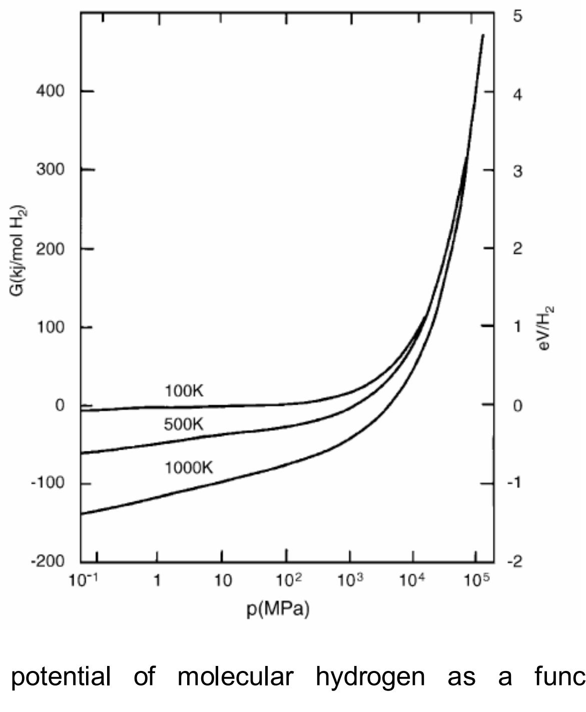

Figure 1.9. Chemical potential of molecular hydrogen as a function of pressure and temperature.[40]

Considering the simplest formation reaction of a metal hydride (Equation 1.4), the increased chemical potential of H_2 at high pressures may now allow access to hydrides MH possessing a high value in their standard chemical potential.[40,83]

$M + ½ H_2 = MH$ *Equation 1.4*

This is exemplified in the following: At low hydrogen pressures (P) hydrogen solubility (x) into a transition metal follows roughly Sieverts's Law.[83] It is defined as proportionality between hydrogen concentration [H] in the metal [M] and the square root of hydrogen pressure. The law holds for an ideal gas.[84]

$x = [H]/[M] \ \alpha \ \sqrt{P}$ *Equation 1.5*

Equilibrium condition for *Equation 1.4* is defined by the chemical potential of gaseous (or fluid) hydrogen H_2 (μ^l) and the chemical potential of a solid solution (μ^a).[84]

$½ \mu^l = \mu^a$ *Equation 1.6*

At high pressures above 1 GPa, the chemical potential of hydrogen does not follow the linear correlation indicated in the Sieverts's Law (*Equation 1.5)*.[40,83] Partial pressures (at high hydrogen pressures) are replaced by fugacity (f) which is a measure of the effective pressure (corrected for non-ideality).[40] For example, nickel metal has a hydrogen solubility $x = 4 \bullet 10^{-6}$ at 0.1 MPa (room temperature) which increases to x = 0.1 at 4 GPa.[84] This represents a tremendous deviation from Sievert's law and shows the remarkable effect of high hydrogen pressures which drastically enhance the solubility of hydrogen into solids.[39,83,84] A similar behavior is displayed by most middle and late transition metals; the synthesis of their (mono)hydrides requires gigapascal pressures.[44-46,91,92]

There are some further practical consequences from the thermodynamic principles of high pressure hydrogenations. The pressure dependency of the chemical potential is the molar volume (V).[40,84] Photon calculations to obtain electronic energy of the unit cell (E_{elec}) were performed in order to solve the Gibbs energy (G) for all materials.[90,93]

$G = E_{elec} + \Delta E - TS + P\Delta V$ *Equation 1.7*

Preceding calculations leading to Equation 1.7 are shown in Appendix C.

Another issue is temperature: According to van't Hoff's relation, for exothermic reactions (Equation 1.4, exothermic hydrides) a temperature increase will shift the equilibrium to the left side.[89] At the same time, the decomposition temperature of MH will increase with increasing pressure.[40,83] Therefore, exothermic hydrides which are metastable at ambient temperatures, may be synthesized at high hydrogen pressures.[83-87] Similarly, hydrogenation reactions can performed at higher temperatures (for achieving appreciable rates) when employing high hydrogen pressures.

Generally, the idea applying high pressures is to form a stable phase at high-pressure conditions and conserve it by quenching at isobaric conditions. After slowly decompressing the sample to ambient conditions, it has to be at least metastable (i.e. kinetically stable). Compared to the MA techniques, even higher pressures are easily accessible when applying DACs. However, DACs are rather observatory tools and not very useful for materials synthesis because of the very small sample size. Nevertheless, DAC studies can provide important insight into synthesis routes, intermediate phases and the quenchability of synthesis products. This insight can then be exploited in targeted MA synthesis experiments.

1.6 Summary

Advances in synthesis techniques led to the discovery of new hydrogen based materials. At first, metal hydrides were prepared at low hydrogen pressures and elevated temperatures, like the main group binary hydrides. In search of new hydrides, slightly higher pressures (usually less than 10 MPa) were applied, and as a result, the main group interstitial and polyanionic hydrides were produced.[52-54,60] In specialized autoclaves pressures up to 0.5 GPa were obtainable and access to a new family of transition metal complex hydrides was gained.[73] Even higher pressures (gigapascal range) might provide access to other classes of hydrides, in particular hydrogen-dominant materials. A hydrogen-dominant material is either a metal or mixed metal/semimetal hydride with the thermodynamically highest possible hydrogen content for a particular metal/semimetal composition.

In this study, gigapascal hydrogenations by MA technique, utilizing ammonia borane as an internal hydrogen source, is used to explore the possibilities of finding such materials. The interest in finding new hydrogen-dominant materials sparks from predictions that these materials can potentially have applications, for example, as high-temperature superconducting materials or as hydrogen storage materials.[26,21] The analysis and characterization of new and improved phases will provide fundamental information about bonding and structure in hydride materials which is needed to better understand the underlying concepts.

1.7 Outline

In Chapter 2, synthesis and analysis techniques of metal hydrides that are relevant to this dissertation are discussed. Synthesis techniques include the high-temperature flux which was used to produce intermetallic precursor phases for hydrogenation studies. Low pressure hydrogenations by hot sintering using autoclaves loaded with gaseous hydrogen (< 9 MPa) and gigapascal pressure (up to 10 GPa) hydrogenations empolying a solid hydrogen source are performed. Analysis of the samples has mostly been performed using x-ray diffraction (powder and single crystal) as well as spectroscopic (IR and Raman) methods. Thermal analysis was completed using the differential scanning calorimetry (DSC). Theoretical calculations provide supporting information to interpret the experimental results.

In Chapter 3, key results from hydrogenation of Zintl phases using the hot sintering technique employing autoclave, are presented. Instead of hydrogeneous Zintl phase formation, oxidative decomposition was observed. However, a new phase Li_2Al was discovered when Zintl phase precursors were synthesized.

Chapter 4 is focused on transition metal complex hydrides which were synthesized using gigapascal hydrogenations. Known Na_2PtH_6 was used to explore and optimize the high-pressure synthesis conditions. As a result a new homoleptic platinum hexahydride, Li_2PtH_6, was obtained. Attempts to synthesize a deuterium analog of Li_2PtH_6 resulted in the discovery of a heteroleptic $Li_2PtH_nD_{6-n}$.

In Chapter 5, the focus is on the main group complex hydrides synthesized by gigapascal hydrogenations. Hypervalent silicon hexahydrides, K_2SiH_6 and Rb_2SiH_6, were obtained and characterized for the first time. The hydrogenation studies of the Na-Si-H system will also be included. However, gigapascal hydrogenations of NaSi did not lead to a hypervalent hexahydride formation. Hexasilicide studies were followed by the attempts to obtain new borohydride phases (Li-B-H system) by gigapascal hydrogenations.

In Chapter 6, a short summary of all the experimental results will be presented. The discussion and main conclusions based on the findings in this study are also collected in this chapter.

1.8 References

1. http://www1.eere.energy.gov/hydrogenandfuelcells/storage/pdfs/targets_onboard_hydro_storage.pdf
2. Schüth, F.; Bogdanovic, B.; Felderhoff, M., *Chem. Commun*. **2004**, 2249
3. Sandrock, G.; Gross, K.; Thomas, G.; Jensen, C.; Meeker, D.; Takara, S., *J. Alloys Compd.* **2002**, 330-332, 696
4. Li, C.; Peng, P.; Zhow, D.W.; Wan, L., *Int. J. Hydrogen energy* **2001**, 36, 14512
5. Ashby, E.C.; Brendel, G.J.; Redman, H.E., *Inorg. Chem.* **1963**, 2, 499
6. Wang, J.; Ebner, A.D.; Ritter, J.A., *J. Phys. Chem.* **2007**, C111, 4917
7. Mellosta von Colbe, J.M.; Felderhoff, M.; Bogdanovic, B.; Schüth, F.; Weidenthaler, C., *Chem. Commun.* **2005**, 37, 4732
8. Friedrichs, O.; Buchter, F.; Borgschulte, A.; Remhof, A.; Zwicky, C.N.; Mauron, Ph.; Bielmann, M.; Züttel, A., *Acta Mater.* **2008**, 56, 949
9. Su, Z.; Ye, J.Y.; Zhou, R.F.; Duan, Y.S., *Rare Met. Mater. Eng.* **2012**, 41, 731
10. Bogdanovic, B.; Brand, R.A.; Marjanovic, A.; Schwickardi, M.; Tolle, J., *J. Alloys Compd.* **2000**, 302, 36
11. Liu, D.M.; Huang, W.J.; Si, T.Z.; Zhang, Q.A*., J. Alloys Compd*. **2013**, 551, 8
12. Ivanov, E.; Konstanchcuk, I.; Boldyrev, V., *J. Less-Common Met*. **1991**, 131, 25
13. Didisheim, J.J.; Zolliker, P.; Yvon, K.; Fischer, J.; Gubelmann, M.; *Inorg.Chem*. **1984**, 23, 1953

14. Retuerto, M.; Sánchez-Benítez, J.; Rodríguez-Canas, E.; Serafini, D.; Alonso, J.A., *Int. J. Hydrogen Energy* **2010**, 35, 7835

15. Van Vucht., J.H.N.; Kuijpers, F.A.; Bruning, H.C.A.M., *Philips Res. Rep*. **1970**, 25, 133

16. Hong, K., *J. Alloys Compd.* **2001**, 321, 307

17. Bittner, H.F.; Badcock, C.C., J*. Electrochem. Soc*. **1983**, 130, 193C

18. Bäuerlein, P.; Antonius, C.; Löffler, J.; Kümpers, J., *J. Power Sources* **2008**, 176, 547

19. Ozawa, K., *Solid State Ionics* **1994**, 69, 212

20. Ashcroft, N.W., *Phys. Rev. Lett.* **1968**, 21, 1448

21. Eremets, M.I.; Trojan, I.A.; Medvedev, S.A.; Tse, J.S.; Yao, Y., *Science* **2008**, 319, 1506

22. Ashcroft, N.W., *Phys. Rev. Lett.* **2004**, 18, 187002

23. Flanagan, T.B.; Oates, W.A., *Annu. Rev. Mater. Sci.* **1991**, 21, 269

24. Kohlmann, H.; Fischer, H.E.; Yvon, K., *Inorg. Chem.* **2001**, 40, 2608

25. Stritzker, B.; Buckel, W., *Z. Physik* **1972**, 257, 1

26. Kim, D.Y.; Scheicher, R.H.; Mao, H.-K.; Kang, T.W.; Ahuja, R., *PNAS* **2009**, 107, 2793

27. Strobel, T.A.; Goncharov, A.F.; Seagle, C.T.; Liu, Z.; Somayazulu, M.; Struzhkin, V.V.; Hemley, R.J., *Phys. Rev. B.* **2011**, 83, 144102

28. Aoki, K.; Nagano, M.; Yanagitani, A., *J. Appl. Phys*. **1987**, 62, 3314

29. Sriraman, S.; Agarwal, S.; Aydil, E.S.; Maroudas, D., *Nature* **2002**, 418, 62

30. Shah, A.; Torres, P.; Tscharner, R.; Wyrsch, N.; Keppner, H., *Science* **1999**, 285, 692

31. Street, R.A., *Phys. States Solid* **1998**, A166, 695

32. Zintl, E.; Woltersdorf, G., *Z. Angew. Phys. Chem*. **1935**, 41, 876

33. Leon-Escamilla, E.A.; Corbett, J.D., *J. Solid State Chem*. **2001**,159, 149

34. Leon-Escamilla, E.A.; Corbett, J.D., *J. Alloys Compd*. **1998**, 265, 104

35. Corbett, J.D.; Leon-Escamilla, E.A., *J. Alloys Compd*. **2003**, 356-357, 59

36. Leon-Escamilla, E.A.; Corbett, J.D., *J. Alloys Compd*. **1994**, 206, L15

37. Wang, Y.; Hua, W.; Qu, J.; Xie, L.; Li, X., *J. Int. Hydrogen Energy*, **2008**, 33, 7207

38. Karazhanov, S.Zh.; Ulyashin, A.G.; Ravindran, P.; Vajeeston, P., *EPL* **2008**, 82, 17006

39. Budziak, A.; Zurek, M.; Zukrowski, J.; Balanda, M.; Pacyna, A.; Czapla, M.; *J. Magn. Mater*. **2012**, 324, 735

40. Fukai Y., *J. Alloys Compd*. **2005**, 404-406, 7

41. Yvon, K., *J. Less-Common Met*. **1984**,103, 53

42. Bronger, W., *J. Alloys Compd*. **1995**, 229, 1

43. Saitoh, H.; Machida, A.; Katayama, Y.; Aoki, K., *App. Phys. Lett*. **2008**, 93, 151918

44. Baranowski, B., *J. Less-Common Met*. **1984**, 101, 115

45. Antonov, V.E., *J. Alloys Compd*. **2002**, 330-332, 110

46. Antonov, V.E.; Baier, M.; Dorner, B.; Fedotov, V.K.; Grosse, G.; Kolesnikov, A.I.; Ponyatovsky, E.G.; Schneider, G.; Wagner, F.E., *J. Phys.: Condens. Matter* **2002**, 14, 6427

47. Fukai, Y.; Okuma, N., *Phys. Rev. Lett*. **1994**, 73, 1640

48. Fukai, Y.; Sugimoto, H., *J. Phys.: Condens. Matter* **2007**,19, 436201

49. Kauzlarich, S.M., Ed. **1996**, *Chemistry, Structure, and Bonding of Zintl Phases and Ions*, VCH: New York,

50. Kuriyama, K.; Masaki, N., *Acta Cryst*. **1975**, B31, 1793

51. Häussermann, U.; Kranak, V.F.; Puhakainen, K., *Hydrogenous Zintl Phases: Interstitial Versus Polyanionic Hydrides, Structured and Bonding*, Ed. Fässler, T., **2011**, 139, pp.143-163

52. Fornasini, M.L.; Pani, M., *J. Alloys Compd*. **1994**, 205, 179

53. Henning, R.W.; Leon-Escamilla, E.A.; Zhao, J.T.; Corbett, J.D., *Inorg. Chem*. **1997**, 36, 1282

54. Corbett, J.D.; Leon-Escamilla, E.A., *J.Alloys Compd*. **2003**, 356-357, 59

55. Wu, H.; Zhou, W.; Udovic, T.J.; Rush, J.J.; Yilderim, T., *Chem. Phys. Lett.* **2008**, 460,432

56. Huang, B.Q.; Corbett, J.D., *Inorg. Chem.* **2007**, 36, 3730

57. Wu, H.; Hartman, M.R.; Udovic, T.J.; Rush, J.J.; Zhou, W.; Bowman, R.C.; Vajo, J.J., *Acta Cryst. B* **2007**, 63, 63

58. Wu, H.; Zhou, W.; Udovic, T.J.; Rush, J.J.; Yildirim, T., *Phys. Rev. Lett.* **2006**, 74, 224101

59. Armbruster, M.; Wörle, M.; Krumeich, F.; Nesper, R., *Z. Allg. Anorg. Chem.* **2009**, 635, 1758

60. Gingl, F.; Vogt, T.; Akiba, E., *J. Alloys Compd*. **2000**, 306, 127

61. Nagorsen, G.; Posch, H.; Schäfer. H.; Weiss, A., Z. *Naurforcshg*. **1969**, 24b,1191

62. Björling, T.; Noréus, D.; Häussermann, U., *J. Am. Chem. Soc*. **2005**, 128, 817

63. Lee, M.H.; Evans, M.J.; Daemen, L.L.; Sankey, O.F.; Häussermann, U., *Inorg. Chem.* **2008**, 47, 1496

64. Fahlquist, H.; Noreus, D.; Callear, S.; David, W.I.F.; Hauback, B.C., *J Am. Chem. Soc.* **2011**, 133, 14574

65. Parker, S.F., *Coord. Chem. Rev*. **2010**, 254, 215

66. Orimo, S.; Nakamori, Y.; Eliseo, J.R.; Züttel, A.; Jensen, C.M., *Chem. Rev*. **2007**, 107, 4111

67. King, R.B., *Coord. Chem. Rev*. **2000**, 200-202, 813

68. Huot, J.; Boily, S.; Güther, V.; Schulz, R., *J. Alloys Compd*. **1999**, 383, 304

69. Soulie, J.-Ph.; Reunadin, G.; Cerny, R.; Yvon, K., *J. Alloys Compd*. **2002**, 346, 200

70. Filinchuk, Y.; Chernyshov, D.; Nevidomskyy, A.; Dmitriev, V., *Angew. Chem. Int. Ed.* **2009**, 47, 529

71. Knox K.; Ginsberg, A.P., *Inorg. Chem.* **1964**, 3, 555

72. Bronger, W.; Brassard, L.; Müller, P.; Lebech, B.; Schultz, Th., *Z. Anorg. Allg. Chem.* **1999**, 625, 1143

73. Bronger, W,; Müller, P.; Schmitz, D., *Z. Anorg.Allg. Chem*. **1984**, 516, 35

74. Bronger, W.; Auffermann, G.; Müller, P., J*. Less-Common Met*. **1986**, 116, 9

75. Noreus, D.; Törnroos, K.W.; Börje, A.; Szabo, T.; Bronger, W.; Spittnak, H.; Auffermann, G.; Müller, P., *J. Less-Common Met.* **1988**, 139, 233

76. Bronger, W.; Auffermann, G., *Angew. Chem. Int. Ed*. **1994**, 33, 1112

77. Bronger, W.; Brassard, L.A., *Z. Anorg. Allg. Chem*. **1995**, 621,1318

78. Bronger, W.; Brassard, L.A., *Angew. Chem. Int. Ed*. **1995**, 34, 898

79. Puhakainen K.; Stoyanov, E.; Evans, M.J.; Leinenweber, K.; Häussermann, U., *J. Solid State Chem*. **2010**,183, 1785

80. Walker D.; Carpenter, M.A.; Hitch, C.M., *A. Mineral*. **1990**, 75, 1020

81. Wang, L.; Bao, K.; Meng, X.; Wang, X.; Jiang, T.; Cui, T.; Liu, B.; Zou, G., *J. Chem. Phys*. **2011**, 134, 024517

82. Nylen, J.; Sato, T.; Soignaard, E.; Yarger, J.L.; Stoyanov, E.; Häussermann, U., *J. Chem. Phys*. **2009**, 131, 104505

83. Fukai, Y., *J. Less-Common Met*. **1991**, 172-174, 8

84. Sugimoto, H.; Fukai, Y., *Acta Mat*. **1992**, 40, 2327

85. Fukai, Y.; Mizutani, M., *Mat. Trans*. **2002**, 43, 1019

86. Fukai, Y.; Mori, K.; Shinomiya, H., *J. Alloys Compd*. **2002**, 348, 105

87. Shizuku, Y.; Yamamoto, S.; Fukai, Y., *J. Alloys Compd*. **2002**, 336, 159

88. Eldik, R.; Klärner, F.-G., Ed. **2002** *High Pressure Chemistry,* Wiley-VCH, Wienheim, Germany

89. Holzapfel, W.B.; Isaacs N.S., Ed. **1997** *High-pressure Techniques in Chemistry and Physics*, Oxford University Press, New York

90. Hemmes, H.; Driessen, A.; Griessen, R., *J. Phys. C.: Solid State Phys.* **1986**, 19, 3571

91. Tkacz, M.; Litwiniuk, A., *J. Alloys Compd.* **2002**, 330-332, 89

92. Bashkin, I.O., *Z. Phys. Chem. Neue Folge* **1989**, 163, 469

93. Ke, X.; Tanaka, I., *Phys. Rev. B* **2005**, 71, 024117

CHAPTER 2

EXPERIMENTAL

2.1. Introduction

The ultimate goal of solid state chemistry is to synthesize materials in a manner that desired properties are achieved. The electronic structure of materials dictates the properties that synthesized materials display. Fundamental understanding of the structure and bonding in materials requires accurate analysis. In addition to the experimental work, the computational calculations can be used to predict, interpret and support the results.

Solid state synthesis is often carried out at high temperatures to improve diffusion in solids. Additionally, the diffusion can be improved by ensuring that atoms are at the shortest possible distance which can be achieved by pressing the samples into compact pellets. Long reaction times commonly accompany the high temperatures in order to overcome kinetic barriers en route to a complete reaction. If possible, the samples are heated above the liquid temperature which will greatly increase the diffusion rate.

Hydrogenations of solid state materials can be achieved in conventional autoclave techniques using pressurized hydrogen up to ~ 10 MPa.[1] Multi-anvil techniques, which employ an internal solid hydrogen source, allow for hydrogenations at gigapascal pressures.

Synthesis products were characterized using the x-ray diffraction to extract unit cell parameters and heavy atom positions. Spectroscopic methods, infrared and Raman, are techniques used to gain information about the bonding arrangements and the bonding strengths in materials. Differential Scanning Calorimetry (DSC) revealed information about the thermal events during heating and cooling cycles.

2.2. Synthesis

In this study two different techniques were employed in order to synthesize solid state precursors. When the desired product was directly approachable, a high temperature technique utilizing a metal ampoule was used.[2] If the desired product was not directly approachable, an isothermal melt centrifugation with a modified ampoule was used.[3] The details of these techniques proceed later in this chapter.

Low H_2 pressure (< 9 MPa) hydrogenations of the main group Zintl phases, and elemental hydrides that were not commercially available, were performed using the autoclave hydrogenations. In search of complex hydrides, the multi-anvil hydrogenations at gigapascal pressures were applied. The details of both hydrogenation techniques proceed later in this chapter.

2.2.1 Precursor Synthesis

Intermetallics and Zintl phases that were directly approachable, i.e. there were no competing reactions and/or phase boundaries in synthesis route, were synthesized at high temperatures employing a metal ampoule.[2] If starting materials were powders, the powders were pressed into a pellet before inserting into the ampoule. Employed ampoule materials were either niobium, tantalum or stainless steel.

Metal ampoules were closed from one end by crimping and flattening the end of the ampoule tightly before it was sealed by welding. After the reaction mixture was loaded into an ampoule, the other end of the ampoule was sealed in a similar manner. All sample preparation and welding was done in air and moisture-free conditions (argon atmosphere). The sealed ampoule was removed from the glovebox and inserted into a silica Schlenk-jacket which was connected to a vacuum/hydrogen line and evacuated before applying desired synthesis temperature using a tube furnace.

The lithium-aluminum system precursors, LiAl and Li_3Al_2, for the main group autoclave hydrogenations, were prepared in a manner described above. Stoichiometric amounts of Li (rods, 99.9%, Sigma Aldrich) and Al (pellets, 99.99%, Sigma Aldrich) metals were sealed into a niobium ampoule. The Li-Al mixture with 1 to 1 ratio (Li:Al) was heated at a rate of 300 ºC/hr to 750 ºC where it was kept for one hour. After one hour the sample was slowly (5 ºC/hr) cooled down to 650 ºC and quenched. Similarly, the Li_3Al_2 sample was prepared from stoichiometric amounts of Li and Al precursors. The sample was heated to 700 ºC (300 ºC/hr), and quenched after 12-hour dwelling time.

Alkali metal silicide precursors ASi (A = Na, K, Rb) for the multi-anvil hydrogenations were also prepared similarly by applying the high temperature flux utilizing an ampoule. The alkali metals were obtained from Sigma Aldrich with purity higher than 99.5% and all sample preparation was performed in Ar-filled glovebox (air/moisture < 0.3 ppm). Pelletized silicon (Sigma Aldrich, 99.99%) was sealed with stoichiometric amount of sodium and potassium into a stainless steel ampoule in order to synthesize NaSi and KSi, respectively. In case of RbSi synthesis an excess of 8% of Rb was used. Ampoules were heated at a rate of 300 ˚C/hr to target temperature (sodium 750 ºC, potassium 700 ˚C, rubidium 560 ˚C) and cooled down to room temperature (150 ˚C/hr) after a 14-hour dwell at target temperature.

When the desired synthesis product was not directly approachable, an isothermal melt centrifugation method with a large excess amount of one component and a modified ampoule with a sieve was empolyed.[3] At the end of the synthesis the excess melt was separated from the desired product by isothermal centrifugation. Sieves and lids were fabricated from the ampoule material sheet (0.5 mm thickness) by punching out disks which were formed into a cup shape. Electrical discharge machining (EDM) was used to fabricate the holes into a cup-shaped lid which transformed a lid into a sieve. Manually inserted sieve in the middle of the ampoule created a division of ampoule into two “chambers”: The centrifugate space (Figure 2.1b) where the excess melt was drained, and the sample space (Figure 2.1a) which was used to collect the desired product. Depending on how much centrifugate space was needed, the position of a sieve was adjusted. After a sieve was inserted into an ampoule, the ampoule was sealed from one end by welding a lid. The reaction mixture was loaded on top of the sieve into the sample “chamber”, and the other end of the ampoule was sealed by welding a lid.

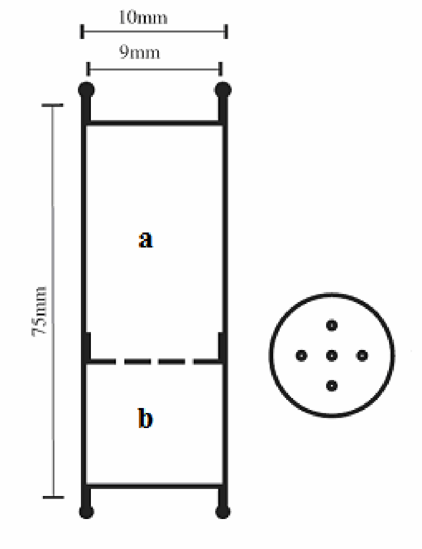

Figure 2.1. Isothermal melt centrifugation system with the sample space (a) and the centrifugate space (b).

The ampoule material has be able to withhold applied synthesis conditions, and be inert towards used precursors, products and surroundings. If a stainless steel ampoule was exposed to temperatures below ~ 850 ºC, a modified ampoule was directly inserted into a stainless steel container which was insulated by silica wool. In case of niobium or tantalum ampoule, it was inserted into silica tube which was sealed by melting the tube while under evacuation to protect the niobium and tantalum from reaction with hydrogen and/or oxygen in the air. After securing the Nb or Ta ampoule into silica tube, it was inserted into an insulated steel cylinder.

The insulated steel cylinder was placed into a box furnace in a way that the sample chamber faced the bottom and selected synthesis conditions were applied. The sample was kept above melting point for a short period of time before it was slowly cooled down to the target temperature. Long dwelling times (often days) at target temperature were needed to ensure that the equilibrium between melt and desired crystalline phase was achieved and an isothermal centrifugation (3000 rpm for three minutes) was performed to separate the excess melt from the product. In order to separate the excess melt, the stainless steel container was turned upside down in a manner that the sample chamber was on the top and centrifugate chamber was at the bottom. As a result, the excess melt was removed through the holes in a sieve and the product was secured on top of the sieve.

Using the isothermal melt centrifugation described above the lithium-rich precursors, Li_9Al_4 and Li_2Al, for the main group low-pressure hydrogenations were synthesized. Lithium (rods, 99.9%, Sigma Aldrich) and aluminum (pellets, 99.99%, Sigma Aldrich) were loaded into tantalum ampoules inside the glovebox under argon atmosphere (O_2 and H_2O < 0.3 ppm). A total mass of 1 g and compositions of $Li_{91.5}Al_{8.5}$ and $Li_{96}Al_4$ were used and the synthesis products were approached from the liquid side to avoid precipitation of any other phases. The reaction mixtures were heated to 450 ˚C (300 ˚C/hr) where they were kept for one hour. Mixtures $Li_{91.5}Al_{8.5}$ and $Li_{96}Al_4$ were slowly (5 ˚C/hr) cooled down to 290 ˚C and 210 ˚C, respectively, and kept at the target temperature for seven days, and centrifuged isothermally to separate the excess lithium melt from the product. The details of how synthesis conditions were selected are explained in Chapter 3.

2.2.2 Low-pressure Hydrogenations

Main group hydrogenations at low pressures were carried out utilizing a steel autoclave (Figure 2.2). A corundum crucible containing a sample pellet was placed into a stainless steel autoclave under air and moisture-free conditions (< 0.3 ppm) in argon-filled glovebox. Before the autoclave was removed from the glovebox, it was tightened to make sure the sample did not get exposed to air and/or moisture. The autoclave, connected to a vacuum and hydrogen line, was evacuated before heating using a tube furnace. Up to 9 MPa of hydrogen gas was released into the autoclave to initiate the hydrogenation reaction.

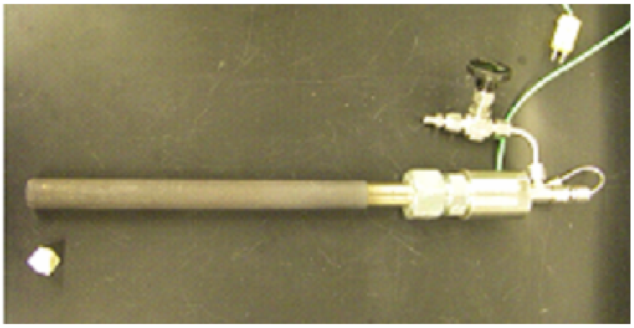

Figure 2.2. Stainless steel autoclave for low pressure hydrogenations.

In addition to the main group hydrogenations, the autoclave technique was used to synthesize elemental hydride precursors which were not commercially available. Alkali metal hydrides, KH and RbH, were prepared by placing 1 g of alkali metal into corundum crucible in air and moisture-free conditions under argon atmosphere. Potassium with 99.5% purity and rubidium with 99.6% purity from Sigma Aldrich were used. The autoclave was heated to 500 ˚C (RbH) and to 520 ˚C (KH), and filled with H_2 (1.5 MPa). During 24-hour dwell at the target temperature, the autoclave was occasionally shaken. Similarly, LiD was obtained using D_2 instead of H_2.

The main group hydrogenations of Li-Al system were carried out at varied temperatures (100 to 300 ºC), dwell times (minutes to hours) and hydrogen pressures (0.5 to 9 MPa). The results and exact synthesis conditions are shown in Chapter 3.

2.2.3 High-pressure Hydrogenations

A Walker-type[4] 6-8 multi-anvil apparatus (MAA) using an 18/12 assembly developed by Stoyanov, et al.,[5] was exploited in the high-pressure hydrogenations. In the 18/12 assembly, a magnesium oxide (MgO) octahedron with an octahedral edge length (OEL) of 18 mm was used as a pressure medium.[5] The trunctuated edge length (TEL) dimension of 12 mm refers to a tungsten carbide cube trunctuation on eight inner anvils[5] which create an octahedral hollow space where the pressure medium is nested. The six outer steel anvils form a cubic space where the inner anvils are positioned.

The preparation of the sample capsule (NaCl) was performed in an Ar-filled glovebox (air and moisture-free conditions). A hollow space inside the NaCl capsule (1.00 mm wall thickness) has an inside diameter of 4.00 mm and a length of 6.5 mm. This hollow space was filled with the sample pellet which was sandwiched between two internal ammonia borane (BH_3NH_3) hydrogen source pellets (Figure 2.3). Subsequently, the NaCl capsule was sealed by tightly compressing salt grains on top of the capsule using a pressing tool.

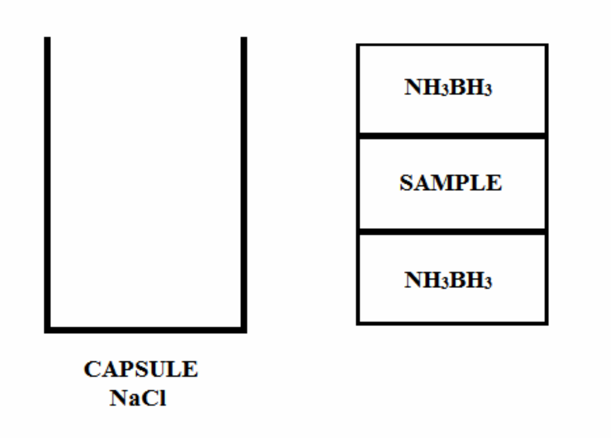

Figure 2.3. Sample and hydrogen source pellet arrangement.

The sealed capsule was removed from the glovebox in order to load the pressure medium. Loading of the MgO pressure medium consist of surrounding the sample capsule with graphite furnace and thermally insulating it with zirconia. To accurately control the synthesis temperature was achieved by adding a thermocouple to the assembly. The parts needed in the 18/12 assembly are shown in Figure 2.4.

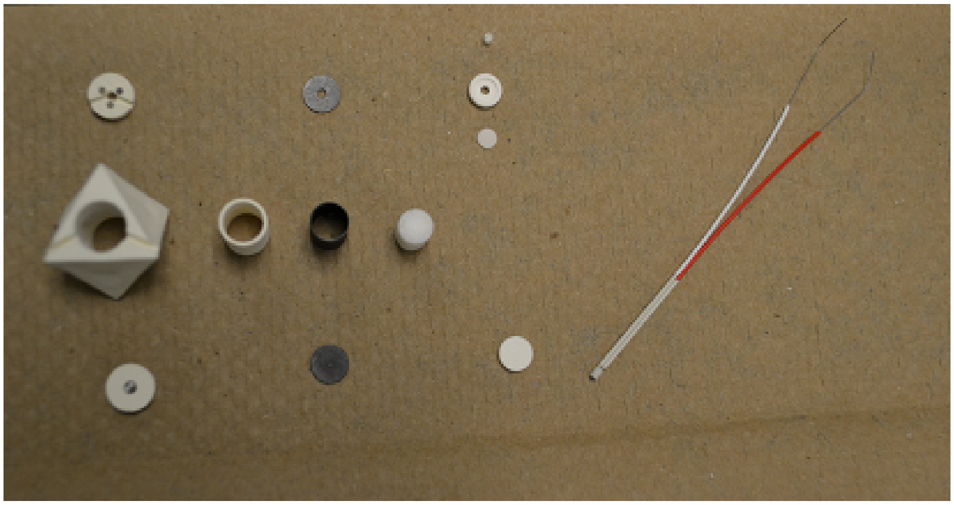

Figure 2.4. The MA 18/12 assembly parts.

Zirconia end-sleeve, with a hole for molybdenum (Mo) lead, was used to close the bottom end of a cylindrical hole in the octahedron. Thermally insulating zirconia sleeve was inserted into the cylindrical opening before a graphite furnace disc (0.38mm thickness) and graphite sleeve were added. Next, a thin MgO bottom disc was added before the sealed salt capsule was positioned inside a graphite furnace. On top of the salt capsule, a thin (0.4 mm) protective alumina disc surrounded by a MgO ring was inserted before a MgO top disc with a hole for the thermocouple was added. Above mentioned parts were positioned inside a graphite furnace which was closed by adding a graphite disc with a hole for a thermocouple. A zirconia top end-sleeve, which had holes for Mo leads and for thermocouple wires, was used to complete the magnesia octahedron. Figure 2.5 shows schematic drawing of MA 18/12 assembly parts.

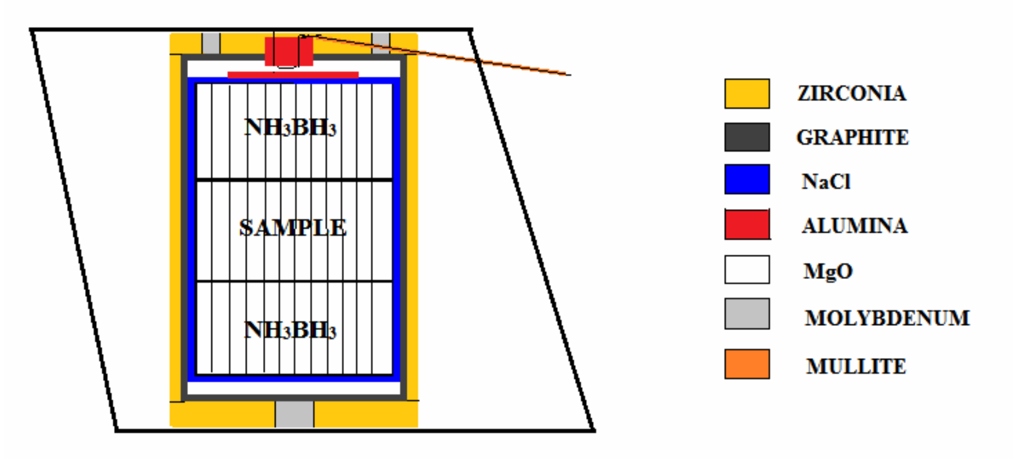

Figure 2.5. Schematic drawing of MA 18/12 assembly. The striped area is the empty space inside NaCl capsule (blue) that holds the sample and hydrogen pellets.

A Type C thermocouple (W5%Re-W26%Re wires) was inserted into top end-sleeve. To avoid the thermocouple wire breakage during the compression, the harder wire that contained less rhenium was placed at the bottom and the softer wire that contained more rhenium was placed on the top. The wires were overlapped by forming a loop at the end of each wire and inserted into 4-bore alumina which was positioned in the middle of the graphite furnace top disk and the zirconia top end-sleeve.[5] The thermocouple wires were bent along the grooves on the zirconia top end-sleeve and protected inside the pressure medium using mullite (Fig. 2.5 noted in orange) and outside the pressure medium using Teflon. The thermocouple was cemented into octahedron as well as both the top and bottom end-sleeves.[5]

The sample containing MgO pressure medium was positioned into an octahedral hollow space inside of the eight inner tungsten carbide (WC) anvils. Four of the inner anvils were lined with laser-cut paper to help position pyrophyllite gaskets around the trunctuation (Figure 2.6

upper left and upper right pictures). The gaskets acted as lubricant between the cubes. The eight inner anvils were positioned into a cubic hollow space created by the six outer steel anvils which were placed inside of a confinement ring in a module (Fig. 2.6 lower right). The hydraulic load (up to 1000 tonnes) was applied uniaxially to achieve the desired pressure (up to 10 GPa).[5]

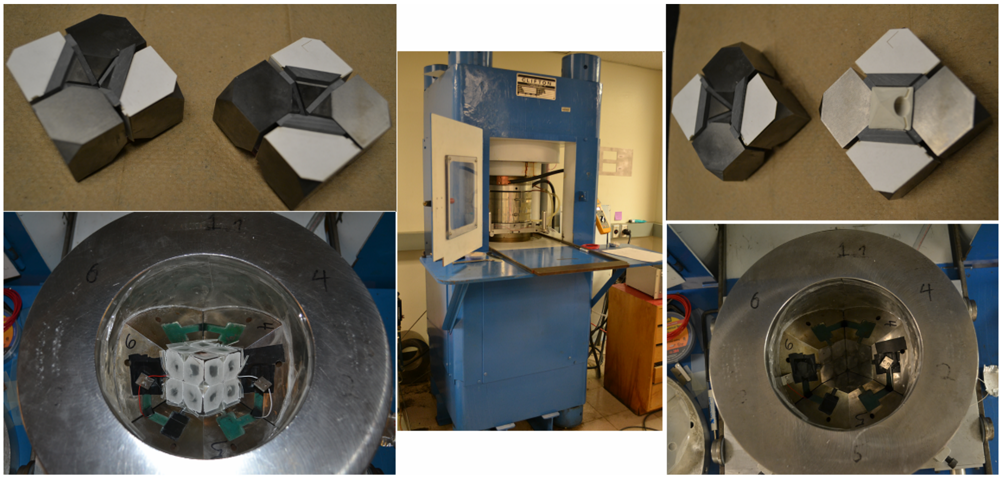

Figure 2.6. Walker 6-8 type multi-anvil apparatus. The eight inner anvils (upper left and right) and the six inner anvils (lower left and right) inside the module. The hydraulic press (middle) is used to apply a hydraulic load.

Compression to the desired pressure was performed at a rate of 0.5 GPa per hour. After the target pressure was reached, the sample was heated by applying current through the graphite furnace using the molybdenum leads. Temperature was monitored using a Eurotherm 2404 controller connected to a Type C thermocouple. After heating, the sample was rapidly quenched while maintaining the pressure in order to preserve the high-pressure phase. Decompression to the ambient pressure was done applying the same rate as for compression. In Chapter 4 and 5, the exact synthesis conditions for different systems will be explained.

Temperature was monitored for each individual run, and the applied pressure was determined based on calibrations by Stoyanov, et al.[5] Since the multi-anvil arrangement absorbs a fraction of the force applied to the system, the calibration is assembly and synthesis condition specific. Based on calibrations, the temperature (up 1500 ˚C) to was observed to linearly dependent on the pressure. Stoyanov, et al.,[5] observed this by performing calibrations at three different pressures (Figure 2.7).

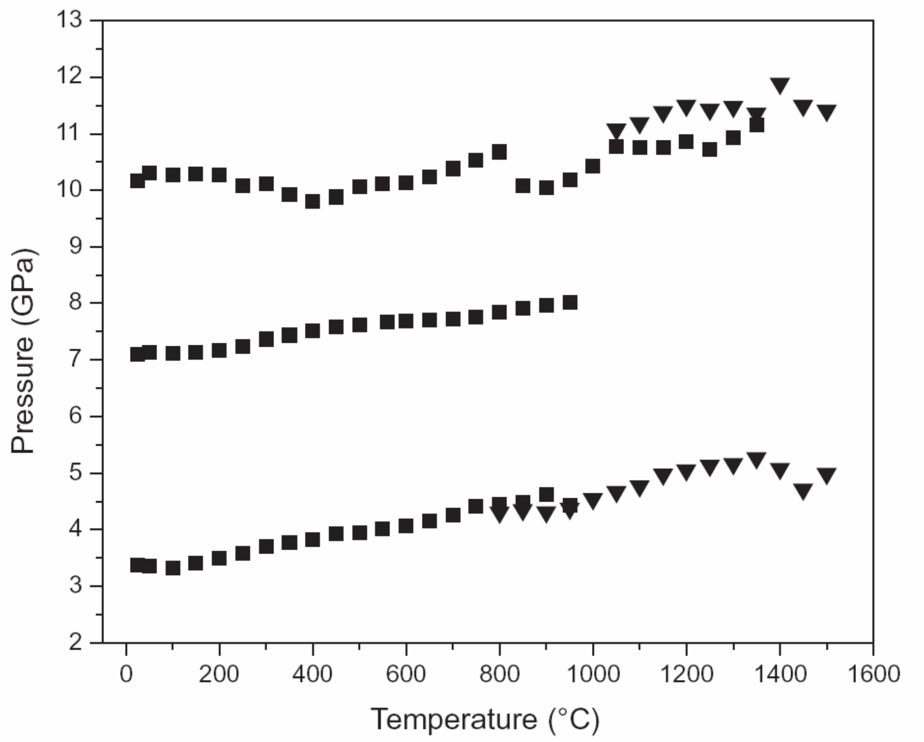

Figure 2.7. Calibrations of MA 18/12 assembly at three different pressure conditions.[5]

Based on the calibrations, the equation to determine the pressure (y in GPa) in any experiment was established as a function of load (x in tonnes).[5]

$$y = B x + C x^2 \qquad \textit{Equation 2.1}$$

There was almost no variation in fitting parameters, B and C in room temperature and at high temperature (1200 ºC).[5]

Table 1.1 Calibration Parameters[5]

Temperature	Fitting parameters	
	B	C ($\times 10^6$)
RT	0.0197	-7.587
HT	0.02045	-6.9554

*RT = Room Temperature, HT = High Temperature

An axial thermal gradient was found to exist in the 18/12 assembly[5] due to a thin zirconia sleeve used for the thermal insulation, and additionally the thermal sink effect due to molybdenum leads. The gradient is approximately 10 ˚C/mm which in case of thin samples (< 3 mm) is acceptable.[5]

The thermally activated hydrogen release behavior of the hydrogen source, ammonia borane, has been well studied (details in Chapter 1). From the practical point of view, the importance of the selected capsule material (NaCl) is its ability to resist the hydrogen diffusion. However, it has been experimentally observed that if a molar ratio between hydrogen source and precursor is too high, the excess hydrogen tends to cause a blowout (i.e. abrupt large-scale pressure-drop) at or above ammonia borane decomposition temperature. Hydrogen volume in a solid material is smaller than the volume of hydrogen gas/liquid, and the blowout can be contributed to inability of the system to respond to suddenly increased volume changes due to hydrogen release. This blowout occurrence can also be connected to unreactive (or slow kinetics) precursor-hydrogen reaction (i.e. hydride formation).

Optimizing the hydrogen content to avoid blowouts becomes crucial when exploring completely new systems without any previous knowledge of hydrogen uptake in the particular system. The excess hydrogen (which did not participate in hydride formation) expands in volume as the pressure is decreased during decompression, and because of ammonia borane has irreversible hydrogen release this excess hydrogen escapes from the capsule. In case of a large excess of hydrogen a blowout can occur during decompression, whereas, in case of a small amount of unreacted hydrogen a blowout is avoided. The former leads to a complete loss of a sample (flushed out of the capsule together with the escaping hydrogen). In the latter case hydrogen escape can be recognized as so-called “rivermarks” appear on the gaskets lining the WC-cubes. However, the sample is often recoverable although the three pellet system is typically disfigured. Instead of retaining the original pellet shape, a sample often appears elongated along the capsule and sometimes completely mixed with the surroundings which makes the sample recovery challenging.

The maximum precursor-to-hydrogen ratio is experimentally determined and depends on used precursors. In particular, it depends on how much hydrogen will react to form a hydride product, and how much remains as an excess. Based on this study, a good starting point is to occupy less than one third of the capsule volume with the precursor. The precursor-to-hydrogen ratio can be adjusted depending on observed behavior in the MA experiments.

2.3 Analysis

Solid state precursors and products were analyzed using the powder x-ray diffraction (PXRD) for polycrystalline samples, and the single crystal x-ray diffraction (SCXRD) in the case of well defined crystals. Thermal studies to define decomposition temperatures and to identify reversible/irreversible thermal events were performed using Differential Scanning Calorimetry (DSC). Spectroscopic methods (infrared and Raman) were used to analyze hydrogen-containing materials in order to gain information regarding the bonding situations and strengths. Theoretical calculations were done to confirm and support the analysis.

2.3.1 Powder X-ray Diffraction (PXRD)

Powder X-ray diffraction was used to find the unit cell parameters and atomic positions for heavy atoms. Diffraction of x-rays from the repeating atom planes in crystals can be used to determine the distance between the planes (d-spacing) in materials. The Bragg's law[6] gives the correlation between scattering conditions (scattering angle, θ) and the distance between lattice planes (d) for any known scattering wavelength (λ) used. The intensity of a diffraction peak is related to the type of atom and the scattering strength is proportional to the atomic number of the element (i.e. number of electrons). Heavier atoms have more scattering power whereas the light atoms scatter weakly. Therefore, x-ray diffraction cannot be used to detect light atoms, like hydrogen, in the presence of heavy elements.

A Siemens D5000 powder diffractometer with Bragg-Brentano (θ:θ) geometry and CuKα radiation (λ = 1.54059 Å) was used in the early stages of this study. Since the materials were air and moisture sensitive, the sample holder slide was prepared inside an Ar-filled glovebox (O_2/H_2O < 0.3 ppm) and covered with a Kapton tape before transporting to a diffractometer. An internal standard, silicon (a = 5.309 Å), was used with the aim of determining the unit cell parameters and the heavy atom positions. PFILM program was employed to correct the observed peak positions (relative to the internal standard silicon) and TREOR97 was used to determine the unit cell symmetry whereas the unit cell parameters were refined using PIRUM.[7-9]

A Bruker D8 Advance diffractometer (transmission geometry; CuK_α radiation) was used to measure the powder samples sealed into 0.3 mm (ID) capillaries which were filled and sealed inside the glovebox. Typical measurement 2θ range was from 10˚ to 90˚ using the step size of 0.016˚. Least squares refinement for the measured and indexed lines were used to obtain the lattice parameters.[9] TOPAS[10] software was applied to refine structures from PXRD patterns. If there were several phases present, the phase fractions were also refined in addition to refining background, unit cell, sample displacement, zero point, profile, strain, preferred orientation, atomic position and atomic absorption.[11]

2.3.2 Single Crystal X-ray Diffraction (SCXRD)

Single crystal x-ray diffraction provides detailed information of the crystal lattice. The unit cell, bond lengths, bond angles, and atomic site ordering can be solved based on the collected and refined diffraction data. Compared to the PXRD technique, the SCXRD uses a shorter wavelength of radiation which directly relates to the higher resolution at atomic level.

Crystals for intensity collection were selected in the glovebox (air and moisture-free conditions) under nitrogen atmosphere and inserted into 0.3 mm capillaries to ensure protection from air and moisture during the intensity collection. If necessary, larger crystals were crushed between two glass slides to obtain single crystals. Room temperature intensity data was collected by a SMART APEX diffractometer employing a graphite monochromated MoKα ($\lambda = 0.71073$ Å) radiation. The intensity data was corrected for Lorenz and polarization effects, and SADABS was used for absorption correction.[12] Systematic absences and statistical analysis of intensity distributions were applied to assign a space group. SHELXS-97 and SHELXL-97 were employed for direct method structure determination and full-matrix least squares F^2 refinement, respectively.[13]

2.3.3 Spectroscopy

Spectroscopic methods can be applied to detect the bonding geometries and bonding strengths in materials. The infrared (IR) modes are observed when a change in the molecule's dipole moment occurs, and the Raman modes are detected as a change in polarization arises.

Geometric considerations determine the number of the observable modes in optical spectroscopy. For the crystals, the allowed modes can be determined based on the symmetry analysis. It is possible that the number of predicted and observed bands differ due to possible combinations of the modes and the overtones. Acoustic modes cannot be observed with the conventional optical spectroscopy. In the collected spectrum, the vibration frequencies (Hz) are shown as wavenumbers (cm^{-1}) versus the intensity. Bonds have characteristic vibrating frequencies which allows to distinguish them in spectra.[14]

IR and Raman spectroscopy can be used to complement each other and conclude the analysis of the bonding environments. FTIR spectroscopy is a non-destructive method based on the sample absorbing and transmitting the radiation. The intensity originates from light absorbed or transmitted by the sample and is measured in a relative scale to the background.[14,15] Raman spectroscopy is a destructive method based on inelastic scattering technique requiring the laser excitation and a change in vibrating phonon frequencies is observed.[14,15]

In Fourier transform infrared spectroscopy (FTIR), a part of the IR radiation is absorbed by the sample and part of the radiation is transmitted through the sample. All the frequencies are measured simultaneously using an interferometer. The radiation source is guided through an interferometer, which consists of two mirrors (fixed and translating), and a beam splitter which transmits and reflects the radiation. The transmitted part of the beam moves to a fixed mirror and the reflected beam to translating mirror causing a path difference in interferometer. The interferogram (light intensity versus optical path difference) is a result of those two divided beams interfering with each other. The Fourier transformation converts the signal into a spectrum where the spectral lines are shown as a function of wavelength. A background spectrum is collected before a sample data collection.[14,15]

A Bruker IFS 66v/s instrument (4 cm^{-1} resolution) was used for Fourier transformation infrared spectroscopy (FTIR) to collect the data over the range from 400 to 4000 cm^{-1}. Background spectrum was measured with a pure KBr disk. The samples were pressed into a thin KBr disk and prepared under argon atmosphere (air and moisture-free conditions) before transporting to the spectrometer in a sealed container.

A custom-built Raman spectrometer in 180˚ geometry (resolution 2 cm^{-1}) was used to measure the samples which were sealed into a 0.3 mm capillary under argon atmosphere. Excitation of the sample was achieved using 532 nm laser witch was controlled using neutral density filters, and the power was reduced to 0.65 mW. Mitutoyo objective (50x super long working distance) with a numerical aperture 0.42 was used to focus laser on the sample. The signal was discriminated from the laser excitation using a Kaiser laser band pass filter followed by a Semrock edge filter. Acton 300i spectrograph and Princeton Instruments liquid cooled CCD detector was used for data collection.

2.3.4 Thermal Analysis

Thermal analysis can be used to determine decomposition pathways and stability ranges for materials and phases. Based on the heat flow measured, the thermal events can be classified as exo- or endothermic. Consecutive heating and cooling cycles are repeated to reveal whether the nature of those events is irreversible or reversible. The signal can also be quantitatively evaluated in order to obtain enthalpies related to the observed thermal events.

A Mettler-Toledo TGA/DSC 1 differential scanning calorimetry (DSC) and Mettler $STAR^e$ v.9.30 software was used for data acquisition and evaluation.[16] A sample pellet (10 - 15 mg) was hermetically sealed into TA TZero® aluminum pans under argon atmosphere. Temperature and heat flow were calibrated using indium (T_m = 156.6 ˚C, ΔH_{fus} = 28.5 J/g) and tin (T_m = 231.9 ˚C, ΔH_{fus} = 59.2 J/g) and a horizontal baseline was applied for the data integration.

The samples were heated/cooled at a rate of 10˚C/min from 50 to 300˚C (three cycles), followed by final heating up to 380˚C to fully decompose the sample (Chapter 3: Li_2Al and Li_9Al_4). A nitrogen flow of 40 ml/min was used during the heating and cooling. At the beginning on each heating and cooling segment the sample was equilibrated for five minutes.

2.3.5 Theoretical Calculations

Theoretical calculations can provide guidance to reaction design and help to interpret the experimental results. The density functional theory (DSF) is the most successful first-principles method within the local spin density approximation (LSDA).[17,18] The method works well with strongly correlated materials, and has further developed in order to be able to apply the calculations for a variety of situations.

In this study, the theoretical first-principles calculations were performed in the framework of the frozen core all-electron Projected Augmented Wave (PAW) method.[19,20] The program VASP[21,22] was used and the plane wave Abnit code[23] was implemented and the generalized gradient approximation GCA-PBE[24] or PW91[25] was used as the exchange correlation. The integration over the Brillouin zone was performed by applying a Monkhorst-Pack grid.[26]

Additional information on the calculations is given in Chapters 4, Chapter 5, and Appendix C.

2.4 References

1. Bronger, W.; Auffermann, G., *Chem. Mater*. **1998**, 10, 2723
2. Bushmann, E., *Z. Anorg. Alleg Chem*. **1961**, 313, 90
3. Boström, M.; Hovmöller, S., *J. Solid State Chem*. **2000**,153, 398
4. Walker D.; Carpenter, M.A.; Hitch, C.M., *Am. Mineral*. **1990**, 75, 1020
5. Stoyanov, E.; Häussermann, U.; Leinenweber, K., *High Pressure Res*. **2010**, 30, 175
6. Klug, H.P.; Alexander, I.E., *X-ray Diffraction Procedures*, 2nd ed., Wiley, New York, **1974**
7. Eriksson, L., Computer Program PFILM, Stockholm University, Communication
8. Werner, P.E.; Eriksson, L.; Westdahl, M., *J. Appl. Cryst*. **1995**, 18, 367
9. Werner, P.E., *Ark. Kemi* **1969**, 31, 513
10. Bruker AXS, *TOPAS V4; General profile and structure analysis software for powder diffraction data*, User's manual, Karlsruhe, Germany, **2008**
11. Sabine, T.M.; Hunter, B.A.; Sabine, W.R.; Ball, C.J., J*. Appl. Crystallogr*. **1998**, 31, 47

12. Sheldrik, G.M., *SADABS Version 2.*10, University of Göttingen, Germany, **2003**

13. Sheldrik, G.M., *SHELX97 and SHELXL97*, University of Göttingen, Germany, **1997**

14. Harris, D.C.; Bertolucci, M.D., *Symmetry and Spectroscopy: An introduction to Vibrational and Electronic Spectroscopy*, Dover Publications Inc. New York, **1989**, pp. 90 – 189

15. Bellamy, L.J., *Infrared Spectroscopy* **1961***,* 28, 1059

16. Mettler-Toledo GmbH, *Thermal Analysis, DSC Evaluation*, User's Manual, Schwerzenbach, Switzerland, **2003**

17. Hohenberg, P.; Kehn, W., *Phys. Rev*. *B* **1964**,136, 864

18. Kohn, W.; Sham, L.J.*, Phys. Rev*. *B* **1965**,140,1133

19. Blöch, P.E., *Phys. Rev*. *B* **1994**, 50, 17953

20. Kresse, G.; Joubert, J.*, Phys. Rev*. *B* **1999**, 59, 1758

21. Kresse, G.; Harner, J., *Phys. Rev*. *B* **1993**, 48, 13115

22. Kresse, G.; Furthmüller, J., *Comput. Mater. Sci*. **1996**, 6, 15

23. Gonze, X.; Amadond, B.; Anglade, P.M.; Beuken, M.M.; Bottin, F.; Boulanger, P.; Bruneval, F.; Caliste, D.; Caracas, R.; Cote, M.; Deutsch, T.; Genovese, L.; Ghosez, Ph.; Giantomassi, M.; Goedecker, S.; Hamann, D.R.; Hermet, P.; Jollet, F.; Jomard, G.; Leroux, S.; Mancini, M.; Mazevert, S.; Oliveria, M.J.T.; Onida, G.; Poullon, Y.; Range., T.; Rgnanese, G.M.; Sangalli, D.; Shaltaf, R.; Torrent, M.; Verstraete, M.J.; Zerah, G.; Zwanziger, J.W., *Comput. Phys. Commun*. **2009**, 180,2582

24. Perdew, J.P.; Burke, K.; Ernzerhof, M., *Phys. Rev. Lett*. **1996**, 77, 3865

25. Pedrew, J.P.; Wang, J., *Phys. Rev*. *B* **1992**, 45, 13244

26. Monkhorst, H.J.; Pack, J.D., *Phys. Rev*. *B* **1976**, 13, 5188

CHAPTER 3

HYDROGENOUS ZINTL PHASES

3.1 Introduction

Hydrogenous Zintl phases can be obtained either by hydrogenating a precursor Zintl phase, or by reacting hydrides of active metals (alkali, alkaline earth, rare earth) with p-element metals or semimetals.[1,2] The latter method usually requires higher synthesis temperature.[1,2] In this study, the hydrogenations of Zintl phase precursors are employed. Interest in the hydrogenous Zintl phases was triggered by the possibility of creating new coordination environments and bonding situations in metals which in turn could lead to interesting and novel properties in these materials.[3,4]

As shown earlier, the hydrogenation of Zintl phases can lead to the formation of either interstitial or polyanionic hydrides. In an interstitial Zintl phase hydride, hydrogen is coordinated exclusively by active metal atoms (Figure 3.1a).[5] In a polyanionic hydride, hydrogen is incorporated into the polymeric anion and acts as a covalently bonded ligand to a p-block element (Figure 3.1 b).[5] However, frequently the hydrogenation of Zintl phases leads to an oxidative decomposition which results eventually in the formation of active metal hydride and free p-block element (Figure 3.1a).[5]

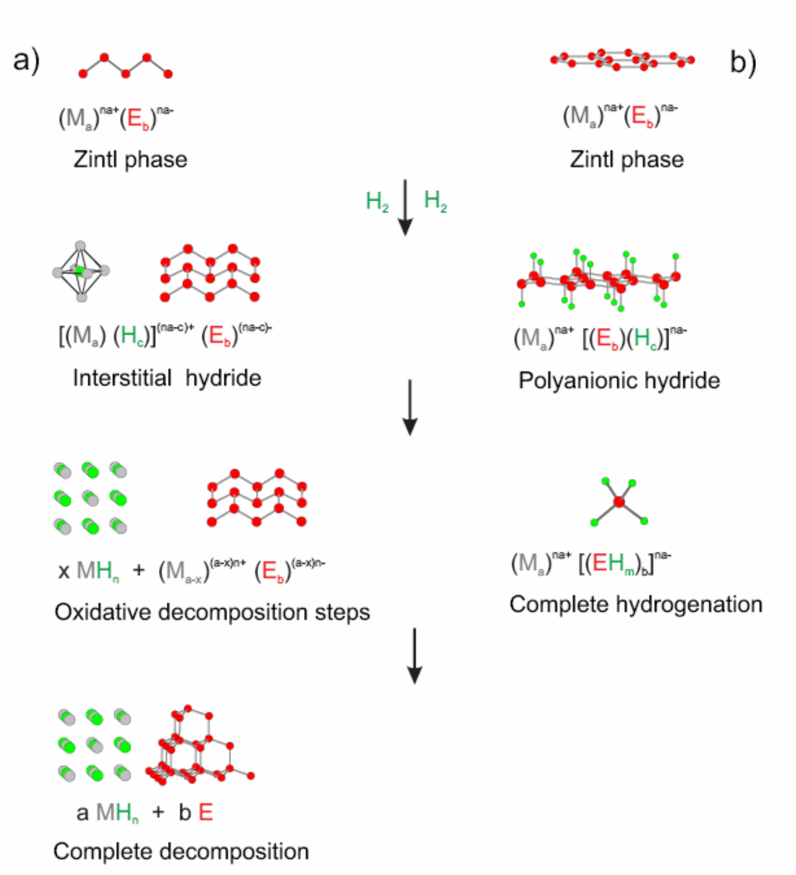

Figure 3.1. Zintl phase hydrogenation routes starting with Zintl phase precursor.[5]

In this study, hydrogenations of Zintl phases were mostly focused on Zintl phases containing either aluminum or gallium. Especially interesting is the lithium-rich side of the Li-Al phase diagram as the lithium-rich intermetallics are particularly promising as hydrogen storage materials.[8,9] The Li-Al phase diagram on aluminum-rich side is well established as the lithium doped Li-Al alloys are commonly used in aerospace industry.[12]

LiAl phase crystallizes with the NaTl structure (*Fd*-3*m*)[1,13] and displays a homogeneity range from 48 to 55 at.% of lithium. The isostructural phases LiGa and LiIn are also known.[14] The Li-Al system displays two other stable phases, Li_3Al_2[15] and Li_9Al_4,[16] which both are line compounds. The rhombohedral structure of Li_3Al_2 is also found for the heavier analogs, Li_3Ga_2 and Li_3In_2.[17,18] The most lithium-rich phase Li_9Al_4 was reported to have a phase transformation from a monoclinic phase into the high temperature phase.[19,20] However, the proposed high temperature phase has never been characterized. Before proceeding with hydrogenations, the lithium-rich part of the Li-Al phase diagram was investigated to properly identify the stable phases on the lithium-rich side of the LiAl phase diagram. It is important to know the underlying intermetallic phases in order to be able to accurately identify the possible hydrogenation products.

3.2 Synthesis of Precursors

There are some apparent inconsistencies of the Li-rich part of the Li-Al phase diagram. Thermal events have been reported at around 267 and 242 ºC and interpreted as the transformation of monoclinic Li_9Al_4 into a high-temperature phase.[21,22] However, characterization of such a phase has never been undertaken. In this study, the supposed high-temperature modification of Li_9Al_4 was synthesized using the composition of $Li_{91.5}Al_{8.5}$ which lead to a discovery of a new phase (Li_2Al) in the Li-Al system. The discovery of this phase explains the previously reported thermal events and rules out the existence of a high-temperature phase for Li_9Al_4. The composition of $Li_{96}Al_4$ was aimed to produce the previously known low-temperature phase Li_9Al_4.

Both synthesis were carried out using the isothermal melt cenfiguration method and all sample preparation was performed in an Ar-filled glovebox under air and moisture-free conditions (details in Chapter 2). The chosen compositions, $Li_{91.5}Al_{8.5}$ and $Li_{96}Al_4$, targeted an equilibrium between melt and the Li-richest phase at a certain temperature (Figure 3.2). Both reaction mixtures were heated to 450 ºC and kept at this temperature for one hour. The reaction mixtures were cooled down to 300 ºC ($Li_{91.5}Al_{8.5}$) and 210 ºC ($Li_{96}Al_4$) and left at their target temperatures for seven days. The solid state sample and melt was separated by isothermal centrifugation.

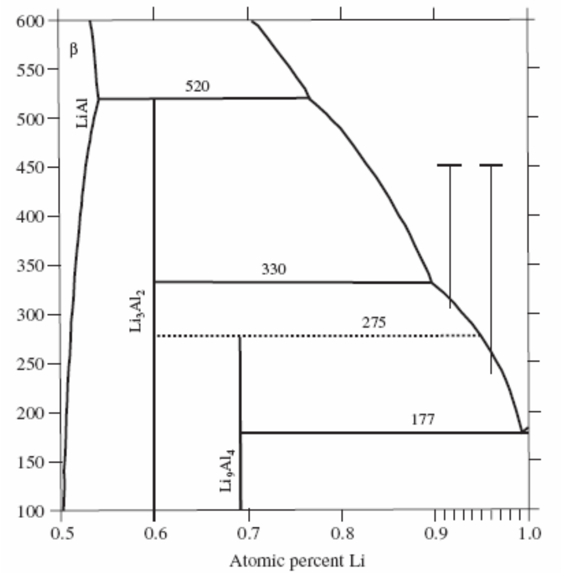

Figure 3.2. Lithium-rich part of Li-Al phase diagram. Synthesis temperatures and compositions to approach the desired phases from the liquid state are shown in phase.

The products obtained after isothermal centrifugation had a profoundly different appearance. The $Li_{96}Al_4$ mixture yielded large, mm-sized crystalline blocks with lamellae structured surfaces and dark, almost black luster. The product from $Li_{91.5}Al_{8.5}$ mixture corresponded to needle-shaped grey crystals with lengths up to 8 mm and thickness up to 1 mm. The x-ray analysis later confirmed that different products were obtained.

3.3 Characterization of a New Phase Li_2Al

As expected, the product of $Li_{96}Al_4$ mixture corresponds to a known monoclinic Li_9Al_4.[19,20] The lattice parameters extracted from the indexed pattern are a = 18.968(5) Å, b = 4.508(1) Å, c = 5.417(1) Å and β = 105.49(1)°.[23] Some additional weak reflections in the powder x-ray pattern could not be identified (Appendix A). The $Li_{91.5}Al_{8.5}$ reaction produced a new orthorhombic phase.[23] The diffraction peaks were indexed and the lattice parameters were extracted as a = 4.6404(8) Å, b = 9.719(2) Å, and c = 4.4764(8) Å. Remaining reflections stem from a small amount of monoclinic Li_9Al_4 (Appendix A). The new phase was subsequently characterized as Li_2Al, crystallizing with the same structure as Li_2Ga and Li_2In.[17,24] The refinement of single crystal x-ray diffraction data revealed that the Li atom positions in the Li_2Al structure were partially occupied with Al (refined total composition $Li_{1.92(1)}Al_{1.08(1)}$, 64 at.% Li)[23] which indicates a small homogeneity range, $Li_{2-x}Al_{1+x}$, for this phase.

Li_2Al crystallizes in the orthorhombic space group *Cmcm*. The structure consists of three atomic positions 4c, one for Al and two for Li (Li1 and Li2). Refinements of occupancies for the Li sites, however, resulted in a significant lowering of the R1 index (from 0.033 to 0.025) when considering a mixture with Al (4 – 5 %). Nevertheless, in the following these positions are referred as Li atom positions. The more complex structure of Li_9Al_4 crystallize in monoclinic *C*2/*m* space group setting. The unit cell of Li_9Al_4 is about twice the size of Li_2Al unit cell, and contains two Al (Al1 and Al2) and four Li (Li2 – Li5) atomic positions 4i. Additionally, a fifth Li site at 2a (Li1) occurs. In contrast with Li_2Al, refinements of Li_9Al_4 site occupancies did not indicate the presence of significant Li/Al disorder which supports the previous assignment of Li_9Al_4 as stoichiometric line compound.[19] The crystallographic data for Li_2Al and Li_9Al_4 is shown in Table 3.1.

The interatomic distances below 3.5Å for Li_2Al and Li_9Al_4 with standard deviations were computed from the single crystal refinement (Appendix B). In Appendix B, also the fractional atomic coordinates and equivalent atomic displacement parameter for Li_2Al and Li_9Al_4 with estimated standard deviations are shown.

Table 3.1 Crystallographic data for Li_2Al and Li_9Al_4 obtained at room temperature (298K) using Mo*K*α radiation (0.71073 Å)

Analysis for	Li_2Al	Li_9Al_4
Formula	$Li_{1.92(1)}Al_{1.08(1)}$	Li_9Al_4
Formula weight	42.5	170.38
Crystal size, mm^3	0.13 x 0.11 x 0.10	0.37 x 0.25 x 0.14
Space group	*Cmcm* (No. 63)	*C*2/*m* (No. 12)
a, Å	4.6579 (16)	18.916(4)
b, Å	9.767(4)	4.5041(11)
c, Å	4.4901(16)	5.4249(14)
β, deg	90.00	105.19(3)
Z; V, $Å^3$	4; 204.28(12)	2; 446.05(20)
D_{calc}, gcm^{-3}	1.381	1.269
Absorption coeff., mm^{-1}	0.493	0.420
F(000)	79	158
$\theta_{min} – \theta_{max}$, deg	4.174 – 32.972	2.23 – 24.85
Index ranges	$-6 < h < 6$ $-12 < k < 12$ $-5 < l < 5$	$-6 < h < 22$ $-5 < k < 5$ $-6 < l < 6$
Total reflns collected	500	5681
Independent reflns	145 [R(int)=0.0425]	452 [R(int)=0.0197]
Refinement method	full-matrix least squares on F^2	full-matrix least squares on F^2
Data/restrains/params	145/0/15	452/0/41
Final R indices $[I > 3\sigma(I)]^{a,b}$	$R_1 = 0.0251$ $wR_2 = 0.0545$	$R_1 = 0.0170$ $wR_2 = 0.0413$
R indices (all data)^{a,b}	$R_1 = 0.0286$ $wR_2 = 0.0558$	$R_1 = 0.0181$ $wR_2 = 0.0419$
Largest diff. peak and hole, $eÅ^{-3}$	0.183 and -0.183	0.129 and -0.160
GOF on F^2	1.056	1.20

^{a} $(R_1) = \Sigma F_0 – F_c / \Sigma F_0$

^{b} $wR_2 = \{\Sigma \{ w(F_0^2 – F_c^2)]/ \Sigma [w(F_0^2)^2]\}^{1/2}$

The crystal structures of orthorhombic Li_2Al and monoclinic Li_9Al_4 are closely related. In Figure 3.3, the structural relationship between orthorhombic Li_2Al (Figure 3.3e) and monoclinic Li_9Al_4 (Figure 3.3f) can be visualized. In the orthorhombic Li_2Al the lithium atoms are in equatorial (light grey) and apical (dark grey) positions. In the monoclinic Li_9Al_4 the additional lithium in the unit cell is shown as blue ellipsoid (Figure 3.3f). The thick black line indicates the unit cell edge, and the bonds between Li-Li and Al-Al (distances < 3 Å) are drawn using thin black lines. In Li_2Al structure, the lithium atoms are in zigzag layers (Figure 3.3c) which are separated by aluminum layers. Those layers are in the middle of the square pyramid building blocks composed of lithium atoms (Figure 3.3b) which the aluminum atoms complete into an octahedral arrangement.

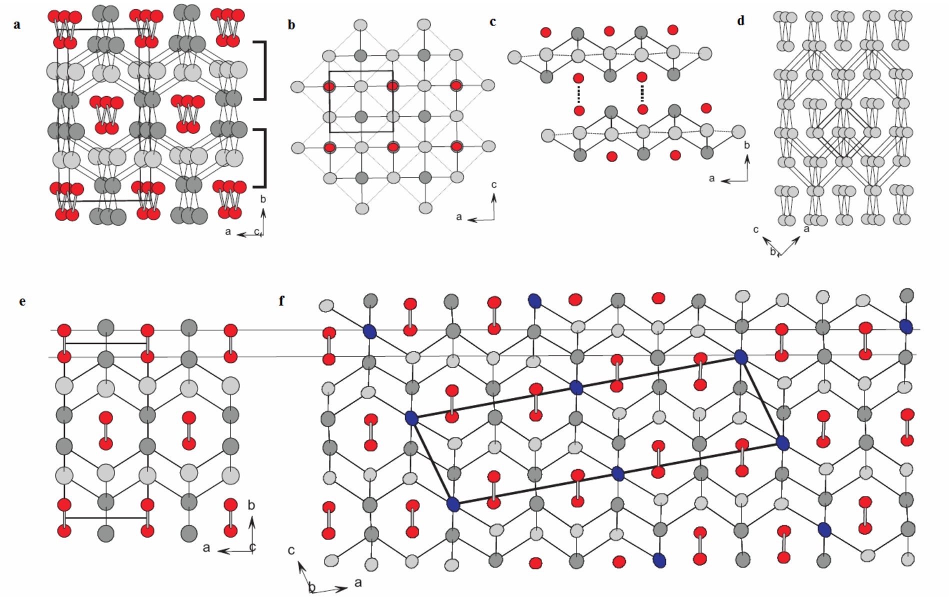

Figure 3.3. Li_2Al (a - e) and Li_9Al_4 (f) structure. Aluminum atoms are shown in red, and lithium atoms in light grey (equatorial), dark grey (apical) and blue (additional Li atom in Li_9Al_4 structure).[23]

The prominent feature in both structures is the planar zigzag-chain arrangement of Al atoms which can be considered as polyanions. The Al-Al distance is 2.70 Å and 2.68 Å in Li_9Al_4 and Li_2Al, respectively. However, in the Li-Al system only the β-phase LiAl with a diamond-like Al substructure formally corresponds to an electron precise Zintl phase, and Al-Al distance is 2.75 Å.[13] In Li_3Al_2, Al atoms form puckered hexagonal layers with and Al-Al distance of 2.73 Å.[15] The Li-rich phases, Li_3Al_2, Li_2Al and Li_9Al_4, are electron deficient with respect to the electronic requirement of a polyanionic substructure consisting of singly bonded Al atoms.

In Li_2Al (Figure 3.3), the Al zigzag chains run along the crystallographic *c* direction. The Li1 atoms (equatorial atoms) form an almost regular two-dimensional square net, which are alternately capped above and below by Li2 atoms (apical atoms). In the resulting layer of square pyramids Li1 attains a quasi-tetrahedral coordination by four Li2 atoms. The Li1-Li2 distances are around 2.76 Å. The Al atoms complete Li1Li2 square pyramids to octahedra, and layers of edge condensed octahedral are now stacked along the *b* direction. The shift introduced by the C-centering arranges Al atoms and apical Li2 atoms into layer-connecting zigzag chains where the Li2-Li2 distance is 2.86 Å.

A relationship between the Li_2Al (Li_2Ga) structure and the body centered cubic (bcc) structure is seen when focusing on the quasi-close-packed arrangement of atoms in the *bc* plane and its stacking along the *a* direction. In Figure 3.2d, the bonds were first drawn for 8+6 coordinated atoms and subsequently selectively removed to yield the connectivity of the Li_2Ga-type structure. It should be noted that the relationship between bcc and Li_2Ga structure is of rather topological nature. The axial ratios of the orthorhombic unit cell of the Li_2Ga structure are $b/a \sim 2$ and $c/a \sim 1$, whereas the corresponding values for the bcc arrangement are $b/a \sim 3$ and $c/a \sim 0.71$. However, the relationship is helpful for explaining the Li_9Al_4 structure. It is easily derived from the Li_2Al structure (Figure 3.3e) by inserting into each quasi-close-packed layer an additional row of Li atoms after 12 regular rows of Li2, Li2 and Al atoms.

As for Li_2Al, the aluminum zigzag-chains in the Li_9Al_4 structure are symmetry equivalent but now composed of two different kinds of Al atoms. Likewise, there are two kinds of apical (Li2 and Li4) and equatorial Li atoms (Li3 and Li5), respectively. The inserted Li atoms (Li1) have the connectivity of apical atoms. Interatomic distances for nearest neighbor pairs Li-Li and Li-Al are very similar to Li_2Al (Appendix B).

The results for the thermal analysis of Li2Al and Li_9Al_4 (details in Chapter 2) are depicted in Figure 3.4 and Figure 3.5, respectively. The DSC heating trace is indicated as a red line and cooling as a blue line for Li_9Al_4 and Li_2Al.

In Figure 3.4, the heating trace of Li_9Al_4 shows repeatedly a thermal event below 300˚C with an onset temperature of 270 ± 2˚C and the peak maximum at 274 ± 3˚C. The associated enthalpy is around 31 J/g. This event is attributed to a peritectic decomposition of Li_9Al_4 into the new, more Al-rich phase $Li_{2-x}Al_{1+x}$ and Li-rich melt. This reaction is reversible upon cooling although a large hysteresis indicates a slow re-formation of Li_9Al_4. The peak maximum of the exothermic event is between 220 ˚C to 230 ˚C. When heating Li_9Al_4 to 380 ˚C, a second endothermic event occurs at 337 ˚C (onset) with peak maximum at 343 ˚C. This event corresponds to the peritectic decomposition of $Li_{2-x}Al_{1+x}$ into Li_3Al_2 and Li-rich melt.

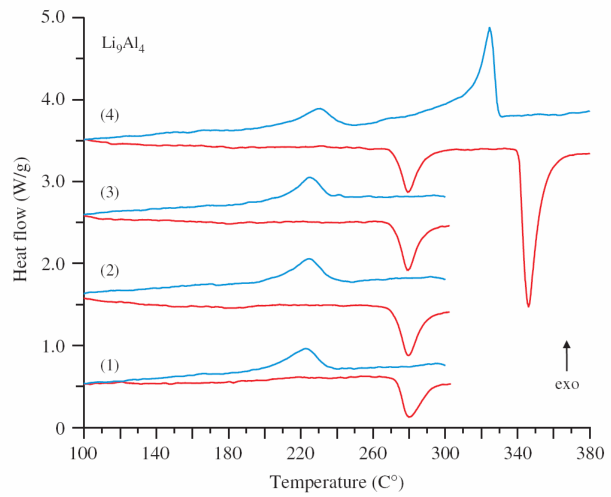

Figure 3.4. The DSC trace for Li_9Al_4 in which the red represents heating and the blue represents cooling trace.[23]

As expected, the DSC heating trace of $Li_{2-x}Al_{1+x}$ (Figure 3.5) does not show a thermal event below 300 ˚C. The heating trace of the first cycle shows a weak and broad endothermic feature around 220 ºC which is obtained reproducibly for different samples and may relate to Li/Al ordering in this phase. The event at 334 ˚C (onset) with peak maximum at 341 ˚C is the peritectic decomposition and matches the results from the Li_9Al_4. The enthalpy associated to the decompositions of $Li_{2-x}Al_{1+x}$ is around 93 J/g. The reaction is reversible upon cooling with a small hysteresis. The onset and peak maximum temperatures are at 328 ºC and 323 ºC, respectively, in the cooling trace.

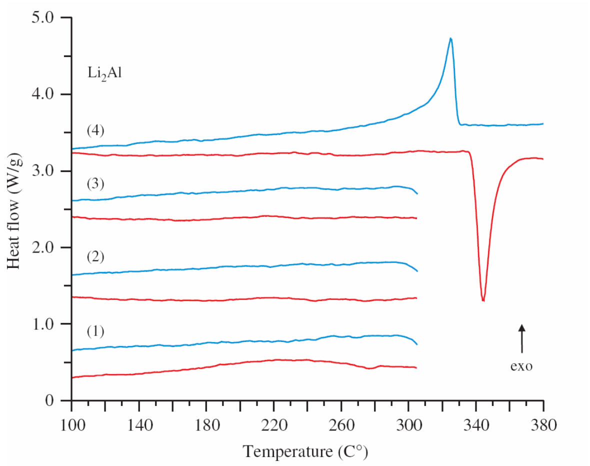

Figure 3.5. The DSC trace for Li_2Al in which the red line represents heating and the blue line represents cooling trace.[23]

The new findings were used to modify the the original phase diagram[21] (Figure 3.2). The discovery of the new phase Li_2Al ($Li_{2-x}Al_{1+x}$) resolved the mystery of the 275 ºC isotherm. The occurrence of Li_2Al is probably not too surprising in the light of the existence of isostructural Li_2Ga and Li_2In in the phase diagrams of the heavier congeners.[17,24] The modified phase diagram is shown in Figure 3.6.

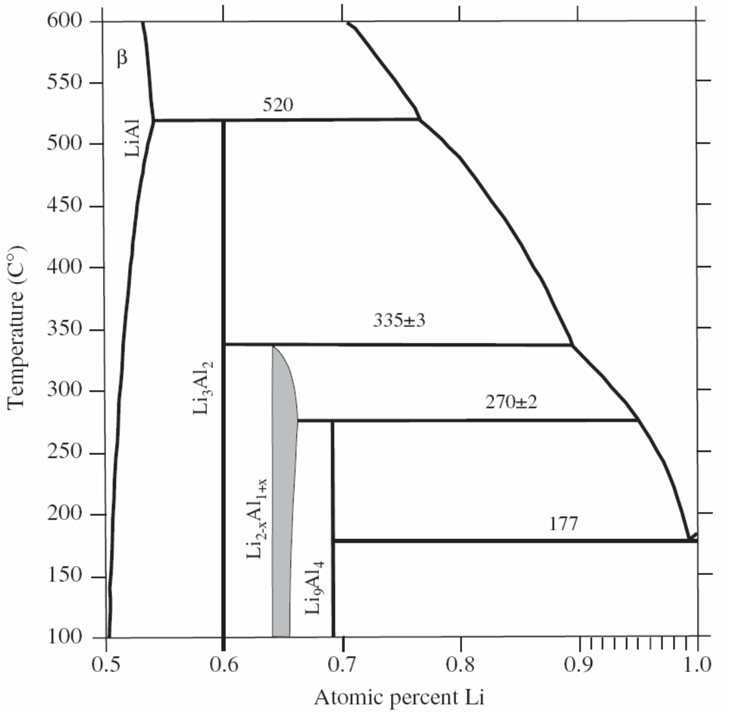

Figure 3.6. A modified Li-Al phase diagram where a new phase, Li_2Al, is shown in grey. [23]

After the refined phase diagram was established, the study was continued with the main group hydrogenations of Li-Al systems at low H_2 pressures.

3.4 Hydrogenation of Zintl Phase Containing Al or Ga

The kinetic and thermodynamic conditions of a particular system determine whether the hydrogenation of a Zintl phase leads to hydride, or not. High-temperature hydrogenations above 250 ˚C are more likely to be thermodynamically controlled and the structure of formed hydrides may differ substantially from the precursor structure. Low-temperature hydrogenations below 250 ˚C may proceed in a topotactic way and hydride and precursor structures show a close relationship.

Particularly interesting system is a rhombohedral Li_3Al_2 in which Al atoms form a polyanionic substructure that corresponds to corrugated hexagon layers.[15] These layers are stacked along the *c* direction and have the Li ions intercalated in between. The polyanionic structure reminds of the elemental structure of arsenic which is electron precise for 5 valence electrons per atom. Each atom is involved in three bonds to neighboring atoms and carries a lone pair. Formally the charge of polyanionic substructure is $[Al_2]^{3-}$ which implies deficiency by one electron per formula unit. The electronic density of states (DOS) shown in Figure 3.7. demonstrates that the hydride structure is energetically favored compared to Li_3Al_2.[25] Based on its electron deficient nature it could be expected that the Li_3Al_2 is susceptible to incorporating hydrogen, yielding the electron precise monohydride Li_3Al_2H. The proposed monohydride structure is composed of three-bonded $[Al]^{2-}$ and $[Al\text{-}H]^{1-}$ moieties, the former carrying a lone pair and the latter a terminal bond to the H ligand.

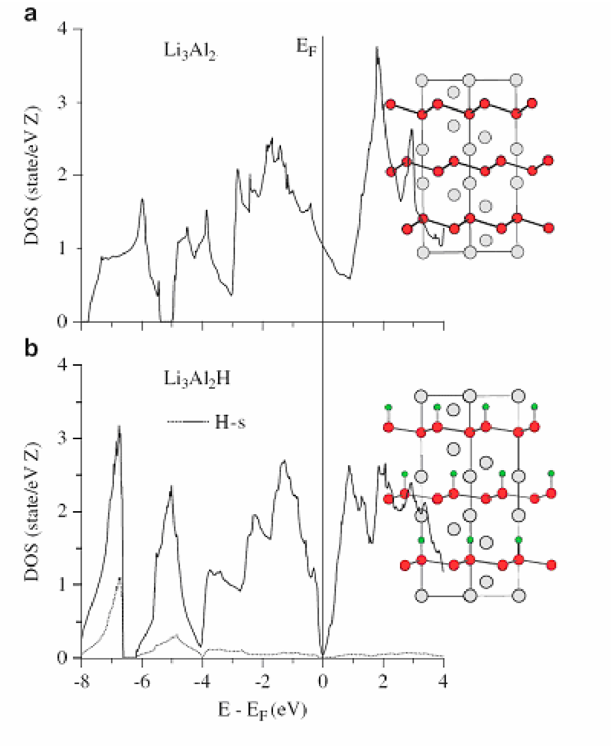

Figure 3.7. Density of states for Li_3Al_2 (a) and hypothetical Li_3Al_2H (b). The atoms are indicated as follows: lithium (grey), aluminum (red) and hydrogen (green).[25]

However, hydrogenations of Li_3Al_2 lead to an oxidative decomposition into mixture of LiH and LiAl instead of forming a hydrogenous Zintl phase (Figure 3.8). In Figure 3.8, the red arrows pointing down indicate the decrease in precursor Li_3Al_2 and the increased amounts of oxidative decomposition products of LiAl and LiH are shown as blue and black, respectively, arrows pointing upwards. Increased amount of decomposition products is seen as the reaction temperature is increased. The broad feature in the diffraction patterns at around $2\Theta = 25°$ stems for the plastic cover that was used to protect the air/moisture sensitive samples during the collection of the powder x-ray data.

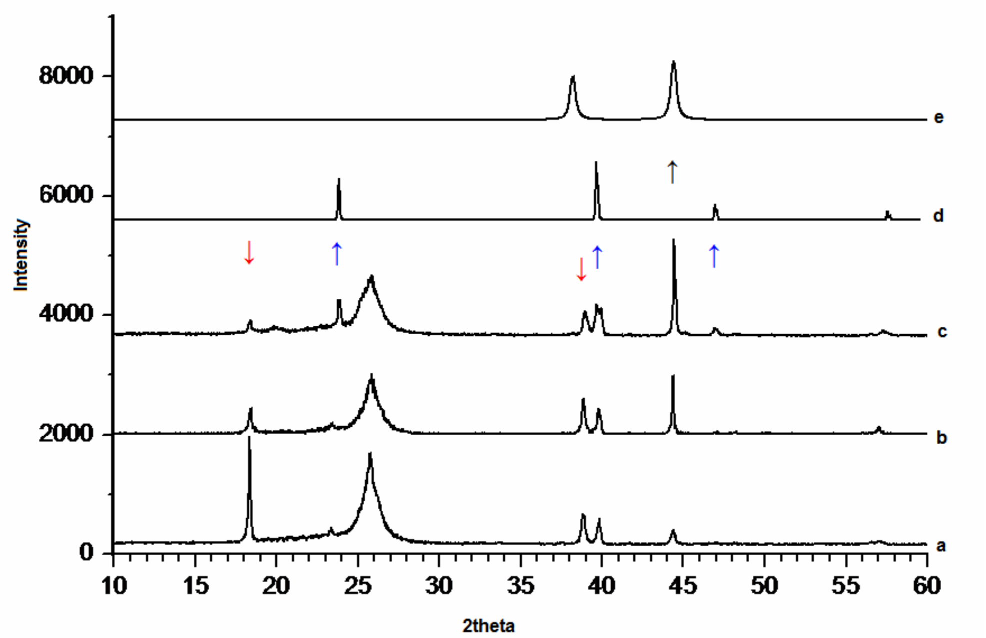

Figure 3.8. Oxidative decomposition of Li_3Al_2 (a). Hydrogenations of Li_3Al_2 (30 bar H_2) were done at 100˚C (b) and at 150˚C (a). The hydrogenation results are compared to theoretical LiAl (d) and LiH (e) patterns. The arrows pointing down indicate the decreased amount of precursor Li_3Al_2, and the arrows pointing up indicate the increased amount of decomposition products.

Similarly, attempts to hydrogenate the other lithium-rich aluminum phases, Li_2Al and Li_9Al_4, also resulted in an oxidative decomposition. Li_9Al_4 decomposed at 300 ºC (7 MPa H_2) into Li_3Al_2 and LiH even when short reaction times (up to 30 min) were used.

Likewise, the gallium-containing (electron deficient) Zintl phases Li_2Ga and Ca_3Ga_5 were expected to incorporate hydrogen in order to become electron precise. Similar to Li_2Al, the hydrogenation of Li_2Ga resulted in an oxidative decomposition into LiGa and LiH. This occurred already with very short reaction times (below 15 min) when applying the conditions 8 MPa H_2 pressure and 300 ºC. Ca_3Ga_5, which displays a tetragonal Cr_5B_3-type structure (*I*4/*mcm*)[26], decomposed into a mixture of $CaGa_4$ and CaH_2. The oxidative decomposition of Ca_3Ga_5 occurred already at very mild conditions, temperatures between 175 ºC to 200 ºC at 3 MPa H_2 pressure. The structure of non-electron precise precursor Ca_3Ga_5 and a hypothetical Ca_3Ga_5H which is electron precise are shown in figure 3.9.

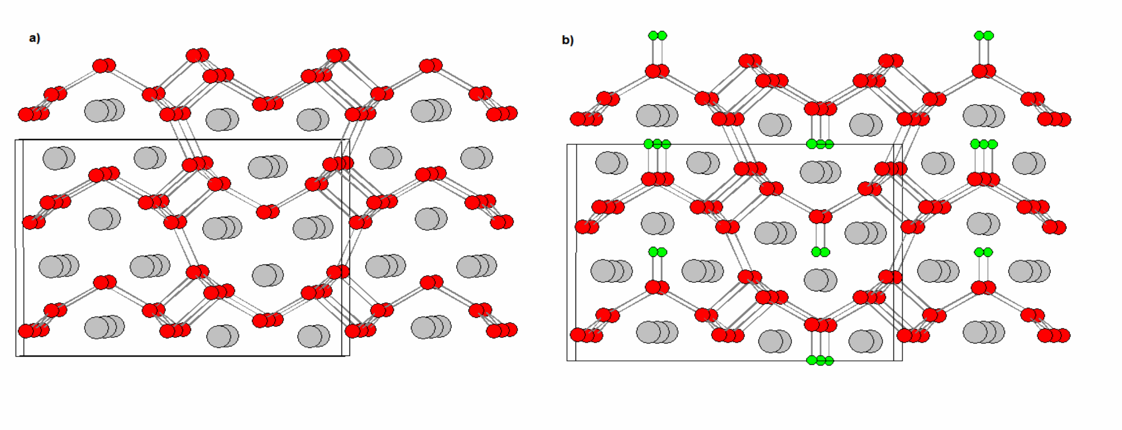

Figure 3.9. The tetragonal Ca_3Ga_5 (a) and a hypothetical elelectron-precise Ca_3Ga_5H (b). The atoms are noted as follows: calcium (grey), gallium (red) and hydrogen (green).

There are also several examples in the literature describing the oxidative decomposition of Zintl phases upon hydrogenation. For example, Wu, et al.,[27] studied the hydrogenation behavior of Ca_5Si_3 which belongs to a tetragonal Cr_5B_3-type.[28,29] At low hydrogen pressure (0.1 MPa) and temperature (300 ºC), the hydrogenation of Ca_5Si_3 produces a mixture of crystalline CaH_2 and $Ca_5Si_3H_{\sim 0.5}$.[27] It was noticed that when keeping the temperature at 300 ºC and increasing the pressure (> 3 MPa of H_2), hydrogenations lead to a decomposition of Ca_5Si_3 into amorphous CaH_2 and CaSi.[27] A similar decomposition behavior is observed when applying higher temperatures (500 ºC) and lower pressure (0.1 MPa).[27] This demonstrates that oxidative decomposition competes with hydride formation and sometimes there is no pressure or temperature window available for achieving the synthesis of hydrogenous product. Also, hydrogen-induced amorphization is observed when higher pressure (3 MPa) was applied.[27]

Wu, et al.,[30] further investigated the hydrogenation of Ca_2Si[31] which crystallizes in an orthorhombic structure. They found that conditions of 200 ºC and 1 MPa of H_2 lead to the formation of $Ca_2SiH_{\sim 2}$ as a major phase. Additionally, the formation of hydrides CaH_2 and $Ca_5Si_3H_x$, which displayed hydrogen-induced amorphization, were observed to coexist with the major phase.[30] At higher H_2 pressure (5 MPa), the $Ca_2SiH_{2.4}$ hydride formed. Higher temperature (400 ºC) increased the amount of decomposition products CaH_2, CaSi, and Ca_2Si.[30] In addition, the hydrogen-induced amorphization was more pronounced at higher temperatures and pressures.[30]

3.5 Conclusions

Research on hydrogenous Zintl phases was initiated in the mid-1990s and since then a wide variety of hydrogenous Zintl phases have been discovered and characterized. Hydrogenous Zintl phases can be divided into interstitial hydrides where hydridic hydrogen is exclusively coordinated by the active metal component, or as a polyanionic hydride where hydrogen is covalently bonded to the p-block metal/semimetal component as a part of the polyanionic framework.[1,2] Hydrogen-induced changes in the structures have lead to new coordination and bonding schemes. However, it is not yet fully understood which factors lead to the formation of polyanionic hydrides as opposed to interstitial hydrides.

The Zintl-Klemm concept[2] can be used to identify electronically imbalanced Zintl phases, potentially susceptible to hydrogen uptake. Accordingly, it was assumed that Li_3Al_2 which is electron deficient by one electron per formula unit, would be feasible to incorporating hydrogen and form a hydride. However, instead of expected Li_3Al_2H, oxidative decomposition into LiAl and LiH was observed. Similarly, oxidative decompositions were observed for other lithium-rich systems, namely Li_9Al_4 and Li_2Al, investigated in this study.

Hydrogenation of Li_2Ga resulted in a decomposition into the LiGa and LiH. Likewise, the oxidative decomposition into $CaGa_4$ and CaH_2 was observed in hydrogenations of Ca_3Ga_5. In all these systems, the oxidative decomposition occurred at low pressures and temperatures, and progressed even when short reaction times were applied. This demonstrates the challenges in predicting the hydride formation and finding the optimal conditions for the hydride formation which competes with the oxidative decomposition of the precursor phase.

3.6 References

1. Zintl, E.; Woltersdorf, G., *Z Angew. Phys. Chem* **1935**, 41, 876

2. Kauzlarich, S.M., Ed., *Chemistry, Structure, and Bonding of Zintl Phases and Ions,* VCH, New York, **1996**

3. Scähfer, H.; Eisenmann, B.; Müller, W., *Angew. Chem. Int. Ed.* **1973**, 12, 694

4. Nesper, R., *Prog. Solid State Chem.* **1990**, 10, 1

5. Häussermann, U., *Z. Kristallogr.* **2008**, 223, 628

6. Schüth, F.; Bogdanovic, B.; Felderhoff, M., *Chem. Commun.* **2004**, 2249

7. Sandrock, G.; Gross, K.; Thomas, G.; Jensen, C.; Meeker,D.; Takara, S., *J. Alloys Compd.* **2002**, 330-332, 696

8. Melendes, C.A.; Sy, C.C., *J. Electrochem. Soc.* **1978**, 125, 727

9. Brun, T.O.; Jorgensen, J.D.; Misawa, M.; Rotella, F.J.; Susman, S., *J. Electrochem. Soc.* **1982**, 129, 2509

10. Pulham, R.J.; Hubberstey, P.; Hemptenmacher, P., *J. Phase Equilibria* **1994**, 15, 587

11. Ding, F.; Liu, Y.; Hu, X., *Electrochem. Solid State Lett.* **2006**, 9, A72

12. Rioja, R.J.; Liu, J., *Metallurg. Mater. Transactions* **2012**, 43A, 3326

13. Kuriyama, K., *Acta Cryst. B* **1975**, 31, 1793

14. Zintl, E.; Brauer, G., *Z. Phys. Chem. B* **1933**, 20, 245

15. Tebbe, K.-F.; von Schnering, H.G.; Rütter, B.; Rabeneck, G., *Z. Naturforsch. B* **1973**, 28, 600

16. Hansen, D.A.; Smith, J., *Acta Crystallogr. B* **1968**, 24, 913

17. Müller, W.; Stöhr, J., *Z. Naturforsch. B* **1977**, 32, 631

18. Stöhr, J.; Schäfer, H., *Z. Naturforsch. B* **1979**, 34, 653

19. Schürmann, E.; Voss, H.-J., *Giessereiforschung* **1981**, 33, 33

20. Myles, K.M.; Mrazek, F.C.; Smaga, J.A.; Seetle, J.L., ERDA Report ANL-76-8, *Argonne National Laboratory* **1976**, pp. B50-B73

21. McAllister, A.J., *Bull. Alloy Phase Diagrams* **1982**, 3, 177

22. Hallstedt, B.; Kim, O., *Int. J. Mater. Res.* **2007**, 98, 961

23. Puhakainen, K.; Boström. M.; Groy, T.L.; Häussermann, U., *J. Solid State Chem.* **2010**, 183, 2528

24. Stöhr, J.; Müller, W.; Schäfer, H., *Z. Naturforsch. B* **1978**, 33, 1434

25. Häussermann, U.; Kranak, V.F.; Puhakainen, K., *Structure and Bonding*, Ed. Fassler, Springer-Verlag, Berlin, Germany, **2011**

26. Bruzzone, G.; Franseschi, E.; Merlo, F., *J. Less-Comm. Metals* **1978**, 60, 59

27. Wu, H.; Zhou, W.; Udovic, T.J.; Rush, J.J.; Yilderim, T., *Chem. Phys. Lett.* **2008**, 460, 432

28. Leon-Escamilla, F.A.; Corbett, J.D., *J. Solid State Chem.* **2001**, 159, 149

29. Leon-Escamilla, F.A.; Corbett, J.D., *Z. Inorg. Chem.* **2001**, 40, 1226

30. Wu, H.; Zhou, W.; Udovic, T.J. ; Rush, J.J., *Chem. Mater.* **2007**, 19, 329

31. Manfrinetti, P.; Fornasini, M.L.; Palenzona, A.; *Intermetallics* **2000**, 8, 223

CHAPTER 4

TRANSITION METAL HYDRIDES BY GIGAPASCAL HYDROGENATIONS

4.1 Introduction

Transition metal complex hydrides are a peculiar class of solid state compounds which consist of homoleptic hydrido complexes and an active metal. Typically, the transition metal (T) in the $[TH_m]^{n-}$ complex anion is from groups 7 to 10, and the active metal cation is either alkali, alkaline earth or rare earth metal.[1,2] The hydridic hydrogen ligand (H^-) is covalently bonded to the transition metal and perplexing range of coordination numbers (cn = 2– 9) and geometries are known to exist.[3]

An interesting feature is the occurrence of low formal oxidation states of T with a ligand (H^-) that does not afford the conventional "π-back-donation" mechanism. This is especially seen with the group 10 metals of nickel and palladium (i.e. tetrahedral NiH_4^{4-}, trigonal planar PdH_3^{3-}, or linear PdH_2^{2-} with zero-valent T). Tetrahedral complexes with zero-valent Ni and Pd displaying extraordinary weak T-H bonds.[4,5] On the other side of the spectrum are complexes with formally high oxidation states, e.g. Re(VII) in ReH_9^{2-}.[5] The actual bonding situations are complicated and often the cation environment is decisive in stabilizing these complexes.[6]

Thus far, most known complex hydrides have been prepared by hot sintering mixtures of active metal hydrides with the corresponding transition metal in hydrogen atmosphere employing autoclave techniques.[7] The oxidation state of the transition metal and its coordination number in the hydrido complex often relates to the hydrogen pressure applied. For example, below 10 MPa the formation of Na_2PdH_2 is observed but if higher pressure (~200 MPa) is applied it leads to the formation of $NaPdH_4$.[8,9] Na_2PdH_2 has a linear $[PdH_2]^{2-}$ complex whereas Na_2PdH_4 displays a square planar $[PdH_4]^{2-}$ complex. In the former complex, Pd attains formal oxidation state of zero, and in the latter complex the oxidation state of Pd is increased to +II [8,9] Another example of the pressure and the oxidation state correspondence is for the transition metal platinum. At hydrogen pressures below 1 MPa, formation of Na_2PtH_4 with square planar $[PtH_4]^{2-}$ complex is obtained while pressures in excess of 150 MPa promote the formation of Na_2PtH_6 displaying octahedral $[PtH_6]^{2-}$ complex.[10,11] The oxidation state of platinum in these complexes are Pt^{+II} and Pt^{+IV}, respectively.[10,11] Generally, high hydrogen pressures promote the realization of higher oxidation states. High oxidation states are also preferred when a heavier active metal is used to counterbalance the structure.[7]

Earlier hydrogenations at gigapascal pressures were used to synthesize binary hydrides of the middle and late transition metals using a toroid-type device.[12] This work was pioneered by Antonov, et al.,[13] When employing pressures between 1 and 9 GPa, these middle and late transition metals T form compounds $TH_{\sim 1}$ (e.g. FeH, MoH, NiH). These hydrides are recoverable and metastable at liquid nitrogen temperature.[13,14] Later Fukai, et al.,[15,16] applied MA techniques to study the formation of hydrides that contain a large number of transition metal vacancies (superabundant vacancies = SAV) at pressures above 5 GPa. In 2009, Saitoh, et al.,[17] were able to synthesize AlH_3 from the elements at pressure range from 6 to 10 GPa and temperatures between 300 to 800ºC also using MA techniques. However, attempts to prepare ternary hydrides using gigapascal hydrogenations have resulted in only few conclusively characterized results.[18-22]

As mentioned earlier, the commonly used hydrogen sources in the past have been alanates and borohydrides.[23,24] In this study, ammonia borane (BH_3NH_3) is exclusively used as an internal hydrogen source due to its high gravimetric volume of hydrogen and suitable thermal behavior.[25] In this study, multi-anvil hydrogenations are targeted toward a specific compound, Li_2PtH_6. The series of transition metal hydrides A_2PtH_6 (A = Na, K, Rb, Cs)[11,26,27] were synthesized by autoclave techniques using pressures up to 0.5 GPa.[2] The compounds A_2PtH_6 crystallize with the K_2PtCl_6-type structure (*Fm*-3*m*). Platinum, in the complex anion $[PtH_6]^{2-}$, has the oxidation state +IV.[11,26,27] Autoclave techniques could not produce an analogous lithium platinum hexahydride. Instead, the applied conditions yielded $Li_5Pt_2H_9$, with a complex ion $[Pt_2H_9]^{5-}$ that is built from two square planar $[PtH_4]^{2-}$ units bridged hydridic H^-.[28] In $Li_5Pt_2H_9$, the oxidation state of platinum is +II whereas in A_2PtH_6 Pt has oxidation state +IV. Based on comparative analysis of the A_2PtH_6 compound series and a detailed study of the vibrational properties of Rb_2PtH_6 and Rb_2PtD_6, it was predicted that Li_2PtH_6 would be accessible at higher pressures.[29] In this study, it was investigated if Li_2PtH_6 can be accessed by gigapascal MA hydrogenations.

4.2 Synthesis of Platinum Hexahydrides

The gigapascal MA hydrogenations employed ammonia borane as internal hydrogen source and were carried out in a 6-8 Walker-type multi-anvil module.[30] The details are presented in the Chapter 2.

First, the known compound Na_2PtH_6 was synthesized, for testing and comparison purposes, using NaH (Aldrich, powder, 95%) and Pt (Alfa Aesar, powder, 99.95%). A stoichiometric ratio of NaH and Pt was applied, and the ratio 1:6.66 between Pt and BH_3NH_3 was chosen. Subsequently, the Li_2PtH_6 was synthesized for the first time by reacting LiH (Aldrich, powder, 95%) and Pt (Alfa Aesar, powder, 99.95%). The ratio of LiH:Pt:BH_3NH_3 was 3:1:3.33. Attempts to synthesize a deuterium analog of Li_2PtH_6 lead to the formation of a heteroleptic $Li_2PtD_nH_{6-n}$. The ratio of LiD:Pt:BD_3ND_3 used in the synthesis was 3:1:3.33. Mixtures of metal hydride (deuteride) and Pt were pressed into a pellet with total mass of 100 mg.

The deuterium source, BD_3ND_3, was obtained by reacting $NaBD_4$ with ammonium formate, and D_2O was used to replace amine protons by deuterium.[31] As was later discovered, the replacement of hydrogen by deuterium was incomplete which led to a heteroleptic complex formation. In Chapter 2, the details of precursor LiD synthesis are presented.

The salt (NaCl) capsule was filled and sealed inside the Ar-filled glovebox under air and moisture-free conditions and taken out from the glove box to prepare the MA assembly. The salt capsule was used as it resist the diffusion of hydrogen (see Chapter 2 for details). After applying the synthesis conditions using the Walker-type multi-anvil module[30], the octahedron was removed from the hydraulic press and transported into the glovebox to recover the sample in air and moisture-free conditions (Ar-filled glovebox). Usually, the three pellet (sandwich) setup was well recognizable after opening the salt capsule with a sharp tool. Decomposed hydrogen source pellets (BN) were easily removed from both sides of the brittle sample pellet. Occasionally some salt was tightly attached to the sample pellet. There was no indication based on the sample appearance (or later using x-ray diffraction data) that any reactions between boron or nitrogen (from the decomposed hydrogen source) and the sample would occur.

A varying range of pressures and temperatures were applied to the samples and a previously known Na_2PtH_6, and novel Li_2PtH_6 and $Li_2PtH_{1.5}D_{4.5}$ were synthesized. The results will be discussed later in this chapter.

4.2.1 Synthesis of Known Na_2PtH_6 to Optimize High-pressure Hydrogenation Conditions

The transition from the autoclave to the multi-anvil synthesis involves transitioning from a large volume of molecular hydrogen to use of an internal thermally decomposing hydrogen source. In the latter case hydrogen activity does not directly relate to applied pressure as it does in the autoclave synthesis. However, in the autoclave synthesis pressures above 0.5 GPa cannot be achieved whereas in MA technique pressures up to 10 GPa can easily be achieved.[32] This is a remarkable advantage as at 1 GPa the activity of the hydrogen fluid increases very sharply (as described in Chapter 1) opening the possibility to access phases and materials not yet known to be prepared any other way.[33,34]

Due to differences in autoclave and multi-anvil hydrogenation methods NaH-Pt system was treated as a testing system. It has several well known complex hydrides: Na_2PtH_2, Na_2PtH_4 and Na_2PtH_6 which have Pt at oxidation states 0, +II and +IV, respectively.[10,11,27] A series of experiments to synthesize Na_2PtH_6 from NaH and platinum powder (2NaH:Pt) were performed in order to find the optimal synthesis conditions for the gigapascal MA hydrogenations. The molar ratio of transition metal and hydrogen was varied between 1:10 to 1:40 (Pt:H). Pressure and temperature conditions between 1.5 to 5 GPa and 500 to 800 ˚C, respectively, were applied. Under conditions of 500 ˚C (2 hour dwell time) and 5 GPa, it was observed that hexahydride, Na_2PtH_6, was formed whereas at other conditions Na_2PtH_4 was obtained.

Using the powder x-ray diffraction (PXRD) it was confirmed that the well crystalline Na_2PtH_6 was obtained (Figure 4.1). During the measurement the sample was kept protected from the air and moisture by covering it with Kapton tape (details in Chapter 2).

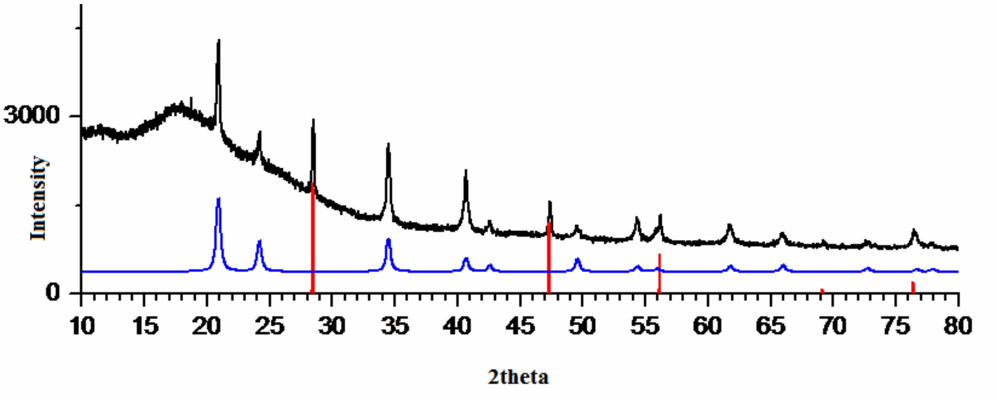

Figure 4.1. Experimental Na_2PtH_6 (5 GPa and 500˚C) compared to the theoretical pattern (blue) of Na_2PtH_6 reported in the literature.[11] Silicon (red) added for unit cell parameter refinement purposes.

4.2.2 Synthesis of Li_2PtH_6 and $Li_2PtH_nD_{6-n}$

Conditions used to obtain Na_2PtH_6 were employed as a starting point in search of a missing start member, Li_2PtH_6, of A_2PtH_6 series (A = Na to Cs)[26,27]. As predicted, the lithium analog was accessible when higher pressure was applied.[29] At pressures above 8 GPa and temperatures between 450 and 500 ˚C, the Li_2PtH_6 product readily formed.[35] The ratio of reaction mixture LiH:Pt:BH_3NH_3 was 3:1:3.333 which gave about 80% yield of the Li_2PtH_6 product. Intermetallic $LiPt_7$ (simple fcc structure)[36] was identified as a side product. Li_2PtH_6 does also form when stoichiometric (2LiH:Pt) is used and/or at lower pressures (down to 5 GPa), but the amount of the side product substantially increases compared to non-stoichiometric starting composition of LiH and Pt (3LiH:Pt).

The isotopologue BD_3ND_3 can be prepared[31,37] to gain access to the deuterized samples for neutron diffraction studies to refine light atom H/D positional parameter. Deuterized samples (3LiD:1Pt:3.333BD_3ND_3) can be synthesized at high pressures above 8 GPa. The large volume of sample needed for neutron diffraction studies would be achieved easier if the high yield 25/15 assembly (instead of 18/12) could be utilized. However, the attainable maximum pressure using 25/15 assembly is ~ 7 GPa[32] which is not sufficient for Li_2PtD_6 preparation. Also, as later will be discussed, the replacement of hydrogen by deuterium was incomplete in deuterized ammonia borane. Therefore, a heteroleptic $Li_2PtH_nD_{6-n}$, was obtained instead of fully deuterized sample.[35]

4.3 Structural Analysis of Li_2PtH_6

According to its powder diffraction pattern Li_2PtH_6 is isostructural to the known heavier analogs of A_2PtH_6 series (Na to Cs),[26,27] which crystallize in the cubic K_2PtH_6-type structure (*Fm*-3*m*, Table 1.1). In addition to a highly crystalline Li_2PtH_6, a poorly crystalline side product $LiPt_7$[36] is obtained. It appears that the formation of the side product competes with the formation of Li_2PtH_6 and the latter is favored by applying an excess of LiH and higher pressures. However, further increasing the excess of LiH:Pt > 3:1 did not improve the yield of Li_2PtH_6. At 8 GPa and 450 °C, a highly crystalline Li_2PtH_6 was formed (Figure 4.2).

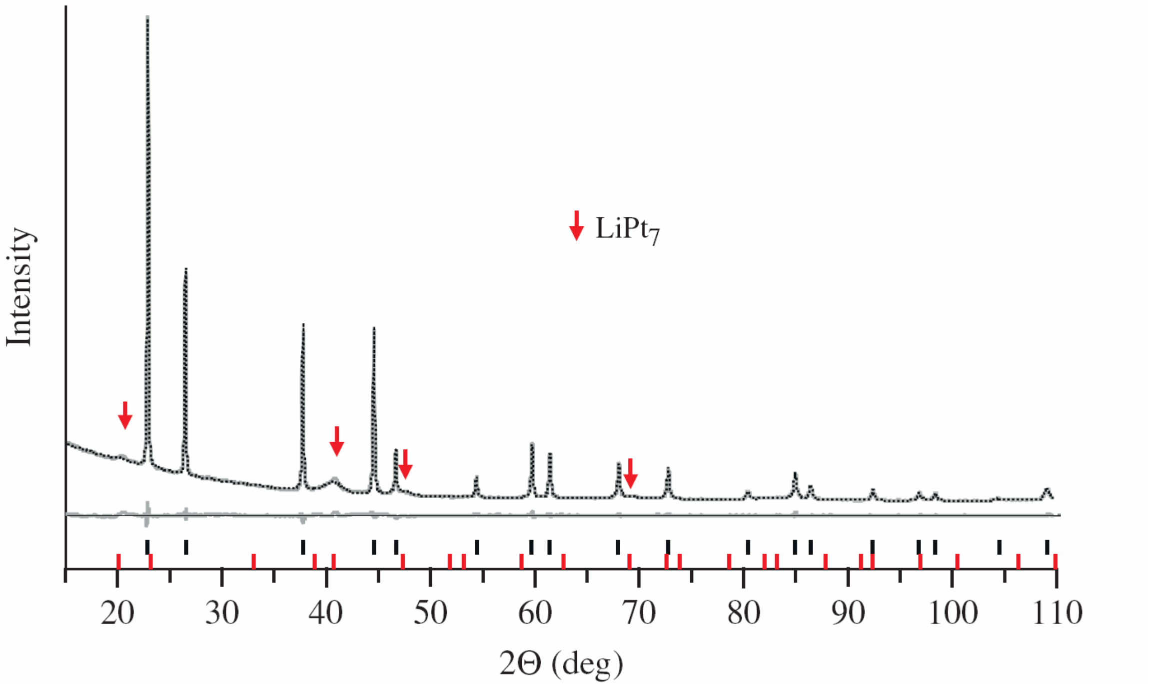

Figure 4.2. Rietveld fit to the x-ray diffraction pattern of Li_2PtH_6 (Cu$K\alpha_1$).[35]

In Figure 4.2, the horizontal bars represent the positions of the Bragg peaks of the main product Li_2PtH_6 (black) and the side product $LiPt_7$ (red). The grey line represents the measured pattern and the dotted black line the calculated pattern. According to the x-ray diffraction pattern, Li_2PtH_6 is isostructural to the heavier homologues of A_2PtH_6 (A = Na to Cs)[26,27] which crystallize in the cubic K_2PtCl_6 structure type (*Fm*-3*m*). The lattice parameter of Li_2PtH_6 is 6.76811(3) Å.[35]

Table 4.1 Li_2PtH_6: crystal data and structure refinement.[41]

Compound	Li_2PtH_6
Space group	*Fm*-3*m*
Z	4
a (Å)	6.7681(30
V (Å^3)	310.0(1)
T (K)	295
χ^2	1.73
R_p (%)	2.84
R_{wp} (%)	3.78
R_B (%)	1.22

This structure corresponds to a CaF_2-type arrangement of $[PtH_6]^{2-}$ octahedral units and alkali metal (A) cations which are coordinated by 12 H-ions, i.e. by four tetrahedrally arranged faces from four different octahedral (Figure 4.3). Accordingly, the platinum and alkali metal atoms (A) occupy the special positions, 4a (0,0,0) and 8c (¼,¼,¼), respectively. Hydrogen atom position represents the only flexible structural parameter 24e (x,0,0), in the unit cell.

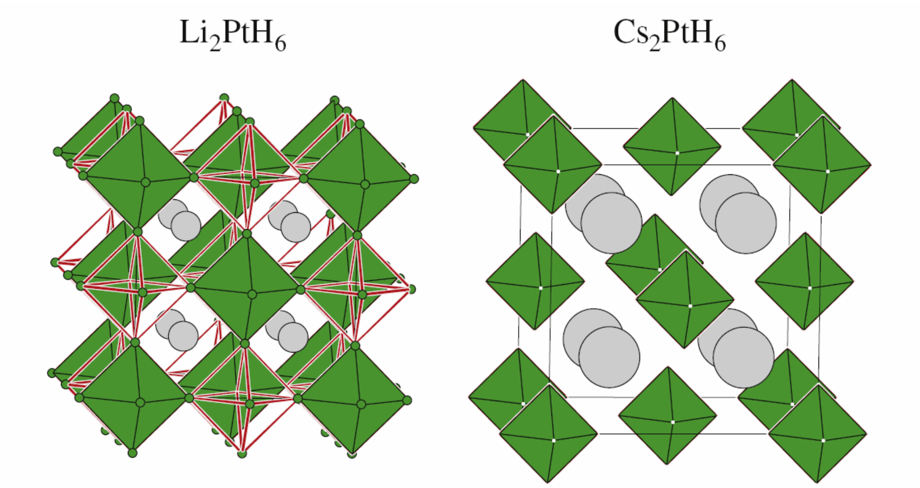

Figure 4.3. Li_2PtH_6 and Cs_2PtH_6 structures. Lithium/cesium cations (grey) balance the $[PtH_6]^{2-}$ complexes (green).[35]

Although deuterized samples, from the $LiD/Pt/BD_3ND_3$, can be synthesized using the same conditions as Li_2PtH_6, the high pressures (> 8 GPa) necessary for obtaining high yield samples prohibited the preparation of sample volume large enough for neutron diffraction measurements. The highest volume assembly (25/15 assembly) could not be employed as it has the maximum pressure limit at around 7 GPa. Therefore, the H/D atom positional parameter could not be determined experimentally. Instead, the first-principles calculations using the density functional theory were performed to optimize the K_2PtCl_6 structure for Li_2PtH_6. Figure 4.4 summarizes the results. The projected augmented wave (PAW) method was performed as implemented in the program VASP.[38-41] The generalized gradient approximation (GCA) was used to treat exchange and correlation effects.[42] The integration over Brillouin zone was done over a Monkhorst-Pack grid (15x15x15).[43] Total energies were converged to at least 1 meV per atom. The H atom positional parameter was optimized for fixed volume of the unit cell (all A_2PtH_6 systems). The equilibrium cell and positional parameter were determined from the global minimum energy by repeating the calculation process for different volumes.

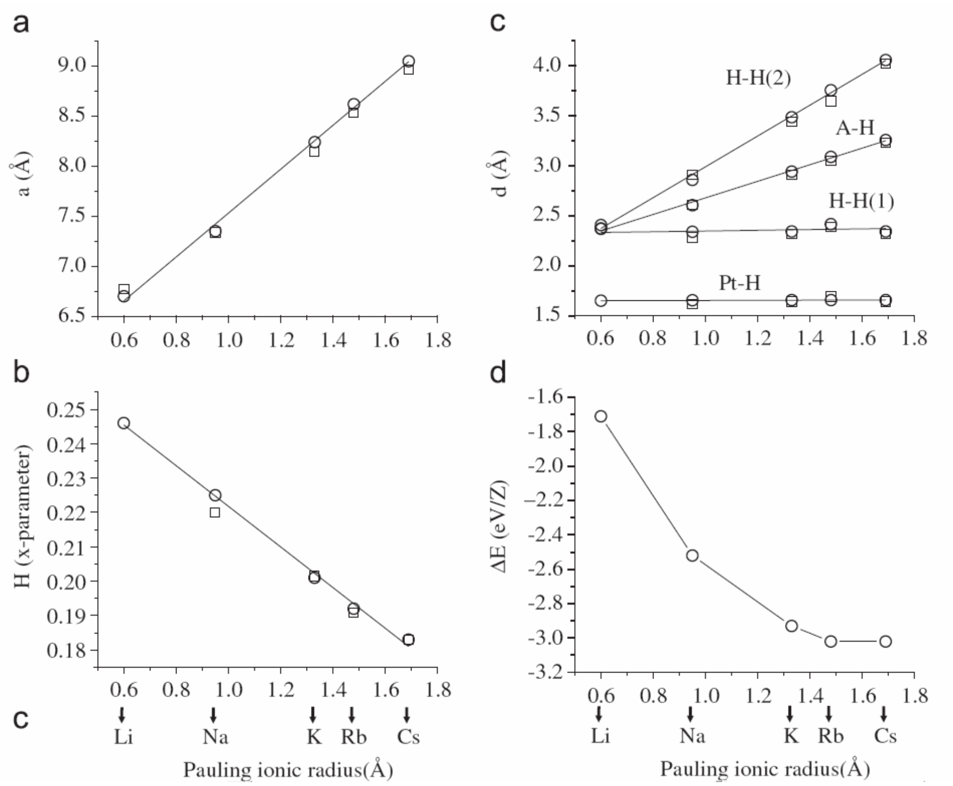

Figure 4.4 The structural trends in relation to Pauling ionic radii. In addition to lattice parameter (a), H atom position (b), interatomic distances (c) for series of A_2PtH_6 as a function of Pauling ionic radius of alkali metal (A), the computed zero-temperature formation energy (d) is shown. Theoretical values are denoted in circles and experimental values in squares.[35]

The structural trend in the series of A_2PtH_6 (Figure 4.4a–c) correlates well with the Pauling ionic radii of alkali metal (A). As suggested earlier by Parker, et al.,[29] the theoretical and experimental (when available) values are in good agreement. In particular, the lattice parameter decreases linearly with the decreasing size of the ionic radius of A. The H atom x parameter increases linearly and approaches ¼ (calculated value 0.246) for A = Li.[35] This leads to a peculiar situation when analyzing interatomic distances (Figure 4.4c). The Pt-H distance in the octahedral complex ion is around 1.65 Å and virtually not affected by A. As a consequence, distances between H atoms within the octahedral units (H-H1)) and in between (H-H(2)) which are considerably different for alkali metal from sodium to cesium, become almost identical for Li_2PtH_6 (2.35 Å and 2.43 Å, respectively). As matter of fact, the substructure of H atoms in Li_2PtH_6 approaches closely that of O atoms in the cubic perovskite structure and Li attains almost regular cuboctahedral coordination by H atoms. In structural respect this causes hydrogen atoms to obtain similar substructure as oxygen in a cubic perovskite. Therefore, the Li_2PtH_6 structure can be considered as a defective perovskite structure where half of the octahedrally coordinated (cations) are missing. The tilting of octahedral units in cubic perovskite (ABO_3) is commonly known to occur. If the tolerance factor, t, is between 0.9 to 1, there is no tilting in octahedral units expected. The ratio of the effective ionic radii of r_A, r_B and r_o can be used to determine the tolerance factor.[44]

$$t = (r_A + r_O) / \sqrt{2}(r_B + r_O) \qquad \textit{Equation 4.1}$$

Shannon ionic[45] radius for 6-coordinated Pt^{+IV} (0.625 Å) and approximated Li^+ radius (1.08 Å) was used. The latter was extrapolated by adjusting the known 8-coordinated Li^+ Shannon ionic radius (0.92 Å) using the ratio between known 8- and 12-coordinated radii of Na^+.[45] The effective ionic radius of H^- (1.3 Å) was estimated based on effective H^- radius in known NaCl-type alkali metal hydrides LiH and KH (1.4 Å and 1.2 Å, respectively) in which the alkali metal has a rigid radius.[46] Calculations (Equation 4.1) yield tolerance factor value of ~ 0.9 which is close to the ideal value and no distortion or tilting of the octahedral units PtH_6^{2-} in Li_2PtH_6 compound is predicted to appear. Therefore, in spectroscopic analysis splitting of the spectral lines (Pt-H stretching modes) is not expected.

The "strained" situation of Li_2PtH_6 structure is also apparent when comparing computed formation energies (referring to 0 K) for the reaction $2AH + Pt + 2H_2 \rightarrow Li_2PtH_6$ (Figure 4.4d). For alkali metals K, Rb and Cs the values are very similar, around -3 eV. It slightly decreases to -2.5 eV for Na and becomes just -1.7 eV for Li_2PtH_6. The temperature-dependent Gibbs free energy, $\Delta G_T(H_2)$, for H_2 gas molecule is around -0.32 eV at 300 K.[47] Therefore, Li_2PtH_6 should represent a thermodynamically stable compound at room temperature and ambient pressure.[48]

Spectroscopic properties of K_2PtH_6 and Cs_2PtH_6 have been previously extensively studied for both by optical (IR and Raman) and by inelastic neutron scattering (INS).[29,49,50] The findings from these studies are compared to our experimental findings of Na_2PtH_6, Li_2PtH_6 and "Li_2PtD_6" (Figure 4.5) as they provide an excellent reference point. The symmetry allowed vibrational modes for octahedral unit, $[PtH_6]^{2-}$, are shown in Table 4.2. The alkali metal platinum hexahydrides crystallizes in cubic space group (*Fm*-3*m*) with four formula units in the cell. In the Bravais cell (one formula unit) the A^+ ions are on tetrahedral sites, and the $[PtH_6]^{2-}$ ions are on octahedral O_h sites.

Table 4.2 Vibrational modes of A_2PtH_6 (A = alkalimetal). The notation R, IR and ia indicates Raman active, IR active and inactive mode, respectively.

Pt-H stretches	A_{1g} (R) + E_g (R) + T_{1u}(IR)
Pt-H bends	T_{2g} (R) + T_{1u} (IR) + T_{2u} (ia)
Libration	T_{1g} (ia)
Translation	T_{2g} (R) + T_{1u} (IR)
Acoustic	T_{1u} (ia)

The investigated products display the octahedral anionic complex, and the stretching and bending mode frequencies of the Pt-H bonds of the different complexes are compared. The Na_2PtH_6 spectrum (Figure 4.5a) shows the expected T_{1u} (asymmetric) Pt-H stretching mode at 1793 cm^{-1} which appears peculiarly split (1681, 1735 and 1793 cm^{-1}). In exactly same way, the splitting has been observed for platinum hexahydrides of the heavier alkali metals K and Rb.[48] This feature has been lately attributed to extra bands that are observable because of Fermi resonance.[47] When going from the Rb (1743 cm^{-1}) to the K (1748 cm^{-1}) compound, the Pt-H stretching mode increases slightly.[48] This trend continues with Na (1793 cm^{-1}) compound, however, the amount of increase is substantially larger. The Pt-H stretching mode for Li_2PtH_6 appears at 1840 cm^{-1} (Figure 4.5b) which represents a further substantial increase compared to Na_2PtH_6.

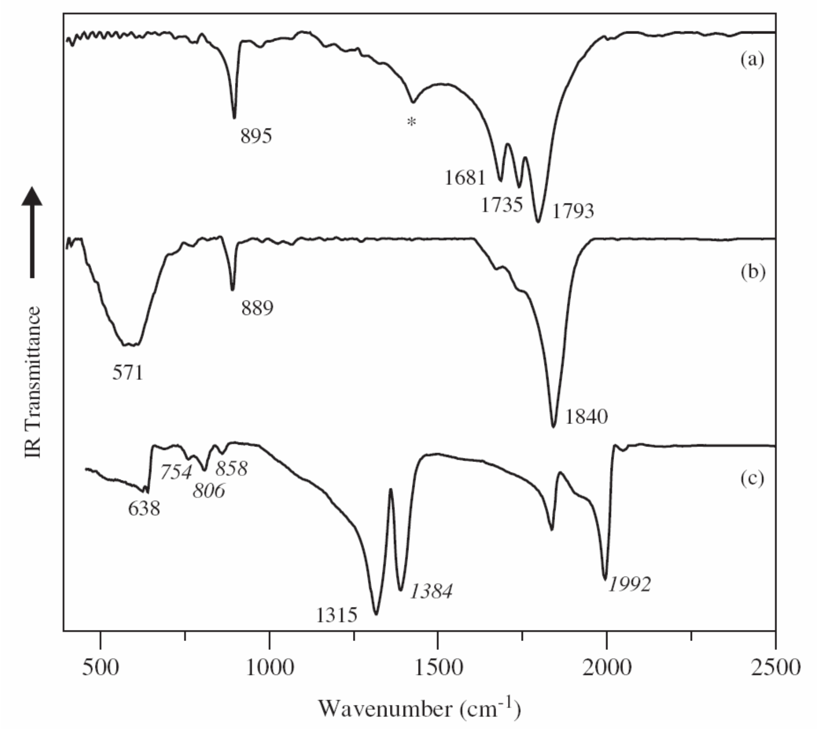

Figure 4.5. IR spectra of Na_2PtH_6 (a), Li_2PtH_6 (b) and "Li_2PtD_6" (c). The asterisk in spectrum (a) denotes an impurity associated with the decomposition of extremely air/moisture sensitive Na_2PtH_6. Italicized wavenumbers in spectrum (c) refer to modes for heteroleptic $[PtH_nD_{6-n}]^{2-}$. The unlabeled mode at 1840 cm^{-1} in spectrum (c) belongs to $[PtH_6]^{2-}$.

The observed Pt-H stretching and bending modes are shown in Table 4.3. The Pt-H bonding modes display a similar trend (increases as cation size decreases) as Pt-H stretching modes from the Rb to the Na compound. However, the frequency of the Pt-H bending mode in the Li compound (889 cm^{-1}) is lower than that for the Na compound (895 cm^{-1}).

Table 4.3 Pt-H T_{1u} stretching and bending modes (cm^{-1}) for A_2PtH_6 (A = Li to Cs) as observed by IR spectroscopy. Values for Li and Na compounds from this study and for heavier analogs form references (29, 48-50).

	stretching	bending
Li_2PtH_6	1840	889
Na_2PtH_6	1793	895
K_2PtH_6	1748	881
Rb_2PtH_6	1743	877

The feature of additional bands accompanying the stretch which is characteristic for the heavier homologues, is only vaguely recognizable for the Li_2PtH_6.[29,49] The lack of additional bands (Figure 4.5b) was also supported by tolerance factor calculation (*Equation* 4.1, p. 69) which yielded close to ideal value (~ 0.9) for the Li_2PtH_6. The most obvious difference compared to the heavier homologues is the occurrence of a broad and intense band appearing at low frequencies (with a maximum around 571 cm^{-1}). The origin of this band is not clear. It is unlikely that it relates to libration or translation modes. Librations (or torsions) of PtH_6^{2-} octahedra are inactive in optical spectroscopy for the heavier homologues. In the INS spectrum of Rb_2PtH_6, the libration mode is at 366 cm^{-1} and translational modes are observed at remarkably lower frequencies (~100 cm^{-1}).[29,49] Although the translation has IR active T_{1u} component and the mass difference between lithium and rubidium is significant, its frequency should not raise above 400 cm^{-1} ($\sqrt{m_{Rb}}/\sqrt{m_{Li}} \sim 3.5$). Therefore, the band at 571 cm^{-1} is attributed to an impurity of the side product $LiPt_7$ which could have hydrogen incorporated into structure ($LiPt_7H_x$).

The spectrum of "Li_2PtD_6" (Figure 4.5c) reveals the presence of heteroleptic D/H complexes. Apparently, the deuterium source BD_3ND_3 used for its synthesis had not been completely proton-exchanged. Earlier Bubliz, et al.,[50] prepared purposely a series of mixed complexes $K_2PtH_nD_{6-n}$ for spectroscopic studies. Based on their results the bands at 1991 and 1384 cm^{-1} can be assigned to Pt-H strechinchg modes in heteroleptic $Li_2PtH_nD_{6-n}$. It is important to notice that heteroleptic complexes have a reduced symmetry and the symmetric stretching modes A_{1g} and E_g in O_h symmetry, that are exclusively Raman active (at higher and lower wavenumbers, respectively, than the T_{1u} mode) become IR active. The bending modes of such complexes appear in the region of 700 to 900 cm^{-1}. The Pt-D stretching mode for homoleptic Li_2PtD_6 is at 1315 cm^{-1} (corresponding to homoleptic shift of 1.399), while the bend should coincide with the sharp edge of the broad intensity feature at low frequencies. The edge is 638 cm^{-1} (corresponding to anisotropic shift of 1.393); the bending mode is camouflaged by what is probably a broad impurity band. The intensity ratio of stretching modes stemming from heteroleptic $[PtH_nD_{6-n}]^{2-}$ and homoleptic PtD_6^{2-} complexes in the IR spectrum of Figure 4.5c matches very well with that for $K_2[PtH_{1.5}D_{4.5}]^{2-}$ reported by Bublitz, et al.[50] Thus, it is assumed that here obtained isotopomer has similar compositions. IR spectra of homoleptic K_2PtH_6 and K_2PtD_6 are shown in Figure 4.6a and Figure 4.6d, respectively. The heteroleptic $K_2PtH_nD_{6-n}$ where n = 4.72 and n = 1.49 are shown in Figure 4.6b and Figure 4.6c, respectively.[50]

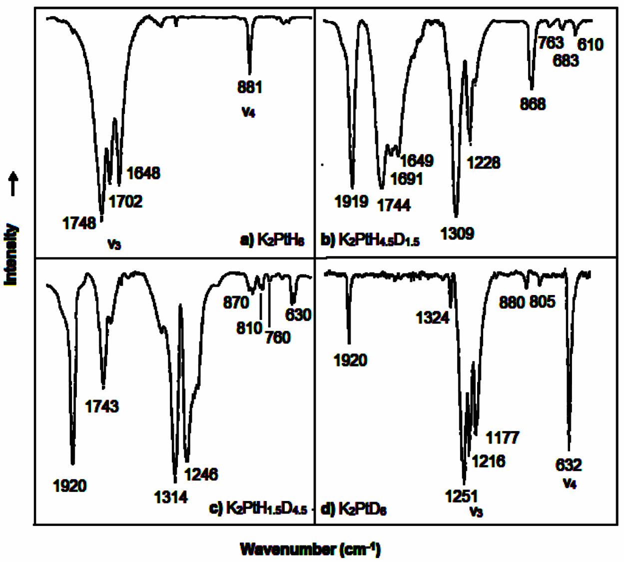

Figure 4.6. The IR spectra of homoleptic K_2PtH_6 (a), homoleptic K_2PtD_6 (d) and heteroleptic $K_2PtH_nD_{6-n}$ where n = 1.49 (c) and n = 4.72 (b).[50]

For thermal decomposition experiments 10 – 20 mg amounts of Li_2PtH_6 sample were pressed into a pellet, which was loaded into a sealable stainless steel container in the glovebox. The steel container was heated under argon atmosphere (0.1 MPa) for 20 hours at varied temperatures. The decomposition products were analyzed using x-ray diffraction (Table 4.4).

Table 4.4 The decomposition products of Li_2PtH_6 (T = 150 - 300°C).[35]

T (˚C)	Decomposition product
150	Li_2PtH_6
200	fcc-Pt (broad)
250	fcc-Pt (sharpened)
300	Li_yPtH_x, $LiPt_7$

Li_2PtH_6 decomposes between 150 and 200 °C when heating in a 0.1 MPa argon atmosphere for 20 hours. The x-ray powder pattern of the decomposition product obtained at 200 °C shows very broad reflections which can be related to fcc-Pt. These reflections constitute – somewhat sharpened – also the pattern of the 250 °C decomposition product. When decomposing Li_2PtH_6 at 300 °C, a trigonal Li_yPtH_x,[51] LiH and small amount of $LiPt_7$ can be identified in the powder pattern of the product. Thus, the thermal behavior of Li_2PtH_6 is different from the $Li_5Pt_2H_9$ which decomposes quantitatively to Li_2PtH_2 (with zero-valent Pt) and LiH at 220 ˚C when applying the same conditions.[50] Further decomposition of Li_2PtH_2 into Li_yPtH_x at

280 ˚C.[51,52] The thermal decomposition behavior of Li_2PtH_6 was found to differ from the decomposition path of $Li_5Pt_2H_9$. Finally, somewhat surprising is the observation that the Li_2PtH_6 degrades only slowly outside of the glove box while the heavier homologues are extremely air and moisture sensitive.

4.4 Conclusions

It was shown that Li_2PtH_6, the missing member of the complex transition metal hydride series A_2PtH_6 (A = Na to Cs)[26,27], was readily obtained from LiH and Pt precursors by MA gigapascal hydrogenations when employing pressures above 8 GPa and temperatures between 450 to 500 ºC. According to the powder x-ray diffraction analysis, the Li_2PtH_6 is isostructural to its heavier homologues and crystallize in a cubic K_2PtCl_6-type structure (*Fm*-3*m*). The lattice parameter of Li_2PtH_6 is 6.76811(3) Å.[35]

However, whereas PtH_6^{2-} octahedral complexes are well separated for the heavier homologues, H-H distances within and between the octahedral complexes become almost equal for Li_2PtH_6. Therefore, the Li_2PtH_6 structure may likewise be regarded as a defective perovskite structure with half of the octahedrally coordinated (cations) occupied. The PtH_6^{2-} complex is a classic 18-electron system adopting an octahedral symmetry. The central atom Pt^{+IV} has d^6 valence-electron configuration, and the complex displays σ-bonds between Pt and H.

The positional hydrogen atom parameter x was calculated using the density functional theory and it was found that x parameter value follows a linear trend in the series of A_2PtH_6 compounds (A = alkali metal). As the alkali metal size decreases, the hydrogen positional parameter x increases. The theoretical and experimental (when available) values were in good agreement.[35]

Based on the IR spectroscopy, it was found that the Pt-H stretching mode of Li compound (1840 cm^{-1}) is at higher frequency than for the heavier homologues. Using the IR spectroscopy, the composition of a heteroleptic compound was determined to be $Li_2PtH_{1.5}D_{4.5}$. The homoleptic deuterium analog was not achieved due to incomplete proton-exchange when synthesizing BD_3ND_3. However, deuterium analog $Li_2PtH_nD_{6-n}$ was readily obtainable at similar conditions as Li_2PtH_6 (> 8 GPa, 450 ºC).[35]

Ammonia borane was introduced as an internal hydrogen source and did not react with precursor, product or sample capsule material. The advantage of gigapascal hydrogenations is the increased activity of hydrogen above 1 GPa.[33,34] The increased activity was crucial and provided a way to obtain the Li_2PtH_6.

4.5 References

1. Yvon, K., *Chimia* **1998**, 52, 613
2. Bronger, W., *J. Alloys Compd*. **1995**, 229, 1
3. Firman, T.K.; Landis, C.R., J. *Am. Chem. Soc.* **1998**, 120, 12650
4. Olofsson-Mårtensson, M.; Häussermann, U.; Tomkinson, J.; Noreus, D., *J. Am. Chem. Soc*. **2000**, 122, 6960
5. King, R.B.; *Coord. Chem. Rev*. **2000**, 200-202, 813
6. Häussermann, U.: Blomqvist, H.; Noreus, D., *Inorg. Chem*. **2002**, 41, 3684
7. Bronger, W.; Auffermann, G., *Chem. Mater*. **1998**, 10, 2723
8. Noreus, D.; Törnroos, L.W.; Börje, A.; Szabo, T.; Bronger, W.; Spittank, H.; Auffermann, G.; Müller, P., *J. Less-Common Met*. **1988**, 139, 233
9. Bronger, W.; Auffermann, G., *J. Alloys Compd*. **1995**, 228, 119
10. Bronger, W.; Müller, P.; Schmitz, D.; Spittank, H., *Z. Anorg. Allg. Chem*. **1984** , 516, 35
11. Bronger, W.; Auffermann, G.; *J. Alloys Compd*. **1995**, 219, 45
12. Khvostantsev, L.G.; Slesarev, V.N.; Brazhkin, V.V., *High Pressue Res*. **2004**, 24, 371
13. Antonov, V.E., *J. Alloys Compd*. **2002**, 330-332, 110

14. Antonov, V.E.; Baier, M.; Dorner, B.; Fedotov, V.K.; Gosse, G.; Kolesnikov, A.I.; Ponyatovsky, E.G.; Schnider, G.; Wagner, F.E., *J. Phys. Condens. Matter* **2002**, 14, 6427

15. Fukai, Y.; Sugimoto, H., *J. Phys.: Condens. Matter* **2007**, 19, 436201

16. Fukai, Y.; Okuma, N., *Phys. Rev. Lett*. **1994**, 73, 1640

17. Saitoh, H.; Machinda, A.; Katayama, Y.; Aoki, K., *Appl. Phys. Lett*. **2008**, 93, 151915

18. Rönnebro, E.; Kitamura, N.; Sakai, T.; *J. Alloys Compd*. **2003**, 358, 216

19. Chen, J.; Sakai, T.; Kitamura, N.; Takeshita, H.T.; Kuriyama, N., *J. Am. Chem. Soc.* **2001***,* 123, 6193

20. Kamegawa, A.; Goto, Y.; Kataoka, R.; Takamura, H.; Okada, M., *Renew. Energy* **2008***,* 33, 221

21. Takamura, H.; Kakuata, H.; Goto, Y.; Kamegawa, A.; Okada, M., *Mater. Trans*. **2001**, 42, 1301

22. Kyoi, D.; Sato, T.; Rönnebro, E.; Kitamura, N.; Ueda, A.; Ito, M.; Katsuyama, S.; Hara, S.; Noréus, S.; Sakai, T., *J. Alloys Compd*. **2004**, 372, 213

23. Schüth, F.; Bogdanovic, B.; Felderhoff, M., *Chem. Commun.* ***2004,*** 2249

24. Li, C.; Peng, P.; Zhow, D.W.; Wan, L., *Int. J. Hydrogen Energy* **2001**, 36, 14512

25. Nylén, J.; Sato, T.; Soingnard, E.; Yarger, J.L.; Stoyanov, E.; Häussermann, U., *J.Chem. Phys*. **2009**, 131, 104505

26. Bronger, W.; Auffermann, G., *Angew. Chem. Int. Ed*. **1994**, 33, 1112

27. Bronger, W.; Brassard, L.A., *Z. Anorg. Allg. Chem*. **1995**, 621, 1318

28. Bronger, W.; Brassard, L.A., *Angew. Chem. Int. Ed*. **1995**, 34, 898

29. Parker, S.F.; Bennington, S.M.; Ramirez-Cuesta, A.J.; Auffermann, G.; Bronger, W.; Herman, H.; Williams, K.P.J.; Smith, T., *J. Am. Chem. Soc*. **2003** , 125, 11656

30. Walker, D.; Carpenter, M.A.; Hitch, C.M., *Am. Mineral* **1990**, 75,1020

31. Hu, M.G.; van Paasschen, J.M.; Geanangel, R.A., *J. Inorg. Nucl. Chem*. **1977**, 39, 2147

32. Stoyanov, E.; Häussermann, U.; Leinenweber, K.*, High Pressure Res*. **2010**, 30, 175

33. Hemmes, H.; Driessen, A.; Griessen, R.J., *C. Phys. Solid State Phys*. **1986**, 19, 3571

34. Driessen, A.; Sänger, P.; Hemmes, H.; Griessen, R.J., *J. Phys. Condens. Matter* **1990**, 2, 9797

35. Puhakainen, K.; Stoyanov, E.; Evans, M.J.; Leinenweber, K.; Häussermann, U., *J. Solid State Chem.* **2010**, 183, 1785

36. Bronger, W.; Klessen, G.; Müller, P., *J. Less-Common Met*. **1985**, 109, L1

37. Lin, Y.; Mao, W.L.; Drozd, V.; Chen, H.H.; Daemen, L.L., J*. Chem. Phys.* **2008**,129, 234509

38. Blöch, P.E., *Phys. Rev*. *B* **1994**, 50, 17953

39. Kresse, G.; Joubert, J., *Phys. Rev*. *B* **1999**, 59, 1758

40. Kresse, G.; Hafner, J., *Phys. Rev*. B **1993**, 47, 558

41. Kresse, G.; Furthmüller, J., *Phys. Rev*. B **1996**, 54, 11169

42. Perdew, J.P.; Wang, J., *Phys. Rev*. B **1992**, 45, 13244

43. Monkhorst, H.J.; Pack, J.D., *Phys. Rev*. B **1976**, 13, 5188

44. Johansson, M.; Lemmens, P., *J. Phys.; Condens. Matter* **2008**, 20, 264001

45. Shannon, R.D., *Acta Cryst.* **1976**, A32, 751

46. Ivanovic, N.; NOvakovic, N.; Colognesi, D.; Radisavljevic, I.; Ostojic, S., *Int. J. Mod. Phys. B* **2010**, 24, 703

47. Ke, X.; Tanaka, I., *Phys. Rev. B* **2005**, 71, 024117

48. This estimate neglects zero point energies, the effect of pressure and the temperature dependence of the internal energy.

49. Parker, S.F., *Coord. Chem. Rev*. **2010**, 254, 215

50. Bublitz, D.; Peters, G.; Preetz, W.; Auffermann, G.; Bronger, W., *Z. Anorg. Allg. Chem*. **1997**, 623, 184

51. Nacken, B.; Bronger, W., *J. Less-Common Met*. **1977**, 52, 323

52. Bronger, W.; Brassard, L.A., *Z. Anorg. Allg. Chem*. **1996**, 622, 462

CHAPTER 5

MAIN GROUP HYDRIDES BY GIGAPASCAL HYDROGENATIONS

5.1 Introduction

As discussed earlier (Chapters 1 and 3), Zintl phases are defined as compounds between an active metal (alkaline, alkaline earth, rare earth) and a p-block metal/semimetal.[1] Hydrogenations of Zintl phases can lead to hydrogenous Zintl phases which can be divided into interstitial or polyanionic hydrides.[2] Polyanionic hydrides represent the intermediate stage to completely hydrogenated complex main group metal hydrides (Figure 3.1). Completely hydrogenated products are rarely observed with autoclave hydrogenations. Applying gigapascal pressures will likely increase the propensity to obtain complex hydrides (as in the case of transition metal complex hydrides).

5.2 Hydrogen-dominant Materials Based on Silicon

In 1968 Ashcroft[3] predicted that metallic hydrogen could be superconducting at room temperature. Recent theoretical investigations indicated that pressures around 400 GPa are needed to transform hydrogen into a superconducting state (T_c = 230 K).[4] Hydrogen-dominant materials were proposed to become superconductors at lower pressures.[5] Indeed, SiH_4, was found to become superconducting at T_c = 17 K (96 GPa) by Eremets, et al.,[5] in 2008. This metallic modification of SiH_4 is not recoverable at ambient pressure, but its discovery encouraged research into ternary silicon hydrides with potential superconducting properties.[6]

The major focus of this study is on gigapascal hydrogenations of the main group element silicon combined with alkali metals (Na, K, Rb). The known halide analogs have been useful in predicting the possible synthesis products for these hydrides. There is an existing series of A_2SiF_6 (A = alkali metal) which crystallize in the cubic K_2PtCl_6-type structure.[7] However, fluorine is a much more electronegative ligand than hydrogen and a large electronegativity difference between central atom and ligand is favorable for stabilizing hypervalent bonding. The electronegativity of hydrogen is similar to p-elements and hydrogen is rarely observed as a ligand in hypervalent species.[8,9]

Originally hypervalency was defined by Musher[10] in the late-'60s to classify the hypervalent molecules as those formed of group 15 to 18 elements in any of their stable valence state higher than 3, 2, 1 and 0, respectively. In 2002, Noury, et al.,[11] simplified the definition of a hypervalent compound as a (main group) molecule that attains more than four electron pairs around the central atom. For silicon, a range of pentacoordinated hydridosilicates anions (e.g.$SiH_2R_3^-$ and $SiH_2OR_3^-$) have been prepared and characterized.[12,13] Such species have received attention because of their significance as model systems, intermediates or transition states in organosilicon reactions.[14,15]

So far, the SiH_5^- ion is the only hypervalent all-hydrido species known. It was identified as a product of the gas phase ion-molecule reaction by mass spectrometer.[16]

$$Et_3SiH_2^- + SiH_4 \rightarrow SiH_5^- + Et_3SiH \qquad \textit{Equation 5.1}$$

This ion subsequently served as a prototype for various theoretical investigations into the bonding properties and the stability of hypervalent compounds.[17-19] It was found that the SiH_5^- ion is stable with respect to loss of H^-, but unstable with respect to decomposition into SiH_3^- and H_2.[17-19]

In this study, a unique hypervalent all-hydrido complex, SiH_6^{2-} will be reported. This unique SiH_6^{2-} complex is a part of thermodynamically stable solids of A_2SiH_6 (A = K and Rb) which crystallize in the cubic K_2PtCl_6-type structure.[20] For sodium a different result was obtained.

5.3 Synthesis and Analysis of Hydrogen-dominant Materials Based on Silicon

The earlier described MA method (Chapter 2 and 4) employing ammonia borane as an internal hydrogen source was used. Two different reaction schemes were tested to find if the gigapascal MA hydrogenations of between silicon and alkali metal (A = Na, K, Rb) would lead to the formation of metal hydride.

Initially, a reaction between alkali metal hydride (A = Na, K or Rb) and elemental silicon was pursued.

$$2AH + Si + 2H_2 \rightarrow A_2SiH_6 \qquad \textit{Equation 5.2}$$

Stoichiometric mixtures of KH and Si (50 mg to 70 mg) were pressed into a pellet which was sandwiched between two ammonia borane pellets. Powder x-ray diffraction (PXRD) of samples after exposing them to high pressures above 4 GPa and temperatures between 450 to 650 ˚C revealed the formation of a cubic face-centered phase (a ~ 7.84 Å). However, the major part of the sample (~ 70 %) corresponded to unreacted KH and Si. Similar behavior was observed for RbH and Si synthesis. The new phase, later identified as K_2SiH_6, could be distinguished visually as a greenish-yellow colored speckles or stripes embedded in the gray matrix of starting material mixture. Despite numerous attempted reaction conditions (temperatures from 300 to 700 ˚C, pressures up to ~ 10 GPa, AH:Si ratio from 2:1 to 3:1, Si:H ratio from 1:10 to 1:20, dwelling time from minutes to hours), the yield of K_2SiH_6 did not significantly increase. Based on the experiments, the optimal temperature window was observed to be between 450 to 550 ˚C and minimum pressure needed was 4 GPa. The other parameters seemed to have little or no influence to yields.

As a next step, the decomposition reaction of alkali metal silicide was considered.

$$2ASi + 3H_2 \rightarrow A_2SiH_6 + Si \qquad \textit{Equation 5.3}$$

Although this reaction proceeded readily at pressures above 4 GPa, it came at the cost of significant amounts (up to ~20%) of a byproduct, ABH_4 (A = K, Rb). Additionally, the silicide precursor produces silicon as a decomposition product. However, the yields of A_2SiH_6 were slightly improved (up to ~50%). Efforts to synthesize Rb_2SiH_6 according to Equations (5.2) and (5.3) showed similar results to K_2SiH_6.

For Na–Si–H system, gigapascal hydrogenations from precursors NaH (Sigma Aldrich, 95%) and silicon powder (Sigma Aldrich, ~ 60 meshes, 99.999%) yielded no reaction at all. Therefore, the gigapascal hydrogenations (MA) were done according to Equation (5.3) using the silicon-to-hydrogen ratio of 1:10. The total mass of the sample was ~ 40 mg for NaSi hydrogenations. The synthesis pressure and temperature were varied from 3.5 GPa to 9.5 GPa and from 300 to 600 ºC, respectively. The main product(s) is not characterized but the results of these gigapascal hydrogenations will be presented later in this chapter.

The preparation of sample capsules and their recovery after synthesis was performed in an argon-filled glovebox. Products were analyzed using the powder X-ray diffraction (PXRD). The samples were ground, loaded into glass capillaries, and measured on a Bruker D8 Advanced diffractometer. The PXRD patterns were refined by TOPAS software[21,22] (for the samples where all phases could be identified). Refined parameters were background, phase fraction, unit cell, sample displacement, zero point, profile, strain, preferred orientation, atomic position, and absorption correction.[23] For patterns with unidentified phases, the lattice parameters were obtained from least-squares refinements.[24,25]

Spectroscopic studies were done to confirm that hydrogen atom (not able to refine position by PXRD) indeed was in the products. IR spectroscopy was carried out on a Bruker IFS 66v/s instrument. KBr pellets were prepared in a glovebox (~ 1 mg sample per 100 mg KBr) and transferred to the spectrometer in a closed container. Raman spectra were recorded on the capillary sealed samples that were also used for PXRD. A custom built system was employed using a frequency-double YAG laser at 532 nm as excitation source and a liquid nitrogen cooled CCD detector. Further details about analysis techniques can be found in Chapter 2.

Theoretical calculations were performed in the framework of the frozen core all-electron projected augmented wave (PAW) method,[26,27] as implemented in program VASP,[28,29] and the plane wave Abinit code[30] employing the GGA-PBE as the exchange correlations.[31] Si, H and F pseudopotentials were obtained from the fhi98PP package.[32] For K and Rb, the pseudopotentials according to Goedecker, Teter, and Hutter were used.[33-35] Appendix C has the computational details.

5.4. Structural Analysis of K_2SiH_6 and Rb_2SiH_6

The lattice parameter a of cubic A_2SiH_6 was refined to 7.8425(9) Å and 8.1572(4) Å for A = K and Rb, respectively.[20] Bragg intensities fit the K_2PtCl_6-type structure (*Fm*-3*m*) which is also adopted by fluorite analog A_2SiF_6. Accordingly, the structure of A_2SiH_6 corresponds to an anti-fluorite-type arrangement of $[SiH_6]^{2-}$ octahedral units and alkali metal (A) cations, which are coordinated by 12 H atoms (i.e. by four tetrahedrally arranged faces from four different octahedra). The Si and A-type atoms occupy the special positions (4a 0,0,0) and (8c $^1/_4$ $^1/_4$ $^1/_4$), respectively. Whereas, the H position 24e (x,0,0) represents the sole flexible structural parameter which cannot be reliably obtained from the refinement of PXRD patterns.

As discussed earlier, the hydrogenation of a mixture between 2KH and Si according to Equation (5.2) yielded ~ 35% K_2SiH_6. From the diffraction pattern, the majority of the sample was identified as unreacted precursors, KH and Si (Figure 5.1).

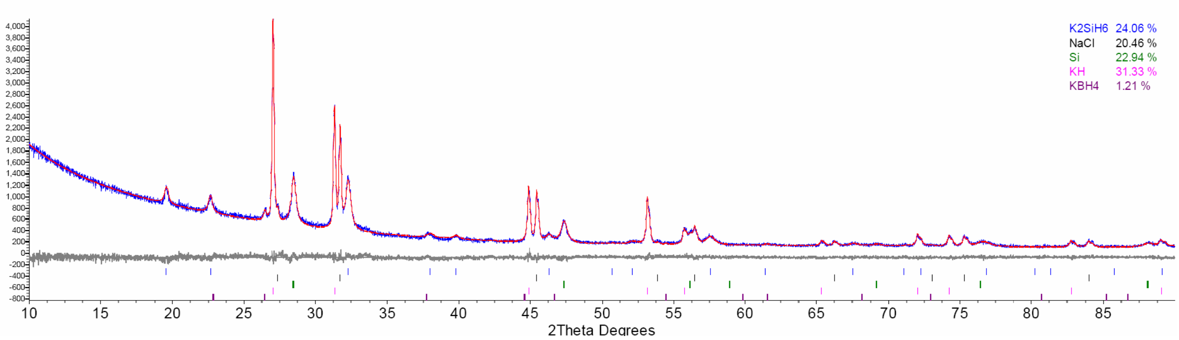

Figure 5.1. Rietveld fit to a PXRD pattern for a sample obtained from a reaction $2KH+Si+BH_3NH_3$ at 8.1 GPa and 400 ºC, a (K_2SiH_6) = 7.8425(5) Å, χ^2 =1.39, R_p = 4.06%, R_{wp} = 5.58%).[20]

Reactions according to Equation (5.3) employing KSi as a precursor improved the yield of K_2SiH_6 considerably (Figure 5.2). However, despite numerous attempts to achieve a complete reaction the maximum yield never exceeded 50%. The improved yield of K_2SiH_6 came at the cost of a significant amount of byproduct, KBH_4 (up to ~ 20%). The boron is obviously introduced from the decomposed hydrogen source, BH_3NH_3. KBH_4 is also present in hydrogenations done according to Equation (5.2), but in miniscule (< 2%) amounts (Figure 5.1).

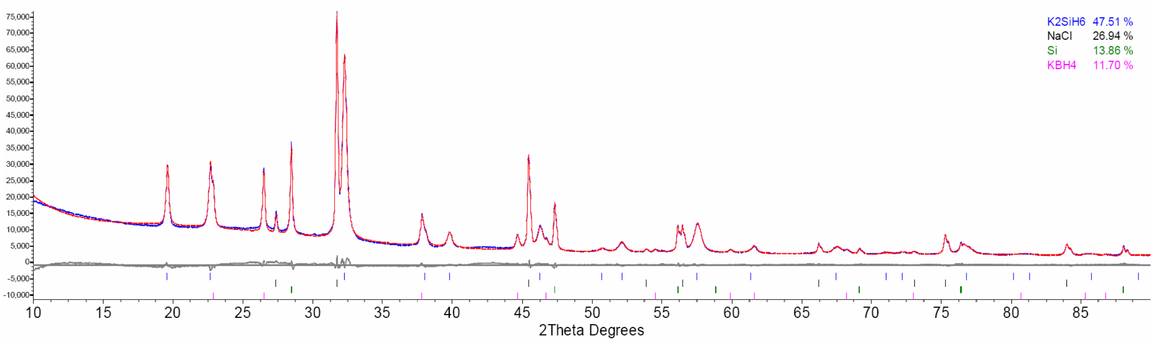

Figure 5.2. Rietveld fit to a PXRD pattern for a sample obtained from a reaction $2KSi + BH_3NH_3$ at 7.6 GPa and 450 ºC, a (K_2SiH_6) = 7.8425(9) Å, χ^2 = 3.96, R_p = 2.09%, R_{wp} = 2.78%.[20]

Hydrogenations of mixtures RbH and Si led to a similar results as for KH and Si. Apparently it is difficult to react elemental silicon under the applied conditions. Rb_2SiH_6 was the major phase in diffraction pattern when hydrogenating RbSi (Figure 5.3). The powder pattern reveals that apart from $RbBH_4$ and Si there are further (unidentified) products.

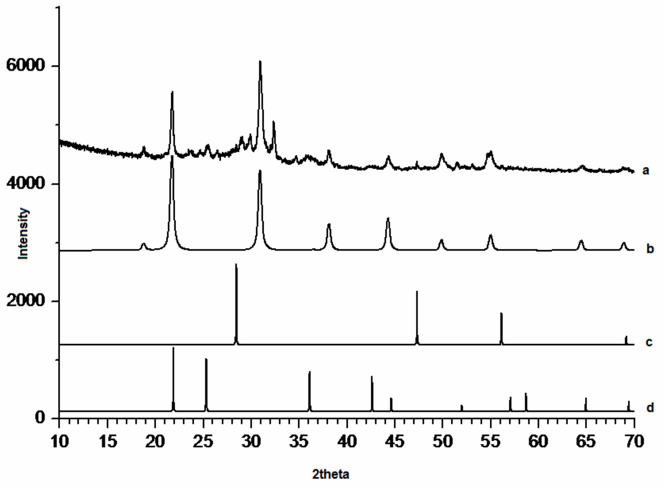

Figure 5.3. PXRD pattern for a sample obtained from a reaction $2RbSi+BH_3NH_3$ at 5.8 GPa and 450 ºC (a) is compared to a theoretical Rb_2SiH_6 (b). The Si (c) and a byproduct $RbBH_4$ (d) pattern.

First-principles calculations were employed to analyze electronic structure, chemical bonding and thermodynamic stability of K_2SiH_6. The computational optimization of the K_2SiH_6 structure yielded a lattice parameter of 7.852 Å (7.978 Å when more realistically considering the effect of zero-point energy, ZPE, to the equilibrium volume) which is in close agreement with the experimental value of 7.8425(9) Å. The H positional parameter was obtained as 0.2058 which resulted in a Si-H bond distance of 1.62 Å (not changed when ZPE corrected). This distance compares favorably to $R_3SiH_2^-$ where the two Si-H distances have been reported as 1.64 Å and 1.65 Å,[13,36] and to the axial Si-H distance in SiH_5^- in its computed equilibrium structure (1.61 - 1.64 Å).[16-19]

An octahedral ion SiH_6^{2-} will give a rise to six internal fundamental modes. The three Si-H stretching modes with symmetry A_{1g}, E_g and T_{1u} in which the first two stretching modes are Raman active whereas T_{1u} is IR active mode. In addition to Si-H stretching modes, the three Si-H bending modes with symmetry T_{2g}, T_{1u} and T_{2u}, which are Raman active, IR active and inactive, respectively, are observed. This agrees with the number of observed bands in spectroscopic studies (IR and Raman). Therefore, the bands of K_2SiH_6 that are observed at

1739, 1560 and 1343 cm^{-1} can be assigned as Si-H stretches, and those at 1133 and 1014 cm^{-1} are assigned to the Si-H bends (Figure 5.4). The unassigned band at 1367 cm^{-1} might be an impurity band or a result of Fermi resonance.[37]

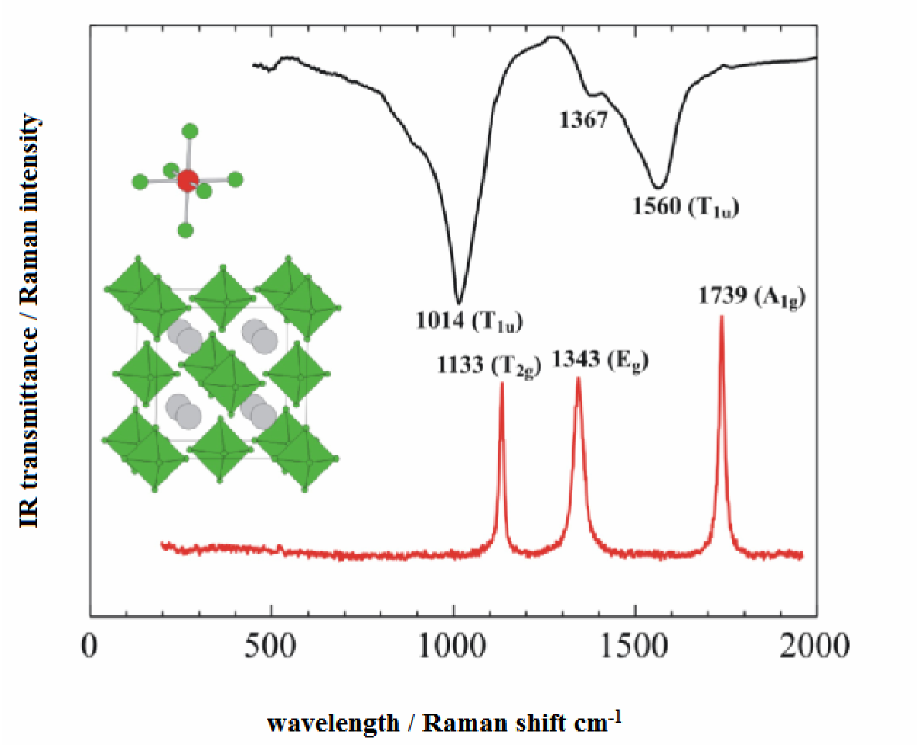

Figure 5.4. Raman (lower) and IR (upper) spectrum of K_2SiH_6.[20]

Similarly, the spectroscopic analysis of Rb_2SiH_6 was performed using both IR and Raman spectroscopy (Figure 5.5). IR bands are observed at 1508 and 997 cm^{-1} and Raman bands are located at 1742, 1318 and 1082 cm^{-1}. The bands at 1742, 1508 and 1318 cm^{-1} are assigned to the Si-H stretches and bands at 1082 and 997 cm^{-1} as Si-H bends. So far, the band at 1382 cm^{-1} is unassigned and may be result of an impurity or a Fermi resonance.[37]

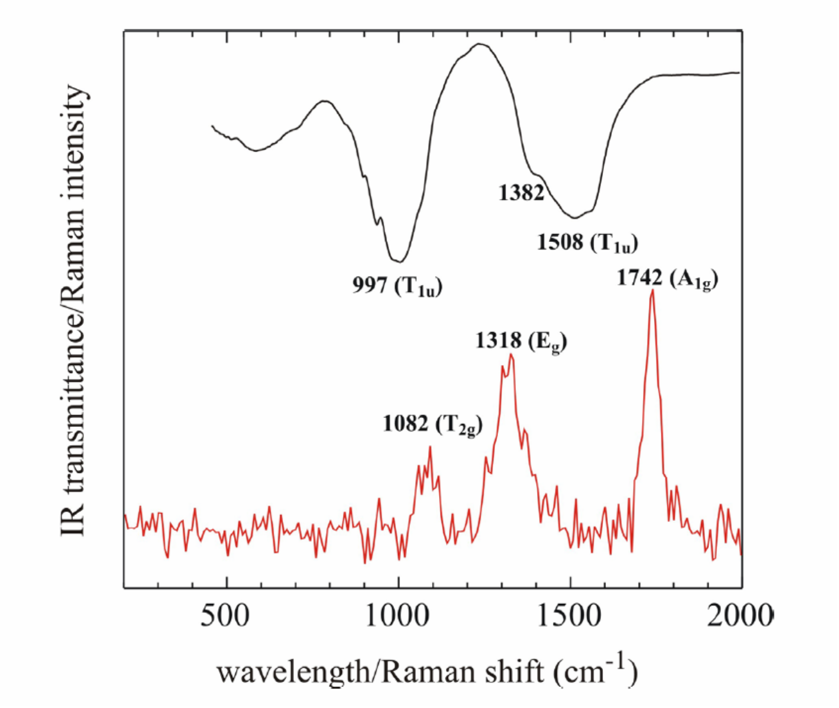

Figure 5.5. Raman and IR spectrum for Rb_2SiH_6.[20]

It is noted that the frequencies of the stretching modes appear considerably decreased in comparison with a normal-valent (2e2c) silane SiH_4 (2186 and 2189 cm^{-1}), while the bending modes are at slightly higher frequencies (SiH_4: 972 and 913 cm^{-1}).[38,39] On the other hand, for $Ph_3SiH_2^-$ the IR frequency of Si-H was observed at 1524 cm^{-1}, which would be in reasonable agreement with the finding for SiH_6^{2-}.[13] In $Ph_3SiH_2^-$ hydrogen has the axial (3e4c bonded) position in the trigonal bipyramidal ligand environment.[36] Table 5.1 shows the collected Si-H frequencies.

Table 5.1. Collection of Si-H stretching and bending frequencies (IR/Raman).[13, 36,38,39]

Si - H	K_2SiH_6	Rb_2SiH_6	SiH_4	$Ph_3SiH_2^-$
Streching	1739	1742	2186	
	1560	1508	2189	1524
	1343	1318		
Bending	1133	1082	972	
	1014	997	913	

First-principles calculations of phonons provided the possibility to confirm the assignment of experimentally determined vibrational modes, investigate the dynamical stability of compounds, and access thermodynamic functions.[40] In Figure 5.6, the calculated phonon dispersion relations for K_2SiH_6 and $RbSiH_6$ at the computed (theoretical) ZPE volume, are shown.

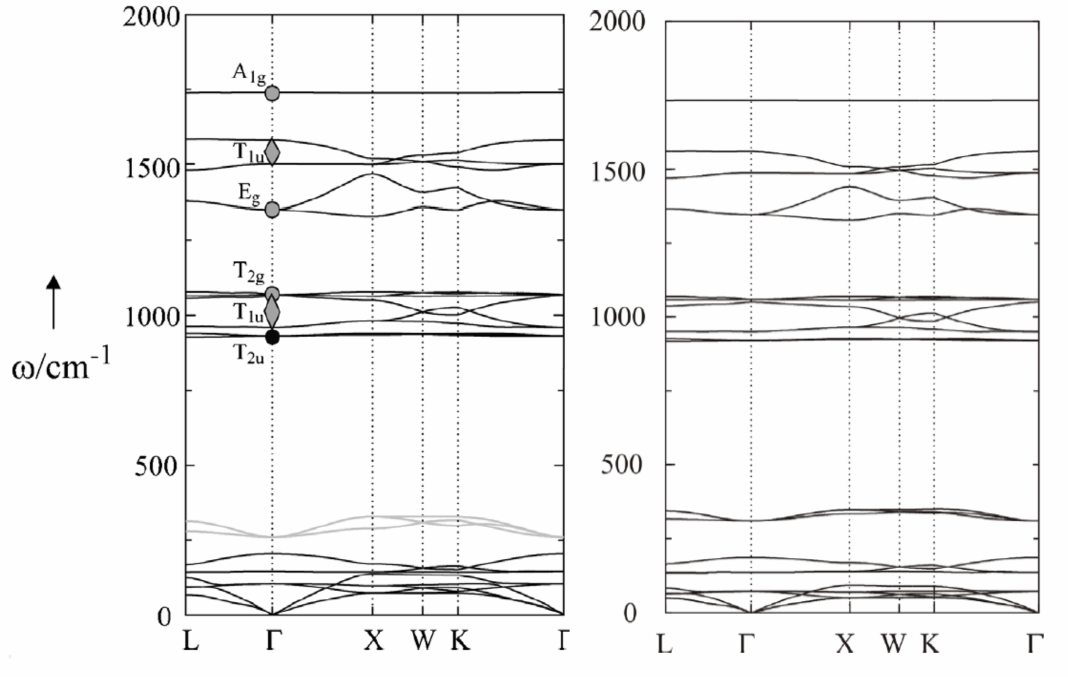

Figure 5.6 The calculated phonon dispersion relations for K_2SiH_6 (left) and Rb_2SiH_6 (right) at the computed ZPE volume.[20]

These dispersion curves (Figure 5.6) show the phonon frequencies along special directions in the Brillouin zone (BZ); k points describe the propagation direction and the modulation of displacements of a phonon. Inelastic neutron scattering allows the experimental determination of phonon dispersions, the situation at the zone center (Γ point) is accessible by optical spectroscopy (IR and Raman).

The mode with the highest frequencies has virtually no dispersion and corresponds to the Raman-active total symmetric stretch A_{1g} at Γ. The calculated frequency at Γ (Figure 5.6) is 1739 cm^{-1} which is in excellent agreement with the experimentally observed frequency (Fig. 5.4; 1739 cm^{-1}). The next modes show dispersion and relate to the IR active T_{1u} mode, which is split at Γ point (LO – TO splitting), and the Raman-active E_g mode. The T_{1u} components have the frequencies 1580 cm^{-1} (TO) and 1501 cm^{-1} (LO), and the E_g mode has frequency of 1352 cm^{-1}. These frequencies are in good agreement with experimental values of 1560 and 1343 cm^{-1}, respectively. Modes associated with bends are located around 1000 cm^{-1}, the Raman-active T_{2g} mode is calculated at 1069 cm^{-1}, the components of IR-active T_{1u} are at 1067 cm^{-1} (TO) and 959 cm^{-1} (LO), and the inactive T_{2u} mode is at 930 cm^{-1}. For the bending modes, the calculated frequencies seem underestimated by about 6 % compared to the experimental values. Similarly, the experimental and calculated Si-H stretching modes were in agreement in the case of Rb_2SiH_6.

The internal modes, arising from the SiH_6^{2-} entities, are clearly separated from the external (lattice) modes and appear below 500 cm^{-1}. Lowest in frequency are the acoustic and two optic translation modes T_{2g} and T_{1u} (K^+ vibrates against SiH_6^{2-}). The libration (or torsion) mode is dispersed around 300 cm^{-1}. Libration describes the rotation of octahedral units against each other and involves only hydrogen motion. The phonon dispersion of this mode is highlighted in Figure 5.6 (light gray). This mode is inactive in optical spectroscopy (T_{1g}) but may be involved in combination with the also inactive T_{2u} bend and thus give a rise to Fermi resonance,[38] which could explain the feature in the IR spectrum at 1367 cm^{-1}. It is likely that dynamic stability of hydridosilicates A_2SiH_6 requires a sufficient separation of SiH_6^{2-} octahedral in the structure.

The electronic band structure of K_2SiH_6 (Figure 5.7) is compared to the archetypical hypervalent system K_2SiF_6. The occupied bands for K_2SiH_6 mirror the molecular orbital levels of SiH_6^{2-}.

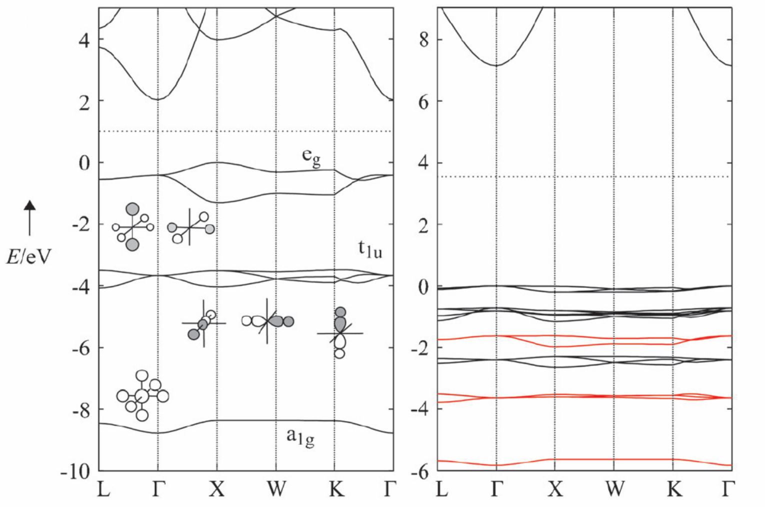

Figure 5.7. The electronic band structure of K_2SiH_6 (left) and K_2SiF_6 (right). Bands associated with hypervalent bonding in K_2SiF_6 are highlighted in red. The horizontal dotted line corresponds to the center of band gap.[20]

The highest lying e_g-type band which is nonbonding and primarily composed of H states, shows a significant dispersion (~ 1.5 eV). The calculated band gap has a size of about 2 eV and is indirect due to dispersion behavior of nonbonding e_g band (Figure 5.7). In contrast, because of the electronegative ligand, K_2SiF_2 (a = 8.3044 Å, $d_{Si\text{-}H}$ = 1.72 Å)[7] attains a wide band gap with a size of ~ 7 eV. The occupied bands are considerably less dispersed compared to K_2SiH_6. The nonbonding e_g band is embedded between bands that account for lone pair states, and because of altered nature of the highest occupied band, the band gap is direct (Figure 5.7).

The rather different nature of the hypervalent Si-H bond compared to Si-F is highlighted by their maximally localized Warner functions (MLWFs) as shown in Figure 5.8. Generally, the Wannier representation allows a real-space presentation of the electronic structure based on localized orbitals.[40] However, Wannier functions are constructed from extended Bloch states and are non-unique. Marzarari and Vanderbilt[41] developed a procedure to iteratively minimize the spread of the Wannier functions so that they are well localized around the centers, hence MLWFs.[40,41]

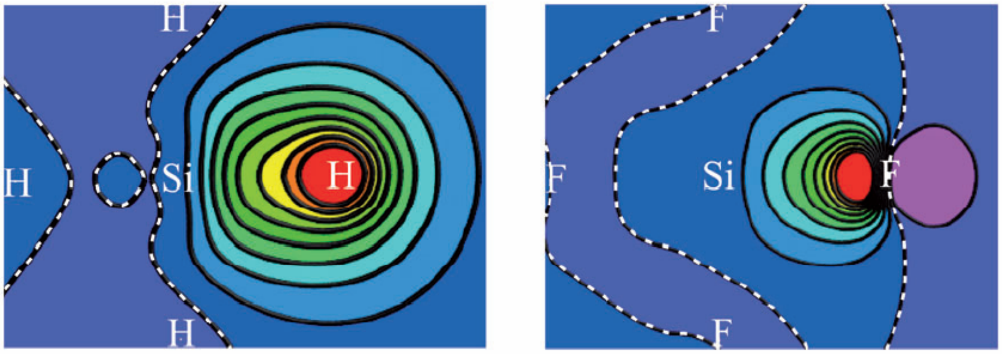

Figure 5.8. Contour maps of MLWFs associated with Si-H (left) and Si-F (right).[20]

The calculations for K_2SiH_6 yielded six spatially separated and equivalent MLWFs corresponding to the Si-H bond orbitals. In addition to Si-F bond orbitals, for K_2SiF_6 MLWFs corresponding to lone pairs around F are also obtained. Both Si-H and Si-F MLWFs are centered at the electronegative atom. However, their spread (the measure of localization) is rather different: 1.201 $Å^2$ for Si-H and 0.436 $Å^2$ for Si-F. This means that the Si-F MLWF is considerably more localized. As a matter of fact, the spread for the Si-F MLWF is essentially the same as for the lone pair MLWF (0.436 Å^2), which underlines the high polarity of the Si-F bond.

The different ionicities of K_2SiH_6 and K_2SiF_6 may be quantified using a Bader analysis which partitions the total electron density distribution in the unit cell into atomic regions, defined as surfaces through which the gradient of the density has zero flux.[42] By integrating the charged density within a region associated to a nucleus, the total charge on an atom can be uniquely estimated.[42] The results are compiled in Table 5.2.

Table 5.2. Atomic charges according to Bader analysis[42]

KH	K	+0.769	KF	K	+0.857
	H	-0.769		F	-0.857
K_2SiH_6	K	+0.809	K_2SiF_6	K	+0.912
	Si	+2.502		Si	+3.251
	H	-0.687		F	-0.846

In Table 5.2, KH and KF with the NaCl structure are included as reference systems. As expected, the charge transfer in KF (± 0.86) is considerably larger than in KH (± 0.76) manifesting the higher ionicity of the former. Interestingly, F in K_2SiF_6 attains a very similar charge to F in KF (-0.85) which in turn yields high positive chargers for Si and K (+3.25 and +0.91, respectively). This indicates that highly electronegative F determines the ionicity of K_2SiF_6. In contrast, the charge for H in K_2SiH_6 is considerably lower (-0.69) compared to charge for H in KH (-0.77), leading to less positive charges for Si and K (+2.502 and +0.809, respectively).

The high pressure needed to synthesize K_2SiH_6 raises a suspicion that the compound represents a metastable high-pressure phase. With the knowledge of the phonon density of states, the vibrational contributions to internal energy E (that includes ZPE), entropy S and Helmholtz free energy (F) can be computed.[43] In the quasiharmonic approximation phonons are harmonic but volume-dependent, and the equilibrium volume of a system is established by minimizing F_T. For reaction between AH and silicon (Equation 5.2), the energies can be calculated as follows.

$$\Delta G_T = G_T (A_2SiH_6) - 2G_T (AH) - G_T (Si) - 2 G_T (H_2) \qquad \textit{Equation 5.4}$$

$$G_T = H_T - TS_T \qquad \textit{Equation 5.5}$$

The temperature-dependent contribution of hydrogen molecule to the Gibbs free energy was approximated using values for H_T, S_T and H_0 from the thermodynamical tables.[44] Results for both K_2SiH_6 and Rb_2SiH_6 are shown in Figure 5.9 and free energy term is decomposed into ΔH and TΔS terms. The enthalpy difference ΔH_T is negative and its values slightly decrease with increasing temperature (more decrease for Rb analog). The formation reaction is exothermic.

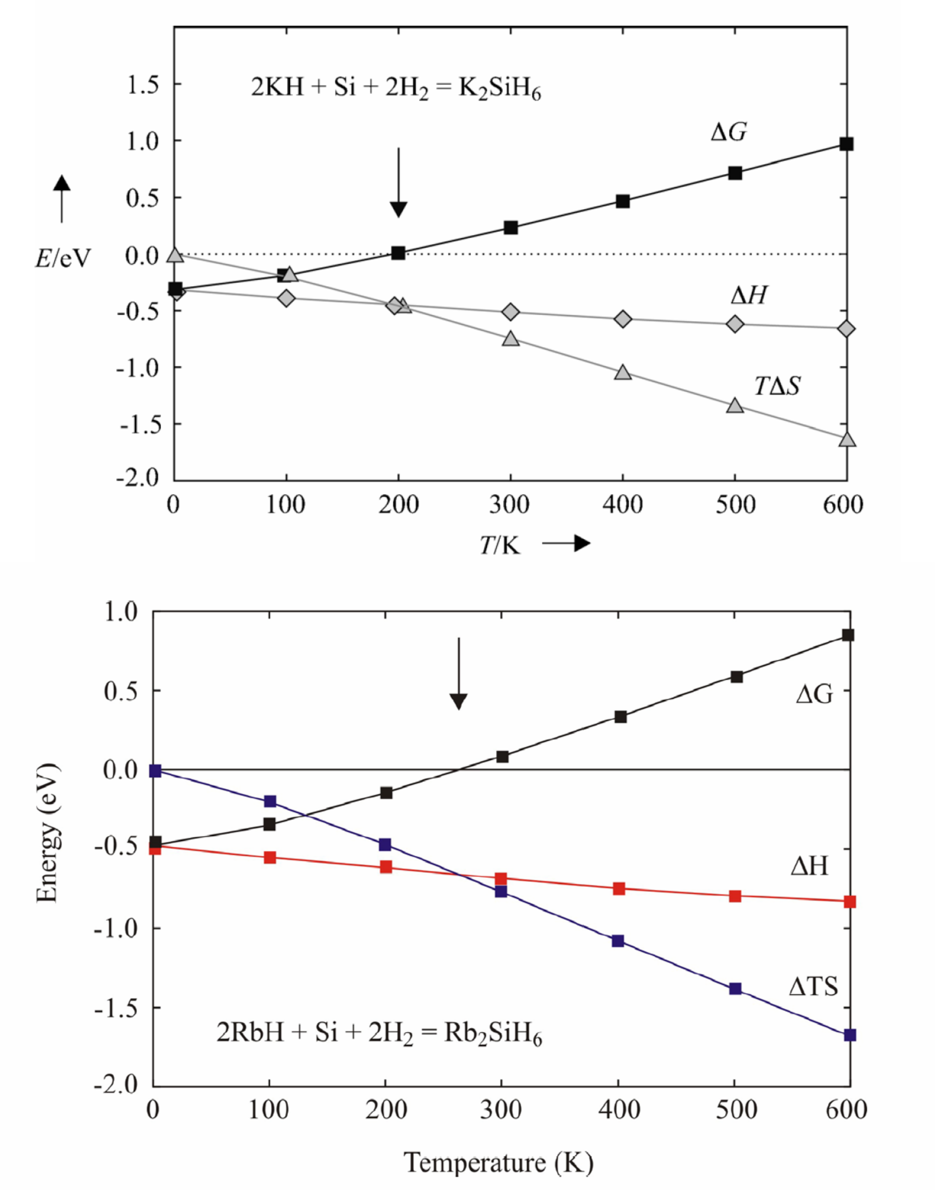

Figure 5.9 Temperature-dependent energies (Gibbs free energy ΔG, entropy TΔS, and enthalpy ΔH) between [2KH+ Si + $2H_2$] and K_2SiH_6 (upper) and Rb_2SiH_6 (lower). The decomposition temperature of A_2SiH_6 is denoted with an arrow.[20]

The $T\Delta S$ term is always negative and follows largely that of a hydrogen molecule, $T\Delta S_T(H_2)$.[44] At about 200 K and at 260 K, the $T\Delta S$ term equals to ΔH for K_2SiH_6 and for Rb_2SiH_6, respectively. At higher temperatures A_2SiH_6 (A = K or Rb) is unstable with respect to AH, Si and H_2 and will decompose if not prevented for kinetic reasons. The stability of A_2SiH_6 (A = K or Rb) increases as the cation size increases and the larger separation between SiH_6^{2-} is obtained. The significance of pressure for the synthesis of A_2SiH_6 is two-fold. Firstly, with pressure the decomposition temperature will shift to higher values, thus enabling the application of elevated temperature for synthesis. Secondly, at pressures above 1 GPa the activity of molecular hydrogen increases sharply, which favors hydridosilicate formation.[45-47]

The formation of K_2SiH_6 was theoretically investigated at pressures up to 10 GPa. For the crystalline materials, the pressure-dependent thermodynamic functions were obtained via the use of the third-order Birch-Murnaghan equation of state at each temperature of interest (400, 500 and 600 K). The equation of state of hydrogen was obtained via the combination of the high-pressure thermodynamic values of hydrogen available by Sugimoto, et al.,[48] and *ab initio* calculations of the internal energies (electronic and lattice). The Gibbs free energy of all materials was then calculated as

$$G = E_{elec} + \Delta E - TS + pV \quad \textit{Equation 5.6}$$

Appendix C has preceding equations and further details regarding the calculations. The Gibbs free energy up to 10 GPa is shown in Figure 5.10.

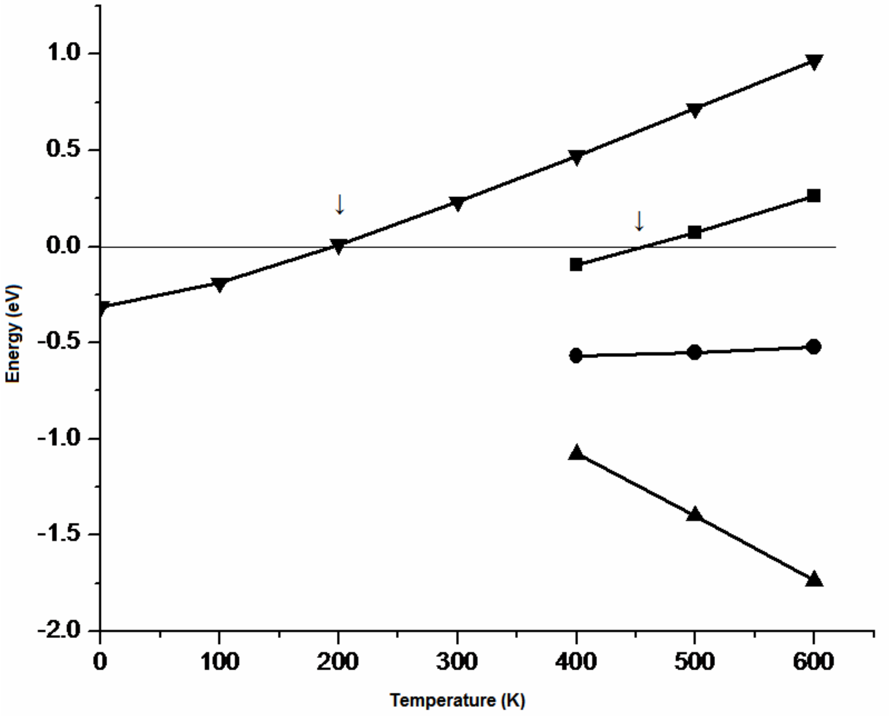

Figure 5.10 Gibbs free energy (G) at ambient (▼), 1 GPa (■), 5 GPa (•) and 10 GPa (▲) pressures. The decomposition temperature of K_2SiH_6 is denoted with an arrow.

Calculated Gibbs free energy values (Figure 5.10) indicate that even at moderate pressures (1 GPa), the formation of K_2SiH_6 is favorable up to a much higher temperature (~ 450 K) than at ambient pressure (~ 200 K). At greater pressures (> 1 GPa) the formation of K_2SiH_6 appears to be completely favorable.

In conclusion, it was shown that high-pressure synthesis affords elusive all-hydrido hypervalent species, namely octahedral complexes SiH_6^{2-} in the crystalline hydridosilicates A_2SiH_6 (A = K or Rb). The compounds seem weakly stable with respect to decomposition into AH, Si and H_2. Stability increases with increasing size of A, which is equivalent with the larger separation of SiH_6^{2-} entities. With H as a ligand, the hypervalent bond attains a peculiar, relatively weakly polar, character. As a consequence, occupied nonbonding molecular orbitals accompanying the hypervalent bond are high in energy which results in a small HOMO-LUMO (band) gap compared to traditional hypervalent systems with electronegative ligands. Compared to normal-valent silanes, the Si-H bond length in SiH_6^{2-} appears considerably enlarged, by about

0.15 Å. Accordingly, the Si-H stretching frequencies are drastically reduced, by about ~ 450 cm^{-1}, reflecting the weakness of a hypervalent Si-H bond.

5.5 Results of Na - Si – H System Gigapascal Hydrogenations

Hydrogenations of mixtures of NaH and Si at 7.6 GPa and 500 ºC did not yield any product. Therefore, gigapascal MA hydrogenations were continued using NaSi as a precursor, according to Equation (5.3). Reaction conditions were varied between 3.5 and 9.5 GPa, and 300 to 600 ºC. The silicon-to-hydrogen ratio was kept constant at 1:10 (Si:5H_2). The sodium analog of a cubic A_2SiH_6 (A = K or Rb) was not obtained from the gigapascal hydrogenations. This can be explained based on the calculated phonon dispersion curve for the hypothetical Na_2SiH_6 (Figure 5.11).

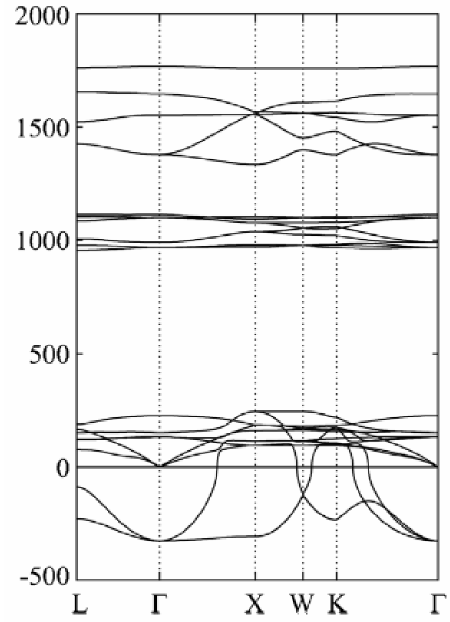

Figure 5.11. The calculated phonon dispersion curves for a hypothetical Na_2SiH_6.[20]

The phonon dispersion relation shows that libration determines the stability of hydrosilicates, A_2SiH_6. For hypothetical Na_2SiH_6 (Fig. 5.11), at the theoretical equilibrium volume, the phonon frequencies of libration modes are imaginary throughout most of the Brillouin zone. This indicates that this mode is unstable and thus Na_2SiH_6 with the K_2PtCl_6-type structure is not accessible. It seems that the dynamic stability of hydridosilicates A_2SiH_6 requires sufficient separation of anionic octahedral units. Therefore, with smaller alkali metals like Na, the structure is not accessible. The same trend is noticed for hypervalent silicon hexafluorides which are more stable as the cation size increases.[11]

Even though a K_2PtCl_6-type hexahydride was not found for Na, gigapascal hydrogenations resulted in $Na_xSi_yH_z$ hydride products. Figure 5.12 shows the powder XRD patterns of synthesis products obtained at 7 GPa and temperatures varying from 300 to 600 ºC. At 300 ºC the NaSi precursor is still recognizable in the diffraction pattern whereas at 600 ºC the powder pattern is dominated by silicon. Hydrogenation at 450 ºC, however, resulted in a diffraction pattern that clearly differs from the precursor with only a small amount of silicon present.

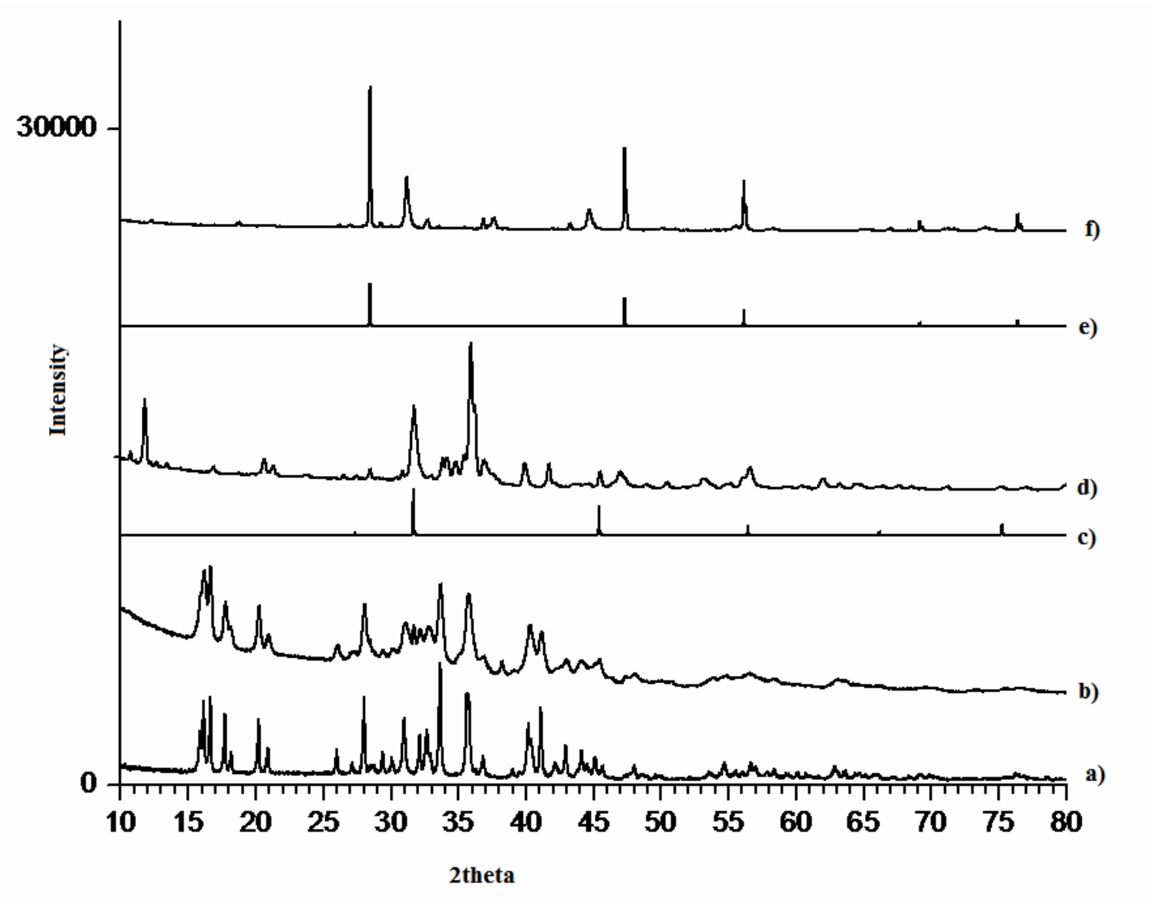

Figure 5.12. NaSi hydrogenations at constant pressure 7 GPa with varied temperature: 300 ºC (b), 450 ºC (d) and 600 ºC (f). The precursor material NaSi (a), silicon (e) is the decomposition product, and NaCl (c) is impurity from the capsule material.

Similarly, a series of hydrogenations at a constant temperature (450 ºC) was performed and pressure varied from 3.5 to 9.5 GPa (Figure 5.13). The pattern of the product from the hydrogenation at 3.5 GPa has some similarities with the precursor, but also additional peaks at low 2θ values appear. The origin of the peaks is not known. Raising pressure to 5.8 GPa is accompanied with additional changes. At 7 GPa the decomposition of the precursor into silicon is initiated and the pattern is completely different from the precursor. In that aspect, it is surprising that at 9.5 GPa the sample is not completely decomposed. At the highest pressure, also weak diffraction lines from $NaBH_4$ start to appear.

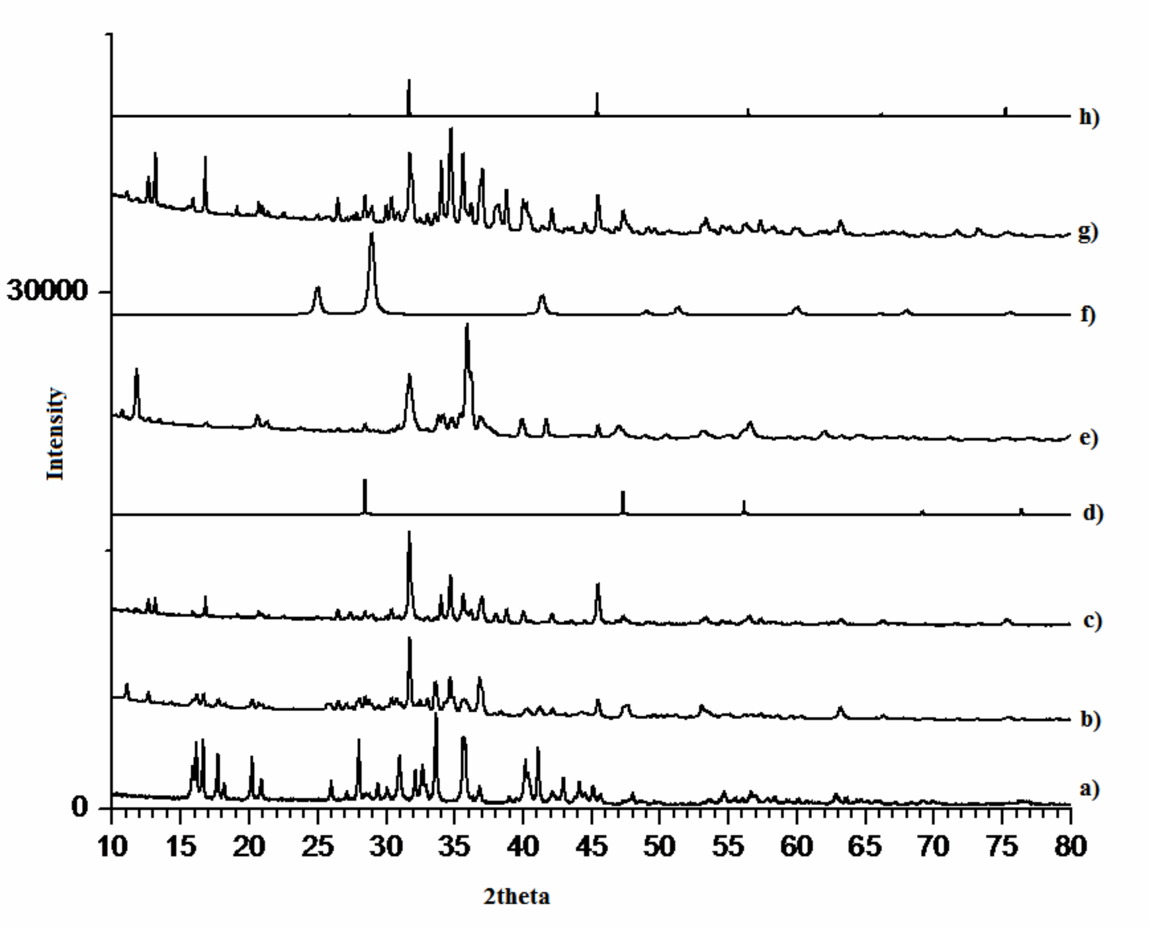

Figure 5.13. NaSi hydrogenations at constant temperature 450 ºC with varied pressures: at 3.5 GPa (b), 5.8 GPa (c), 7 GPa (e) and 9.5 GPa (g). The precursor material NaSi (a), silicon (d), $NaBH_4$ (f) and NaCl (h) patterns are also shown.

The experiments where pressure was varied at 450 ºC are very difficult to interpret. Most likely mixtures of various hydride and/or decomposition products were obtained. Based on the two experiment series (i.e. P and T variation), it was concluded that hydrogenation conditions close to 5.8 GPa and 450 ºC were the most promising for obtaining a single phase product $Na_xSi_yH_z$. These conditions lead to a reproducible product (Figure 5.14); however its characterization could not be achieved.

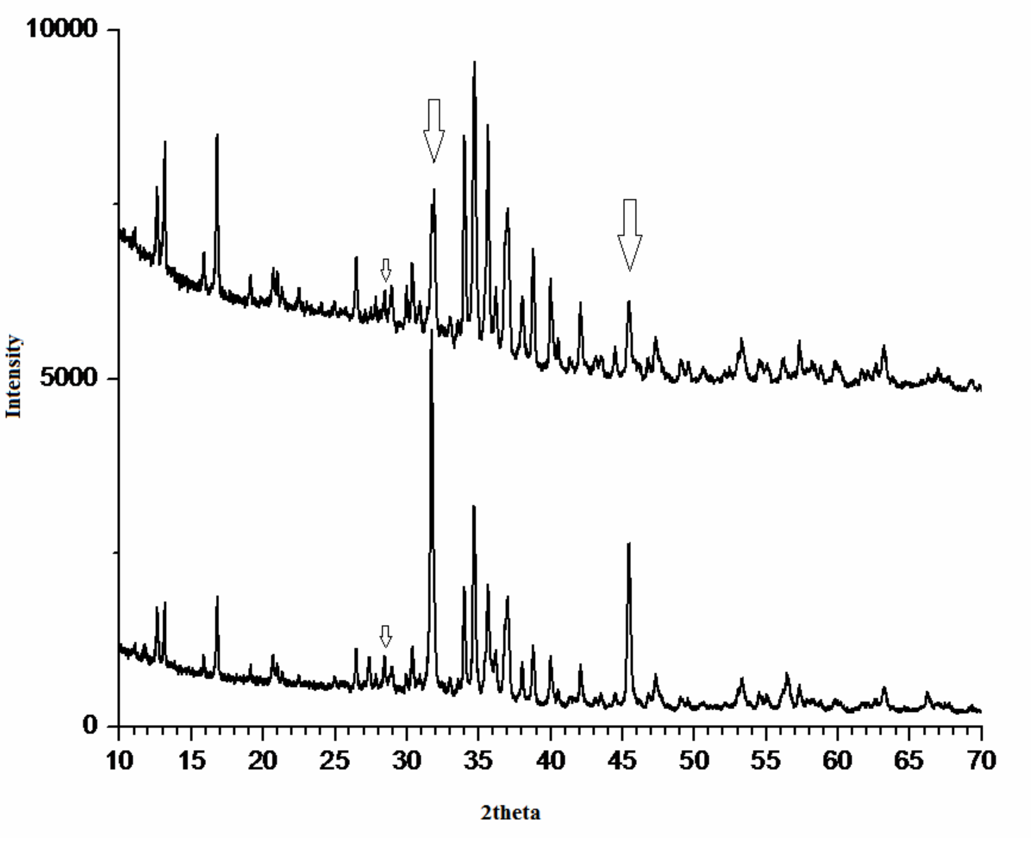

Figure 5.14. Result of two independent hydrogenations of NaSi at 5.8 GPa and 450 ºC. Large arrows indicate NaCl and small arrows Si.

One may speculate that the $Na_xSi_yH_z$ product obtained at 5.8 GPa and 450 ºC also consists of SiH_6^{2-} moieties. This is indicated by IR spectroscopy (not shown). However, such units do not occur separated (as in K_2PtCl_6-type A_2SiH_6) but may be condensed into chains of corner-connected octahedral SiH_6^{2-} units. This would allow for a composition $NaSiH_5$, and arrangements like this are known from silicon fluoride chemistry.

5.6 Hydrogen-dominant Materials Based on Boron

$LiBH_4$ is the only stable hydride in the Li-B-H system, and it is well studied.[49] It has a high volumetric and gravimetric density of hydrogen and has been of interest as a hydrogen storage material. However, hydrogen release occurs at high temperature and is irreversible. There has been attempts to improve the kinetics of $LiBH_4$ by doping to make it suitable for energy applications.[50]

It has been proposed that $LiBH_4$ would have high-pressure phases displaying more suitable properties (reversibility and improved kinetics) for energy applications.[51] These possible high pressure phases have initiated theoretical studies, and in recent years also diamond anvil cell (DAC) experiments of $LiBH_4$ have been performed.[51-53] DAC studies provide a way to probe the behavior of materials under extreme pressures. However, the DAC is not a tool for the synthesis of materials. The proposed high-pressure phases of $LiBH_4$[51-53], which were described earlier in this chapter, will be used as a starting point to analyze recovered products from LiH-B mixture gigapascal MA hydrogenations.

As early as 1974, five different $LiBH_4$ phases were observed by Pistorius[54] using piston-cylinder technique. The room temperature orthorhombic *Pnma* (Phase II) and high temperature tetragonal (Phase I) phases were characterized. Three high-pressure phases (Phases III, IV, and V) were observed but no structural refinements were done as the high-pressure phase transformations were studied using DTA. In 2002, Soulie, et al.,[55] confirmed that the room temperature phase crystallizes in an orthorhombic (*Pnma*) structure which was also confirmed by Hartman, et al.,[56] Lithium borohydride is different from the heavier alkali metal borohydrides which attain cubic structures at ambient conditions. In 2002, Soulie, et al.,[55] characterized the high-temperature (HT) phase of $LiBH_4$ as a hexagonal ($P6_3mc$) structure instead of the tetragonal structure found in the earlier studies by Pistorius[54]. Filinchuk, et al.,[53] and Hartman, et al.,[56] also later confirmed the hexagonal structure of HT-$LiBH_4$ phase.

Theoretical modeling of $LiBH_4$ appears to be difficult and contradictory results are reported. For example, the high-temperature hexagonal structure of $LiBH_4$ was predicted to be unstable and calculations suggest that the stable HT-phase of $LiBH_4$ would rather correspond to

Cc or *P*3 structure.[57,58] Considering the difficulties of characterizing the ambient pressure $LiBH_4$ phases (both at room and high temperature) and disagreements between experimental and theoretical results, it is not a surprise that the structure prediction and characterization of high-pressure phases is even more controversial.

In *in situ* high-pressure and high-temperature synchrotron studies done by Filnichuk, et al.,[51,53,59] the phase IV observed by Pistorius[54] was not found to exist. In these DAC studies, there were two characterized high-pressure phases, and neither of them was recoverable at ambient conditions. Phase III was characterized as an orthorhombic *Ama*2 structure, but has also been identified as $I4_1/acd$ structure, and Phase V has been identified as a cubic *Fm*3*m* structure.[51,53,59] The latter has been proposed to be recoverable and metastable at ambient conditions.[51,60] There also are theoretical studies predicting that *Cc* and $P2_1/c$ structures would be stable at high pressures (> 2 GPa).[61] In Figure 5.15, the P-T phase diagram of $LiBH_4$ based on recent experimental observations is shown.[51,53,59] These experimental findings will help to achieve more accurate theoretical predictions which so far have not been reliable for the $LiBH_4$ system.[52,57,58] The previous findings on $LiBH_4$ high-pressure phases will be used as a starting point to analyze experimental findings in this study.

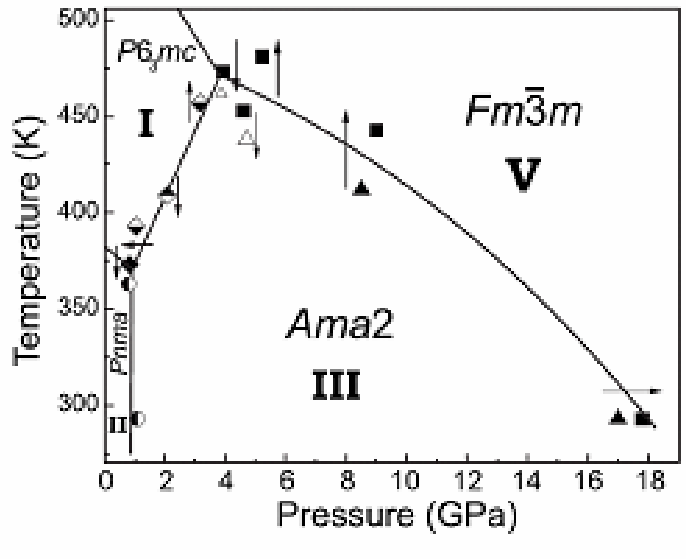

Figure 5.15. The $LiBH_4$ phase diagram according to ref (59).

In addition there have been theoretical calculations predicting that several polyanionic (not fully hydrogenated) phases of Li-B-H system may exist.[62] The energies and structures for Li_3BH_6 (*R*-3), and $LiBH_2$ and LiBH (both with *Pnma* space group symmetry) were calculated.[61] Orimo, et al.,[62] observed experimentally that monoclinic $Li_2B_{12}H_{12}$ forms as an intermediate decomposition product of $LiBH_4$.

The multi-anvil (MA) technique could provide a better way to target these phases and conserve them at ambient conditions for analysis purposes, pending that those phases are quenchable. It is already demonstrated in this study that high pressure can be beneficial when aiming to synthesize hydrogen-dominant materials. The results of gigapascal hydrogenation experiments of mixtures LiH and B will be presented later in this chapter.

5.7 Synthesis and Analysis of Li-B-H

MA hydrogenations (as introduced in Chapters 2 and 4) using ammonia borane as hydrogen source (Aldrich, powder, 99.9%) were carried out in a 6-8 Walker multi-anvil module. The starting materials were mixtures of LiH (Aldrich, powder, 95%) and B (Aldrich, powder, amporphous) with sample weights around 20 mg. The temperatures and pressures were varied from 400 to 700 ºC, and from 2 GPa to 8 GPa, respectively. The LiH-to-B ratio was varied from 1:1 to 2:1 whereas the ratio between boron and hydrogen was maintained at 1:10 ($B:H_2 = 1:5$). Sample handling was done inside argon-filled glovebox (air/moisture < 0.3 ppm).

Obtained products were analyzed using the x-ray diffraction and IR spectroscopy. The majority of samples had a brownish-red appearance indicating the presence of a large amount of unreacted amorphous boron. However, when applying pressure and temperature conditions of 6 GPa and 600 ºC, the samples had a light grey, almost white, color. The powder x-ray diffraction revealed a well crystalline product. The same conditions were repeated several times and the diffraction pattern could be reproduced. Figure 5.16 shows the diffraction pattern in comparison with that of monoclinic $Li_2B_{12}H_{12}$ and the patterns of reported high-pressure phases of $LiBH_4$.

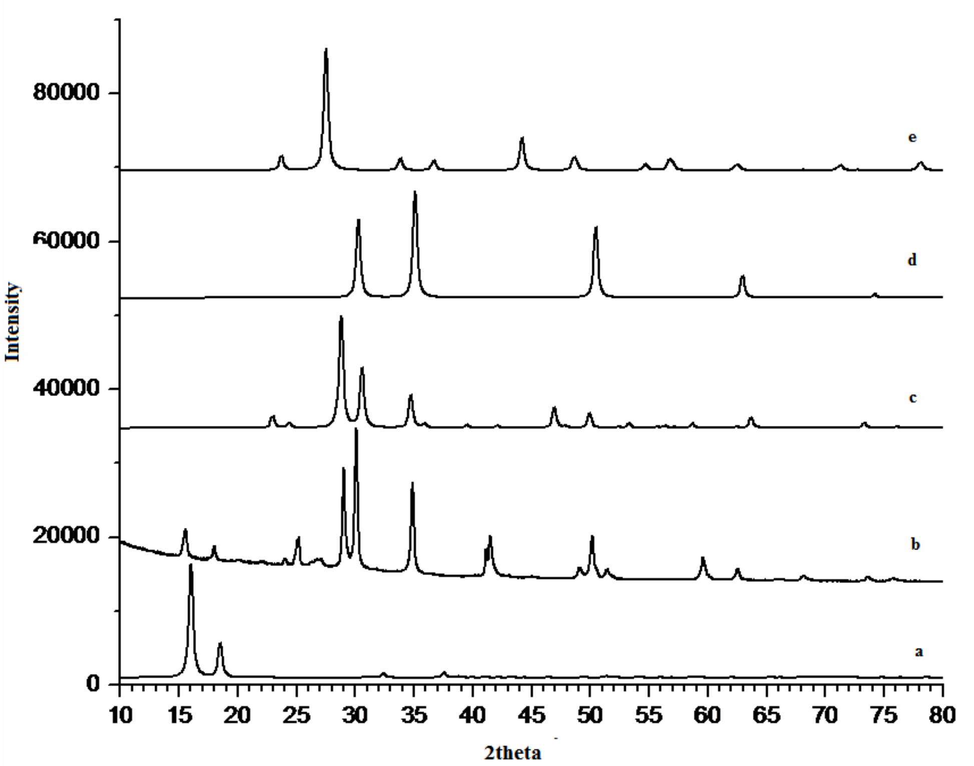

Figure 5.16. Powder XRD pattern of LiH-B hydrogenated at 6 GPa and 600 ºC (b) compared to $Li_2B_{12}H_{12}$ (a) and high-pressure phases observed in DAC studies.[59,62] High-pressure phase parameters for a tetragonal (c), a cubic (d) and an orthorhombic (e) cell are from gigapascal studies of $LiBH_4$.[52]

There was no resemblance between the obtained diffraction patterns and the known ambient-pressure (HT or room temperature) phases of $LiBH_4$. There is a resemblance with the patterns of $Li_2B_{12}H_{12}$ and tetragonal high-pressure phases (Figure 5.16a, c, d). However, these high-pressure phases are not supposed to be quenchable, and there is a significant mismatch in the Bragg positions of the $Li_2B_{12}H_{12}$ pattern and the gigapascal hydrogenated product (Bragg peaks below 2θ = 20º). It is proposed that the pattern Fig. 5.16b belongs to a new phase $LiBH_x$. The broad feature around 2θ ~ 26º may be attributed to a LiB alloy impurity.

The presence of B-H bonds in $LiBH_x$ was confirmed with optical spectroscopy. The IR spectrum is shown in Figure 5.17.

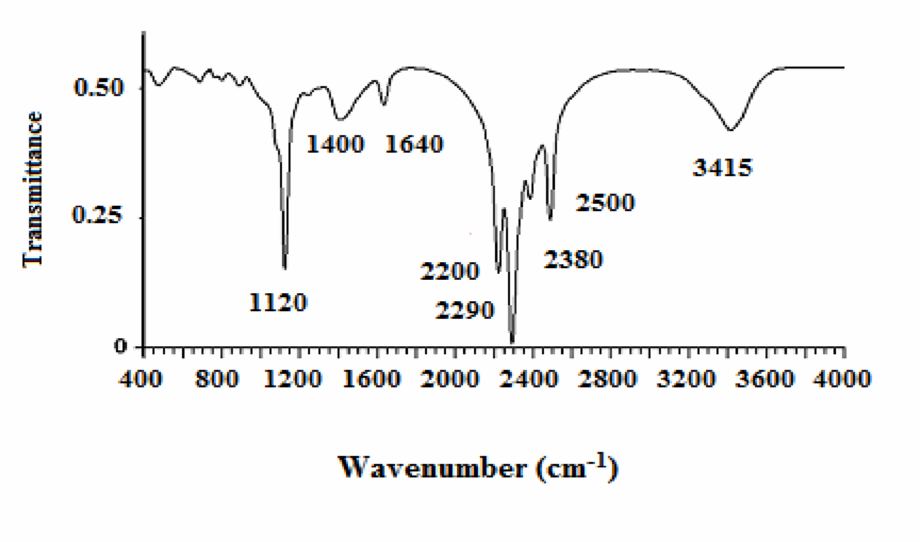

Figure 5.17. The IR spectrum of hydrogenation at 6 GPa and 600 ºC from LiH and B precursors.

Based on the IR spectrum, it can be confirmed that synthesis indeed produced a hydrogenated product as the B-H stretching mode region is between 2500 cm^{-1} to 2000 cm^{-1} and that region has strong spectral lines. The mode at 1120 cm^{-1} coincides well with a B-H bending mode. The sample embedded in KBr pellet was prepared in air and moisture-free conditions, and protected during the transportation to the spectrometer. However, the wide region around 3400 cm^{-1} shows the typical O-H stretching modes and low intensity peak at 1640 cm^{-1} further confirms the O-H contamination of the sample. This is not surprising in respect to an existing study by Yamawaki, et al.,[63] who observed that exposure of $LiBH_4$ to 5% humidity at room temperature leads to a ready formation of hydrated $LiBH_4 \cdot H_2O$. The short period of time it takes to remove the sample from a protected container and insert it into the spectrometer is obviously enough for OH contamination. This hydrate forming behavior hinders the interpretation of the IR spectrum and analysis should be taken very cautiously.

Completely air and moisture-free spectroscopy is possible with Raman spectroscopy because samples can be sealed into capillaries inside the Ar-filled glovebox (Figure 5.18).

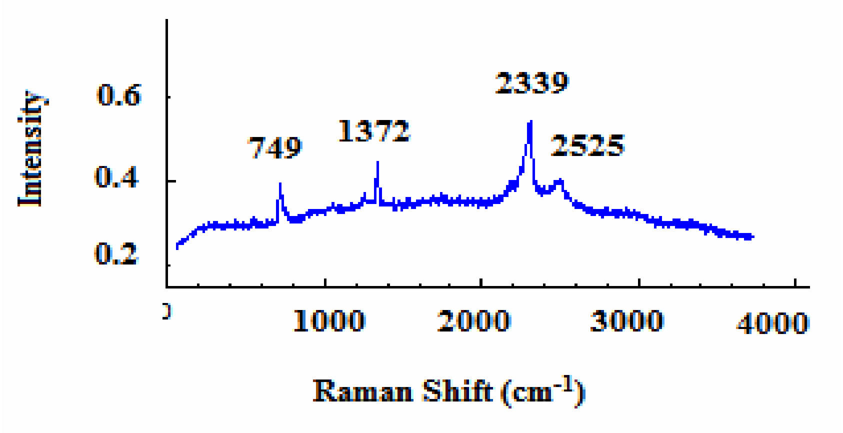

Figure 5.18. The Raman spectrum of hydrogenation at 6 GPa and 600 ºC from the LiH and B precursors.

The Raman spectroscopy revealed a spectral line at 1372 cm^{-1} which can be assigned to the B-H bending modes and the spectral lines at 2339 cm^{-1} and 2525 cm^{-1} to the B-H stretching modes. The mode at 749 cm^{-1} may relate to libration, but this is not yet clear. The analysis of the spectroscopic studies is hindered because the IR corresponded to that of an OH contaminated sample and may not be relied on to support the Raman spectrum.

5.8 Conclusions

Gigapascal MA hydrogenations were successfully performed to obtain K_2SiH_6 and Rb_2SiH_6 which crystallize in the cubic K_2PtCl_6-type structure with unit cell dimensions of 7.8425(5) Å and 8.1572(9) Å, respectively.[20] The formation of K_2SiH_6 proceeded at pressures above 8 GPa and at temperatures between 400 and 450 ºC, whereas Rb_2SiH_6 was obtained at 6 GPa and 450 ºC. It was not possible to prepare Na_2SiH_6 with the K_2PtCl_6-type structure which can be explained by the dynamic instability of such a system. Phonon dispersion calculations show that librational modes are imaginary throughout most of the Brillouin zone.[20]

The crystalline hexahydrides A_2SiH_6 (A = K, Rb) display unique hypervalent SiH_6^{2-} hydrido complexes, and the hypervalent bonding nature was confirmed by IR and Raman spectroscopy. Compared to normal-valent (2e2c) silane, the Si-H stretching frequencies of hypervalent bonds are drastically reduced, by about 450 cm^{-1}. This is also reflected in the enlarged Si-H bond legth (0.15 Å) in SiH_6^{2-}.

The synthesis of silicon hexahydrides also revealed that the internal hydrogen source ammonia borane was not as inert as previously thought. It was discovered that boron from decomposed source reacted with the sample material. This competing reaction between the desired product and ABH_4 (A = K, Rb) was preventing a complete reaction. However, the hexasilicide products were highly crystalline making the refinement of power x-ray diffraction patterns possible.

Finally, high-pressure hydrogenations of mixtures of LiH and B were carried out. At 6 GPa and 600 ºC, a well crystalline phase is obtained, and spectroscopic analysis confirmed the presence of B-H bonds in the sample. Most likely they are part of tetrahedral entities BH_4^-. The product is very air sensitive which makes IR spectroscopy challenging. Pre-existing DAC studies of $LiBH_4$[51-53], which were performed at pressures above 18 GPa[51] and are not recoverable phases, were used as a reference point in analyzing our recovered high-pressure phase but the structure remains yet to be characterized.

5.9 References

1. Zintl, E.; Woltersdorf, G., *Z. Angew. Phys. Chem*. **1935**, 41, 876

2. Kauzlarich, S.M., Ed., *Chemistry, Structure, and Bonding of Zintl Phases and Ions,* VCH: New York, **1996**

3. Ashcroft, N.W., *Phys. Rev. Lett*. **1968**, 21, 1748

4. Cudazzo, P.; Profeta, G.; Sanna, A.; Floris, A.; Continenza, A.; Massida, S., *Phys. Rev. Lett*. **2008**, 100, 257001

5. Eremets, M.I.; Trojan, I.A.; Medvedev, S.A.; Tse, J.S.; Yao, Y., *Science* **2008**, 319, 1506

6. Martinez-Canales, M.; Oganov, A.R.; Ma, Y.; Yan, Y.; Lyakhov, A.O.; Bergara, A., *Phys. Rev. Lett*. **2009**, 102, 087005

7. Loehlin, J.H., *Acta Cryst. C* **1984**, 40, 570

8. Hach, R.J.; Rundle, R.E., *J. Am. Chem. Soc.* **1951**, 73, 7940

9. McGrady, G.S.; Steed, J.W.; Ed. King, R.B.; *Encyclopedia of Inorganic Chemistry* **2005***,* 2, 1938

10. Musher, J.I., *Angew. Chem. Int. Ed*. **1969**, 8, 54

11. Noury, S.; Silvi, B*., Inorg. Chem*. **2002**, 41, 2164

12. Corriu, R.; Guerin, C.; Henner, B.; Wang, Q., *Inorg. Chem. Acta* **1992**, 198-200, 705

13. Prince, P.D.; Bearpark, M.J.; McGrady, G.S.; Steed, J.W., *Dalton Trans*. **2008**, 271

14. Chuit, C.; Corriu, R.J.P.; Reye, C.; Young, J.C., *Chem. Rev*. **1993**, 93, 1371

15. Bento, A.P.; Bickelhaupt, F.M., *J. Org. Chem*. **2007**, 72, 2201

16. Taketsugu, T.; Gordon, M.S., *J. Phys. Chem*. **1995**, 99, 14597

17. Moc, J., J. *Mol. Struct*. **1999**, 461-462, 249

18. Couzijin, E.P.A.; Ehlers, A.W.; Schakel, M.; Lammertsma, K., *J. Am. Chem. Soc.* **2006**, 128, 12364

19. Pierrefixe, S.C.A.H.; Guerra, C.F.; Bickelhaupt, F.M., *Chem. Eur. J*. **2008**, 14, 819

20. Puhakainen, K.; Benson, D.; Nylén, J.; Konar, S. ; Stoyanov, E.; Leinenweber, K.; Häussermann, U., *Angew. Chem. Int. Ed.* **2012**, 51, 3156

21. Bruker, A.X.S., *TOPAS V4: General Profile and Structure Analysis Software for Powder Diffraction Data*, User's Manual, Karlsruhe, Germany, **2008**

22. Sabine, T.M.; Hunter, B.A.; Sabine, W.R.; Ball, C.J., *J. Appl. Crystallogr*. **1998**, 31, 47

23. Eriksson, L., PFILM, program for manipulation of powder diffractonmeter data, **2004**

24. Werner, P.-E., *Ark. Kemi* **1969**, 31, 513

25. Blöch, P.E., *Phys. Rev. B* **1994**, 50, 17953

26. Kresse, G.; Joubert, J., *Phys. Rev. B* **1999**, 59, 1758

27. Kresse, G.; Hafner, J., *Phys. Rev. B* **1993**, 48, 13115

28. Kresse, G.; Furthmüller, J., *Comput. Mater. Sci*. **1996**, 6, 15

29. Gonze, X.; Amadond, B.; Anglade, P.M.; Beuken, J.M; Bottin, F.; Bolanger, P.; Bruneval, F.; Caliste, D.; Carcas, R.; Côté, M.; Deutsch, T.; Genovese, L.; Ghosen, Ph.; Giantomassi, M.; Goedecker, S.; hamann, D.R.; Hermet, P.; Jollet, F.; Jomard, G.; Leroux, S.; Mancini, M.; Mazevet, S.; Oliveira, M.J.T.; Onida, G.; Pouillon, Y.; Rangel, T.; Rgnanese, G.M.; Sangalli, D.; Shaltaf, R.; Torrent, M.J.; Verstraete, M.J.; Zerah, G.; Zwanziger, J.W., *Comput. Phys. Commun*. **2009**, 180, 2582

30. Perdew, J.P.; Burke, K.; Ernzerhof, M., *Phys. Rev. Lett*. **1996**, 77, 3865

31. Fuchs, M.; Sheffler, M., *Comput. Phys. Commun*. **1999**, 119, 67

32. Goedecker, S.; Teter, M.; Hutter, J*., Phys. Rev. B* **1996**, 58, 1703

33. Hartwigsen, C.; Goedecker, S.; Hutter, J*., Phys. Rev*. B **1998**, 58, 3641

34. Krack, M., *Theor. Chem. Acc*. **2005**, 114, 145

35. Bearprk, M.J.; McGrady, G.S.; Prince, P.D.; Steed, J.W*., J. Am. Chem. Soc.* **2001**, 123, 7736

36. Parker, S.F., *Coord. Chem. Rev*. **2010**, 254, 215

37. Ohno, K.; Matsuura, H.; Endo, Y.; Hirota, E., *J. Mol. Spectrosc*. **1985** 111, 73

38. Allen, W.D.; Schaefer III, H.F., *Chem. Phys*. **1986**, 108, 2430274

39. Gonze, X.; Lee, C., *Phys. Rev. B* **1997**, 55, 10355

40. Wannier, G.H., *Phys. Rev*. **1937**, 52, 191

41. Marzari, N.; Vanderbilt, D*., Phys. Rev. B* **1997**, 56, 12847

42. Bader, R.F.W., *Atoms in Molecules A Quantum Theory*, Oxford University Press, Oxford, **1990**, pp. 1-52

43. Ke, X.; Tanaka, I., *Phys. Rev. B* **2005**, 71, 024117

44. Chase Jr., M.W.; Davies, C.A.; Downey Jr., J.R.; Frurip, D.J.; McDonald, R.A.; Syverud, A.N.; *NIST-JANAF Thermochemical Tables*, National Institute of Standards and Technology, Gaithersburg, **1985**

45. Hemmes, H.; Driessen, A.; Griessen, R.J., *Phys. C* **1986**, 19, 3571

46. Driessen, A.; Sänger, P.; Hemmes, H.; Griessen, R.J., *J. Phys. Cond. Matter* **1990**, 2, 9797

47. Fukai, Y., *J. Alloys Compd*. **2005**, 405-405, 7

48. Sugimoto, H.; Fukai, Y., *Acta Metall. Mater.* **1992**, 9, 2327

49. Li, C.; Peng, P.; Zow, D.W.; Wanl, L., *Int. J. Hydrogen Energy* **2001**, 36, 14512

50. Liu, D.M.; Huang, W.J.; Si, T.Z.; Zhang, Q.A., *J. Alloys Compd*. **2013**, 551, 8

51. Filinchuk, Y.; Chernyshov, D.; Nevidomskyy, A.; Dmitriev, V., *Angew. Chem. Int. Ed.* **2009**, 47, 529

52. Yao, Y.; Klug, D.D., *Phys. Rev. B* **2012**, 86, 064107

53. Filinchuk, Y.; Chernyshov, D.; Cerny, R., *J. Phys. Chem. C* **2008**, 112, 10579

54. Pistorius C.W.F.T., *Z. Phys. Chem., Neue Folge* **1974**, 88, 253

55. Soulié, J.-Ph.; Renaudin, G.; Cerny, R.; Yvon, K., *J. Alloys Compd.* **2002**, 346, 200

56. Hartman, M.R.; Rush, J.J.; Udovic, T.J.; Bowman, R.C.; Hwang, S.J., *J. Solid State Chem*. **2007**, 180, 129

57. Lodziana, Z.; Vegge, T., *Phys. Rev. Lett.* **2004**, 93, 145501

58. Zarkevich, N.A.; Johnson, D.D., *Phys. Rev. Lett*. **2008**, 100, 040602

59. Dimitriev, V.; Filinchuk, Y.; Chernyshov, D.; Talyzin, A.V.; Dzwilewski, A.; Andersson, O.; Sundqvist, B., *Phys. Rev. B* **2008**, 77, 174112

60. Kang, J.K.; Kim, S.Y.; Han, Y.S.; Muller, R.P.; Dooddard, W.A., *Appl. Phys. Lett.* **2005**, 87, 111904

61. Frankcombe, T.J.; Kroes, G.-J.; Züttel, A., *Chem. Phys. Lett.* **2005**, 405, 73

62. Orimo, S.-I.; Nakamori, Y.; Ohba, N. ; Miwa, K.; Aoki, M.; Towata, S.; Züttel. A., *Appl. Phys. Lett.* **2006**, 89, 021920

63. Yamawaki, H.; Fujisha, H.; Gotoh, Y.; Nagano, S., *J. Alloys Compd.* **2012**, 514, 111

CHAPTER 6

SUMMARY

6.1 Summary

In the past decades, the study of metal hydrides has been focused on finding new hydrogen storage materials.[1,2] In addition to being attractive as hydrogen storage materials, metal hydrides offer other interesting properties. Indeed, hydrogen-induced structural changes in materials can lead to a wide variety of properties and applications.[3-8] An interesting class of metal hydrides are so-called hydrogen-dominant materials which may have high-temperature superconducting properties.[9-11]

Hydrogenous Zintl phases, which are mixed s and p-block metal/semimetal hydrides, have been intensively studied since mid-90's.[6-8] These systems are not viable hydrogen storage materials due to low hydrogen content, but are interesting for their hydrogen-induced structure and property changes.[12,13] In this study, its shown that hydrogenations of Li_3Al_2 lead to an oxidative decomposition into LiAl and LiH even at very low H_2 pressures (< 3 MPa) and mild temperatures (< 200 ºC). The oxidative decomposition competes with the formation of hydrogenous Zintl phases. A similar behavior was observed for Li_9Al_4, Li_2Al, Ca_3Ga_5 and Li_2Ga. It is remarkable that oxidative decompositions occur at very low pressures and temperatures, and even after short reaction times (15 min).

During the preparation of Li-Al Zintl phases used as precursors for hydrogenation studies a new phase $Li_{2-x}Al_{1+x}$ was discovered.[14] Based on the single crystal x-ray diffraction refinement, $Li_{2-x}Al_{1+x}$ crystallizes in an orthorhombic structure with the lattice parameters a = 4.6579 (16) Å, b = 9.767(4) Å and c = 4.4901(16) Å. This new phase displays a narrow homogeneity range, $Li_{1.92}Al_{1.08}$. Thermal studies using differential scanning calorimetry (DSC) were done to accurately detect its peritectic decomposition temperature (274 ºC).

Gigapascal hydrogenations employing multi-anvil (MA) technique were thought to be a viable way to generally access hydrogen-dominant materials because of the drastically increased hydrogen activity above 1 GPa.[15,16] As internal hydrogen source ammonia borane (BH_3NH_3), which has a high hydrogen content and releases irreversibly hydrogen at low temperature, was employed.[17]

As a first step, gigapascal MA hydrogenations were attempted to find if the missing lithium analog of the existing series A_2PtH_6 (A = Na to Cs) can be obtained. The existing platinum hexahydrides from Na to Cs were synthesized using a special autoclave, in which hydrogen gas pressures of up to 0.5 GPa can be achieved.[18-20] Na_2PtH_6 was synthesized in order to optimize the MA synthesis conditions for the search of Li_2PtH_6. Na_2PtH_6 was obtained at 5 GPa pressure and at 500 ºC. These conditions were used as a starting point in search of the lithium analog. Li_2PtH_6 was synthesized at pressures above 8 GPa and temperatures between 450 ºC and 500 ºC.[21] The structure of Li_2PtH_6 is analogous to the heavier homologues of A_2PtH_6 (A = alkali metal from Na to Cs) series which crystallize in the cubic K_2PtCl_6-type structure. Using the powder x-ray diffraction, the cell edge length was determined to be 6.7681(3) Å.[21] Attempts to synthesize the deuterized analog of Li_2PtH_6 resulted in $Li_2PtH_{1.5}D_{4.5}$ with heteroleptic complexes because of the insufficient deuterization of the hydrogen source. First-principles calculations were applied to determine the H atom position by optimizing the K_2PtCl_6 structure type for Li_2PtH_6. As a result, the hydrogen atom parameter x (24e x, 0, 0) was found to be 0.246. Li_2PtH_6 attains very peculiar structure compared to its heavier homologues. In Li_2PtH_6 the bond lengths within and between the octahedral units are close to equal whereas in the heavier analogs PtH_6^{2-} units are distinctly separated. Thus, the Li_2PtH_6 may be considered as a defective perovskite structure where half of the octahedrally arranged atoms (cations) are missing.[21]

Subsequent application of gigapascal MA hydrogenations to main group metal-silicon system led to the discovery of hypervalent silicon hexahydrides for alkali metals K and Rb. As Li_2PtH_6, also K_2SiH_6 and Rb_2SiH_6 crystallize in the cubic K_2PtCl_6-type structure. The unit cell parameter was determined as 7.8425(9) and 8.1572(4) Å for K_2SiH_6 and Rb_2SiH_6, respectively.[23] Hydrogenations were performed using two different reaction schemes starting from alkali metal hydride (AH, A = K, Rb) and silicon powder, and using the alkali metal silicide (ASi, A = K, Si) as a precursor. The former scheme did only produce a very low yield of product whereas the latter one resulted in higher yields but with the cost of a byproduct, ABH_4 (A = K, Rb). The boron is obviously originating from hydrogen source (BH_3NH_3). The hypervalent bonding in SiH_6^{2-} entities become very clear from the spectroscopic studies. Compared to normal-valent silanes (SiH_4)[24], the Si-H stretching frequencies in SiH_6^{2-} are about 450 cm^{-1} lower, and the Si-H bond legth is enlargened by about 0.15 Å. The sodium analog of a silicon hexahydride with K_2PtCl_6-type structure does not exist. Calculated phonon dispersion curves for a hypothetical Na_2SiH_6 revealed imaginary frequencies of the librational modes throughout the Brillouin zone and thus indicate dynamic instability of the system. Generally, larger alkali metals stabilize the structure by providing a larger separation of SiH_6^{2-} entities.

The oxidation state of Pt in A_2PtH_6 is +IV which implies that octahedral PtH_6^{2-} complexes correspond to a classic 18-electron system PtH_6^{2-}. The H ligand does not have the capability for π-interaction. Thus, Pt s, p and d_{eg} orbitals involve in six bonding molecular orbitals (MOs) whereas Pt d t_{2g}-orbitals correspond to non-bonding MOs. Both types of MOs are occupied by the 18 valence electrons which allows that two electrons can be assigned per Pt-H bond.[25] In contrast, SiH_6^{2-} is a 12-electron system and d-electrons are not involved in a simple MO description. As a consequence four occupied bonding MOs account for bonding to 6 ligands. SiH_6^{2-} is a hypervalent species.[26] Hypervalent bonding is unusual with hydrogen as a ligand and previously the only known all-hydrido hypervalent silicon was a gas phase ion, SiH_5^-.[25] Hypervalency is traditionally thought to require highly electronegative ligand, like fluorine.[27,28]

Lastly, gigapascal MA hydrogenations were employed for mixtures of LiH and B and a hydrogenated high-pressure phase was recovered. The recovered phase was confirmed to contain boron-hydrogen bonds by using the infrared spectroscopy (IR). Powder x-ray diffraction showed sharp diffraction lines indicating that the product is highly crystalline. Currently the composition and the structure of this recovered phase remains unknown.

6.2 References

1. Schüth, F.; Bogdanovic, B.; Felderhoff, M., *Chem. Commun*. **2004**, 2249

2. Sandrock, G.; Gross, K.; Thomas, G.; Jensen, C.; Meeker, D.; Takara, S., *J. Alloys Compd.* **2002**, 330-332, 696

3. Kohlmann, H.; Fischer, H.E.; Yvon, K., *Inorg. Chem.* **2001**, 40, 2608

4. Aoki, K.; Nagano, M.; Yanagitani, A., *J. Appl. Phys*. **1987**, 62, 3314

5. Sriraman, S.; Agarwal, S.; Aydil, E.S.; Maroudas, D., *Nature* **2002**, 418, 62

6. Leon-Escamilla, E.A.; Corbett, J.D., *J. Solid State Chem*. **2001**,159, 149

7. Leon-Escamilla, E.A.; Corbett, J.D., *J. Alloys Compd*. **1998**, 265, 104

8. Corbett, J.D.; Leon-Escamilla, E.A., *J. Alloys Compd*. **2003**, 356-357, 59

9. Eremets, M.I.; Trojan, I.A.; Medvedev, S.A.; Tse, J.S.; Yao, Y., *Science* **2008**, 319, 1506

10. Strobel, T.A.; Goncharov, A.F.; Seagle, C.T.; Liu, Z.; Somayazulu, M.; Struzhkin, V.V.; Hemley, R.J., *Phys. Rev.* B83 **2011**, 144102

11. Kim, D.Y.; Scheicher, R.H.; Mao, H,-K.; Kang, T.W.; Ahuja, R., *PNAS* **2009**, 107, 2793

12. Karazhanov, S.Zh.; Ulyashin, A.G.; Ravindran, P.; Vajeeston, P., *EPL* **2008**, 82, 17006

13. Budziak, A.; Zurek, M.; Zukrowski, J.; Balanda, M.; Pacyna, A.; Czapla, M., *J. Magn. Mater*. **2012**, 324, 735

14. Puhakainen, K.; Boström. M.; Groy, T.L.; Häussermann, U., *J. Solid State Chem.* **2010**, 183, 2528

15. Fukai Y., *J. Alloys Compd*. **2005**, 404-406, 7

16. Fukai, Y., *J. Less-Common Met*. **1991**, 172-174, 8

17. Nylén, J.; Sato, T.; Soignaard, E.; Yarger, J.L.; Stoyanov, E.; Häussermann, U., *J. Chem. Phys*. **2009**, 131, 104505

18. Bronger, W.; Müller, P.; Schmitz, D., *Z. Anorg. Allg. Chem*. **1984**, 516, 35

19. Bronger, W.; Auffermann, G., *Angew. Chem. Int. Ed*. **1994**, 33, 1112

20. Bronger, W.; Brassard, L.A., *Z. Anorg. Allg. Chem*. **1995**, 621, 1318

21. Puhakainen K.; Stoyanov, E.; Evans, M.J.; Leinenweber, K.; Häussermann, U., *J. Solid State Chem*. **2010**,183, 1785

22. Bublitz, D.; Peters, G.; Preetz, W.; Auffermann, G.; Bronger, W., *Z. Anorg. Allg. Chem*. **1997**, 623, 184

23. Puhakainen, K.; Benson, D.; Nylén, J.; Konar, S.; Stoyanov, E.; Häussermann, U., *Angew. Chem. Int. Ed.* **2012**, 51, 3156

24. Taketsugu, T.; Gordon, M.S., *J. Phys. Chem*. **1995**, 99, 14597

25. Albright, T.A.; Burdett, J.K.; Whangbo, M.-H., **1985**, *Orbital Interactions in Chemistry,* Wiley & Sons, Inc., page 280

26. Albright, T.A.; Burdett, J.K.; Whangbo, M.-H., **1985**, *Orbital Interactions in Chemistry,* Wiley & Sons, Inc., page 259

25. Musher, J.I., *Angew. Chem. Int. Ed*. **1969**, 8, 54

26. Noury, S.; Silvi, B*., Inorg. Chem*. **2002**, 41, 2164

COMPREHENSIVE REFERENCES

Albright, T.A., Burdett, J.K.; Whangbo, M.-H., **1985**, *Orbital Interactions in Chemistry,* Wiley & Sons, Inc., pages 259 and 280

Armbruster, M.; Wörle, M.; Krumeich, F.; Nesper, R., *Z. Allg. Anorg. Chem.* **2009**, 635, 1758

Ashcroft, N.W., *Phys. Rev. Lett.* **1968**, 21, 1448

Ashcroft, N.W., *Phys. Rev. Lett.* **2004**, 18, 187002

Bader, R.F.W., *Atoms in Molecules: A Quantum Theory,* Oxford University Press, Oxford, **1990**, pp. 1-52

Bashkin, I.O., *Z. Phys. Chem. Neue Folge* **1989**, 163, 469

Bearpark, M.J.; McGrady, G.S.; Prince, P.D.; Steed, J.W.*, J. Am.Chem. Soc.* **2001**, 123, 7736

Bellamy, L.J., *Infrared Spectroscopy* **1961***,* 28, 1059

Bento, A.P.; Bickelhaupt, F.M., *J. Org. Chem*. **2007**, 72, 2201

Birch, J., *Phys. Rev.* **1947**, 71, 809

Bittner, H.F.; Badcock, C.C., J. *Electrochem. Soc*. **1983**, 130, 193C

Björling, T.; Noréus, D.; Häussermann, U., *J. Am. Chem. Soc*. **2005**, 128, 817

Blöch, P.E., *Phys. Rev. B* **1994**, 50, 17953

Blöch, P.E.; Jespen, O.; Anderson, O.K., *Phys. Rev.* **1994**, 49, 16223

Bogdanovic, B.; Brand, R.A.; Marjanovic, A.; Schwickardi, M.; Tolle, J., *J. Alloys Compd.* **2000**, 302, 36

Boström, M.; Hovmöller, S., *J. Solid State Chem*. **2000**,153, 398

Bronger, W., *J. Alloys Compd*. **1995**, 229, 1

Bronger, W.; Auffermann, G., *Angew. Chem. Int. Ed*. **1994**, 33, 1112

Bronger, W.; Auffermann, G., *Chem. Mater*. **1998**, 10, 2723

Bronger, W.; Auffermann, G., *J. Alloys Compd*. **1995**, 228, 119

Bronger, W.; Auffermann, G.; *J. Alloys Compd*. **1995**, 219, 45

Bronger, W.; Auffermann, G.; Müller, P., J.*Less-Common Met*. **1986**, 116, 9

Bronger, W.; Brassard, L.A., *Angew. Chem. Int. Ed*. **1995**, 34, 898

Bronger, W.; Brassard, L.A., *Z. Anorg. Allg. Chem*. **1995**, 621, 1318

Bronger, W.; Brassard, L.A., *Z. Anorg. Allg. Chem*. **1996**, 622, 462

Bronger, W.; Brassard, L.; Müller, P.; Lebech, B.; Schultz, Th., *Z. Anorg. Allg. Chem.* **1999**, 625, 1143

Bronger, W.; Klessen, G.; Müller, P., *J. Less-Common Met*. **1985**, 109, L1

Bronger, W,; Müller, P.; Schmitz, D., *Z. Anorg.Allg. Chem*. **1984**, 516, 35

Bronger, W.; Müller, P.; Schmitz, D.; Spittank, H., *Z. Anorg. Allg. Chem*. **1984** , 516, 35

Bruker AXS, *TOPAS V4; General profile and structure analysis software for powder diffraction data*, User's manual, Karlsruhe, Germany, **2008**

Bruker, A.X.S., *TOPAS V4: General Profile and Structure Analysis Software for Powder Diffraction Data*, User's Manual, Karlsruhe, Germany, **2008**

Brun, T.O.; Jorgensen, J.D.; Misawa, M.; Rotella, F.J.; Susman, S., *J. Electrochem. Soc.* **1982**, 129, 2509

Bruzzone G.; Fransceshci, E.; Merlo, F., *J. Less-Comm. Metals* **1978**, 60, 59

Bublitz, D.; Peters, G.; Preetz, W.; Auffermann, G.; Bronger, W., *Z. Anorg. Allg. Chem*. **1997**, 623, 184

Budziak, A.; Zurek, M.; Zukrowski, J.; Balanda, M.; Pacyna, A.; Czapla, M., *J. Magn. Mater*. **2012**, 324, 735

Burtovyy, R.; Tkacz, M., *Solid State Commun*. **2004**, 131, 169

Bushmann, E., *Z. Anorg. Alleg Chem*. **1961**, 313, 90

Bäuerlein, P.; Antonius, C.; Löffler, J.; Kümpers, J., *J. Power Sources* **2008**, 176, 547

Chase Jr., M.W.; Davies, C.A.; Downey Jr., J.R.; Frurip, D.J.; McDonald, R.A.; Syverud, A.N.; *NIST-JANAF Thermochemical Tables*, National Institute of Standards and Technology, Gaithersburg, **1985**

Chen, J.; Sakai, T.; Kitamura, N.; Takeshita, H.T.; Kuriyama, N., *J. Am. Chem. Soc.* **2001***,* 123, 6193

Chuit, C.; Corriu, R.J.P.; Reye, C.; Young, J.C., *Chem. Rev*. **1993**, 93, 1371

Corbett, J.D.; Leon-Escamilla, E.A., *J. Alloys Compd*. **2003**, 356-357, 59

Corriu, R.; Guerin, C.; Henner, B.; Wang, Q., *Inorg. Chem. Acta* **1992**, 198-200, 705

Couzijin, E.P.A.; Ehlers, A.W.; Schakel, M.; Lammertsma, K., *J. Am.Chem. Soc.* **2006**, 128, 12364

Cudazzo, P.; Profeta, G.; Sanna, A.; Floris, A.; Continenza, A.; Massida, S., *Phys. Rev. Lett*. **2008**, 100, 257001

Didisheim, J.J.; Zolliker, P.; Yvon, K.; Fischer, J.; Gubelmann, M., *Inorg.Chem*. **1984**, 23, 1953

Dimitriev, V.; Filinchuk, Y.; Chernyshov, D.; Talyzin, A.V.; Dzwilewski, A.; Andersson, O.; Sundqvist, B*., Phys. Rev. B* **2008**, 77, 174112

Ding, F.; Liu, Y.; Hu, X., *Electrochem. Solid State Lett.* **2006**, 9, A72

Driessen, A.; Sänger, P.; Hemmes, H.; Griessen, R.J., *J. Phys. Condens. Matter* **1990**, 2, 9797

Eldik, R.; Klärner, F.-G., Ed. **2002** *High Pressure Chemistry,*Wiley-VCH, Wienheim, Germany

Eremets, M.I.; Trojan, I.A.; Medvedev, S.A.; Tse, J.S.; Yao, Y., *Science* **2008**, 319, 1506

Eriksson, L., PFILM, program for manipulation of powder diffractonmeter data, **2004**

Eriksson, L.; Computer Program PFILM, Stockholm University, Communication

Fahlquist, H.; Noreus, D.; Callear, S.; David, W.I.F.; Hauback, B.C., *J. Am. Chem. Soc.* **2011**, 133, 14574

Filinchuk, Y.; Chernyshov, D.; Cerny, R., *J. Phys. Chem. C* **2008**, 112, 10579

Firman, T.K.; Landis, C.R., J. *Am. Chem. Soc.* **1998**, 120, 12650

Flanagan, T.B.; Oates, W.A., *Annu. Rev. Mater. Sci.* **1991**, 21, 269

Fornasini, M.L.; Pani, M., *J. Alloys Compd*. **1994**, 205, 179

Frankcombe, T.J.; Kroes, G.-J.; Züttel, A., *Chem. Phys. Lett.* **2005**, 405, 73

Friedrichs, O.; Buchter, F.; Borgschulte, A.; Remhof, A.; Zwicky, C.N.; Mauron, Ph.; Bielmann, M.; Züttel, A., *Acta Mater.* **2008**, 56, 949

Fuchs, M.; Sheffler, M., *Comput. Phys. Commun*. **1999**, 119, 67

Fukai Y., *J. Alloys Compd*. **2005**, 404-406, 7

Fukai, Y., *J. Less-Common Met*. **1991**, 172-174, 8

Fukai, Y.; Mizutani, M., *Mat. Trans*. **2002**, 43, 1019

Fukai, Y.; Mori, K.; Shinomiya, H., *J. Alloys Compd*. **2002**, 348, 105

Fukai, Y.; Okuma, N., *Phys. Rev. Lett*. **1994**, 73, 1640

Fukai, Y.; Sugimoto, H., *J. Phys.: Condens. Matter* **2007**,19, 436201

Gingl, F.; Vogt, T.; Akiba, E., *J.Alloys Compd*. **2000**, 306, 127

Goedecker, S.; Teter, M.; Hutter, J*., Phys. Rev*. *B* **1996**, 58, 1703

Gonze, X.; Amadond, B.; Anglade, P.M.; Beuken, J.M; Bottin, F.; Bolanger, P.; Bruneval, F.; Caliste, D.; Carcas, R.; Côté, M.; Deutsch, T.; Genovese, L.; Ghosen, Ph.; Giantomassi, M.; Goedecker, S.; hamann, D.R.; Hermet, P.; Jollet, F.; Jomard, G.; Leroux, S.; Mancini, M.; Mazevet, S.; Oliveira, M.J.T.; Onida, G.; Pouillon, Y.; Rangel, T.; Rgnanese, G.M.; Sangalli, D.; Shaltaf, R.; Torrent, M.J.; Verstraete, M.J.; Zerah, G.; Zwanziger, J.W., *Comput. Phys. Commun*. **2009**, 180, 2582

Gonze, X.; Lee, C., *Phys. Rev*. *B* **1995**, 51, 8610

Gonze, X.; Lee, C., *Phys. Rev*. *B* **1997**, 55, 10355

Hallstedt, B.; Kim, O., *Int. J. Mater. Res.* **2007**, 98, 961

Hansen, D.A.; Smith, J., *Acta Crystallogr. B* **1968**, 24, 913

Harris, D.C.; Bertolucci, M.D., *Symmetry and Spectroscopy: An introduction to Vibrational and Electronic Spectroscopy*, Dover Publications Inc. New York, **1989**, pp. 90 – 189

Hartman, M.R.; Rush, J.J.; Udovic, T.J.; Bowman, R.C.; Hwang, S.J., *J. Solid State Chem*. **2007**, 180, 129

Hartwigsen, C.; Goedecker, S.; Hutter, J*., Phys. Rev*. B **1998**, 58, 3641

Hemmes, H.; Driessen, A.; Griessen, R.J., *C. Phys. Solid State Phys*. **1986**, 19, 3571

Henning, R.W.; Leon-Escamilla, E.A.; Zhao, J.T.; Corbett, J.D., *Inorg. Chem*. **1997**, 36, 1282

Hohenberg, P.; Kehn, W., *Phys. Rev*. *B* **1964**,136, 864

Holzapfel, W.B.; Isaacs N.S., Ed. **1997** *High-pressure Techniques in Chemistry and Physics*, Oxford University Press, New York

Hong, K., *J. Alloys Compd.* **2001**, 321, 307

http://www1.eere.energy.gov/hydrogenandfuelcells/storage/pdfs/targets_onboard_hydro_storage.pdf

Huang, B.Q.; Corbett, J.D., *Inorg. Chem.* **1997**, 36, 3730

Huot, J.; Boily, S.; Güther, V.; Schulz, R., *J. Alloys Compd*. **1999**, 383, 304

Hu, M.G.; van Paasschen, J.M.; Geanangel, R.A., *J. Inorg. Nucl. Chem*. **1977**, 39, 2147

Huppertz, H., *Z. Kristallogr*. **2004**, 219, 330

Häussermann, U., *Z. Kristallogr.* , **2008**, 223, 628

Häussermann, U.; Blomqvist, H.; Noreus, D., *Inorg. Chem*. **2002**, 41, 3684

Häussermann, U.; Kranak, V.F.; Puhakainen, K., Hydrogenous Zintl Phases: Interstitial Versus Polyanionic Hydrides, Structured and Bonding, Ed. Fässler, T., **2011**, 139, pp.143-163

Ivanov, E.; Konstanchcuk, I.; Boldyrev, V., *J. Less-Common Met*. **1991**, 131, 25

Ivanovic, N.; Novakovic, N.; Colognesi, D.; Radisavljevic, I.; Ostojic, S., *Int. J. Mod. Phys. B* **2010**, 24, 703

Johansson, M.; Lemmens, P., *J. Phys. ; Condens. Matter* **2008**, 20, 264001

Kamegawa, A.; Goto, Y.; Kataoka, R.; Takamura, H.; Okada, M., *Renew. Energy* **2008***,* 33, 221

Kang, J.K.; Kim, S.Y.; Han, Y.S.; Muller, R.P., Dooddard, W.A., *Appl. Phys. Lett.* **2005**, 87, 111904

Karazhanov, S.Zh.; Ulyashin, A.G.; Ravindran, P.; Vajeeston, P., *EPL* **2008**, 82, 17006

Kauzlarich, S.M., Ed., Chemistry, *Structure, and Bonding of Zintl Phases and Ions*, VCH, New York, **1996**

Kawai, N.; Endo, S., *Rev. Sci. Instrum*. **1970**, 41, 1178

Ke, X.; Tanaka, I., *Phys. Rev. B* **2005**, 71, 024117

Khvostantsev, L.G.; Slesarev, V.N.; Brazhkin, V.V., *High Pressue Res*. **2004**, 24, 371

Kim, D.Y.; Scheicher, R.H.; Mao, H.-K.; Kang, T.W.; Ahuja, R., *PNAS* **2009**, 107, 2793

King, R.B., *Coord. Chem. Rev*. **2000**, 200-202, 813

Klug, H.P.; Alexander, I.E., *X-ray Diffraction Procedures*, 2nd ed., Wiley, New York, **1974**

Knox K.; Ginsberg, A.P., *Inorg. Chem.* **1964**, 3, 555

Kohlmann, H.; Fischer, H.E.; Yvon, K., *Inorg. Chem.* **2001**, 40, 2608

Kohn, W.; Sham, L.J.*, Phys. Rev. B* **1965**,140,1133

Krack, M., *Theor. Chem. Acc*. **2005**, 114, 145

Kresse, G.; Furthmüller, J., *Comput. Mater. Sci*. **1996**, 6 , 15

Kresse, G.; Furthmüller, J., *Phys. Rev*. B **1996**, 54, 11169

Kresse, G.; Hafner, J., *Phys. Rev*. B **1993**, 47, 558

Kresse, G.; Joubert, J., *Phys. Rev*. B **1999**, 59, 1758

Kuriyama, K., *Acta Cryst. B* **1975**, 31, 1793

Kyoi, D.; Sato, T.; Rönnebro, E.; Kitamura, N.; Ueda, A.; Ito, M.; Katsuyama, S.; Hara, S.; Noréus, S.; Sakai, T., *J. Alloys Compd*. **2004**, 372, 213

Lee, M.H.; Evans, M.J.; Daemen, L.L.; Sankey, O.F.; Häussermann, U., *Inorg. Chem.* **2008**, 47, 1496

Leon-Escamilla, E.A.; Corbett, J.D., *J. Alloys Compd*. **1994**, 206, L15

Leon-Escamilla, E.A.; Corbett, J.D., *J. Alloys Compd*. **1998**, 265, 104

Leon-Escamilla, E.A.; Corbett, J.D., *J. Solid State Chem*. **2001**,159, 149

Leon-Escamilla, F.A.; Corbett, J.D., *Z. Inorg. Chem.* **2001**, 40, 1226
Li, C.; Peng, P.; Zhow, D.W.; Wan, L., *Int. J. Hydrogen energy* **2001**, 36, 14512

Lin, Y.; Mao, W.L.; Drozd, V.; Chen, H.H.; Daemen, L.L., *J. Chem. Phys.* **2008**, 129, 234509

Liu, D.M.; Huang, W.J.; Si, T.Z.; Zhang, Q.A*., J. Alloys Compd*. **2013**, 551, 8

Lodziana, Z.; Vegge, T., *Phys. Rev. Lett.* **2004**, 93, 145501

Manfrinetti, P.; Fornasini, M.L.; Palenzona, A., *Intermetallics* **2000**, 8, 223

Mao, H.-K.; Bell, P.M., *Science* **1979**, 203, 1004

Marzari, N.; Vanderbilt, D*., Phys. Rev*. *B* **1997**, 56, 12847

McAllister, A.J., *Bull. Alloy Phase Diagrams* **1982**, 3, 177

Melendes, C.A.; Sy, C.C., *J. Electrochem. Soc.* **1978**, 125, 727

Mellosta von Colbe, J.M.; Felderhoff, M.; Bogdanovic, B.; Schüth, F.; Weidenthaler, C., *Chem. Commun.* **2005**, 37, 4732

Mettler-Toledo GmbH, *Thermal Analysis, DSC Evaluation*, User's Manual, Schwerzenbach, Switzerland, **2003**

Minkwitz, R.; Schneider, S.; Kornath, A., *Inorg. Chem*. **1998**, 37, 4662

Moc, J., J. *Mol. Struct*. **1999**, 461-462, 249

Monkhorst, H.J.; Pack, J.D., *Phys. Rev*. *B* **1976**, 13, 5188

Musher, J.I., *Angew. Chem. Int. Ed*. **1969**, 8, 54

Myles, K.M.; Mrazek, F.C.; Smaga, J.A.; Seetle, J.L., ERDA Report ANL-76-8, *Argonne National Laboratory* **1976**, pp. B50-B73

Müller, W.; Stöhr, J., *Z. Naturforsch. B* **1977**, 32, 631

Nacken, B.; Bronger, W., *J. Less-Common Met*. **1977**, 52, 323

Nagorsen, G.; Posch, H.; Schäfer. H.; Weiss, A., Z. *Naurforcshg*. **1969**, 24b,1191

Nesper, R., *Prog. Solid State Chem.* **1990**, 10, 1

Noreus, D.; Törnroos, L.W.; Börje, A.; Szabo, T.; Bronger, W.; Spittank, H.; Auffermann, G.; Müller, P., *J. Less-Common Met*. **1988**, 139, 233

Noreus. D.; Törnroos, K.W.; Börje, A.; Szabo, T.; Bronger, W.; Spittnak, H.; Auffermann, G.; Müller, P., *J.Less-Common Met* **1988**, 139, 233

Noury, S.; Silvi, B*., Inorg. Chem*. **2002**, 41, 2164

Nylen, J.; Sato, T.; Soignaard, E.; Yarger, J.L.; Stoyanov, E.; Häussermann, U., *J. Chem. Phys*. **2009**, 131, 104505

Ohno, K.; Matsuura, H.; Endo, Y.; Hirota, E., *J. Mol. Spectrosc*. **1985** 111, 73

Olofsson-Mårtensson, M.; Häussermann, U.; Tomkinson, J.; Noreus, D., *J. Am. Chem. Soc*. **2000**, 122, 6960

Orimo, S.; Nakamori, Y.; Eliseo, J.R.; Züttel, A.; Jensen, C.M., *Chem. Rev*. **2007**, 107, 4111

Orimo, S.-I.; Nakamori, Y.; Ohba, N. ; Miwa, K. ; Aoki, M.; Towata, S.; Züttel. A., *Appl. Phys. Lett.* **2006**, 89, 021920

Ozawa, K., *Solid State Ionics* **1994**, 69, 212

Parker, S.F., *Coord. Chem. Rev*. **2010**, 254, 215

Parker, S.F; Bennington, S.M.; Ramirez-Cuesta, A.J.; Auffermann, G.; Bronger, W.; Herman, H.; Williams, K.P.J.; Smith, T., *J. Am. Chem. Soc*. **2003** , 125, 11656

Pedrew, J.P.; Wang, J., *Phys. Rev. B* **1992**, 45, 13244

Perdew, J.P.; Burke, K.; Ernzerhof, M., *Phys. Rev. Lett*. **1996**, 77, 3865

Pierrefixe, S.C.A.H.; Guerra, C.F.; Bickelhaupt, F.M., *Chem. Eur. J*. **2008**, 14, 819

Pistorius C.W.F.T., *Z. Phys. Chem., Neue Folge* **1974**, 88, 253

Prince, P.D.; Bearpark, M.J.; McGrady, G.S.; Steed, J.W., *Dalton Trans*. **2008**, 271

Puhakainen, K.; Benson, D.; Nylén, J.; Konar, S. ; Stoyanov, E. ; Leinenweber, K.; Häussermann, U., *Angew. Chem. Int. Ed.* **2012**, 51, 3156

Puhakainen, K.; Boström. M.; Groy, T.L.; Häussermann, U., *J. Solid State Chem.* **2010**, 183, 2528

Puhakainen K.; Stoyanov, E.; Evans, M.J.; Leinenweber, K.; Häussermann, U., *J. Solid State Chem*. **2010**, 183, 1785

Pulham, R.J.; Hubberstey, P.; Hemptenmacher, P., *J. Phase Equilibria* **1994**, 15, 587

Retuerto, M.; Sánchez-Benítez, J.; Rodríguez-Canas, E.; Serafini, D.; Alonso, J.A., *Int. J. Hydrogen Energy* **2010**, 35, 7835

Reuter, K.; Scheffler, M., *Phys. Rev. B* **2001**, 65, 035406

Rioja, R.J.; Liu, J., *Metallurg. Mater. Transactions* **2012**, 43A, 3326

Rönnebro, E.; Kitamura, N.; Sakai, T.; *J. Alloys Compd*. **2003**, 358, 216

Sabine, T.M.; Hunter, B.A.; Sabine, W.R.; Ball, C.J., *J. Appl Crystallogr*. **1998**, 31, 47

Saitoh, H.; Machinda, A.; Katayama, Y.; Aoki, K., *Appl. Phys. Lett*. **2008**, 93, 151915

Sandrock, G.; Gross, K.; Thomas, G.; Jensen, C.; Meeker, D.; Takara, S., *J. Alloys Compd.* **2002**, 330-332, 696

Schäfer, H.; Eisenmann, B.; Müller, W., *Angew. Chem. Int. Ed.* **1973**, 12, 694

Schürmann, E.; Voss, H.-J., *Giessereiforschung* **1981**, 33, 33

Schüth, F.; Bogdanovic, B.; Felderhoff, M., *Chem. Commun*. **2004**, 2249

Shah, A.; Torres, P.; Tscharner, R.; Wyrsch, N.; Keppner, H., *Science* **1999**, 285, 692

Shannon, R.D., *Acta Cryst.* **1976**, A32, 751

Sheldrik, G.M.*, SADABS Version 2.*10, University of Göttingen, Germany, **2003**

Sheldrik, G.M., *SHELX97 and SHELXL97*, University of Göttingen, Germany, **1997**

Shizuku, Y.; Yamamoto, S.; Fukai, Y., *J. Alloys Compd*. **2002**, 336, 159

Soulié, J.-Ph.; Renaudin, G.; Cerny, R.; Yvon, K., *J. Alloys Compd*. **2002**, 346, 200

Sriraman, S.; Agarwal, S.; Aydil, E.S.; Maroudas, D., *Nature* **2002**, 418, 62

Stoyanov, E.; Häussermann, U.; Leinenweber, K., *High Pressure Res*. **2010**, 30, 175

Street, R.A., *Phys. States Solid* **1998**, A166, 695

Stritzker, B.; Buckel, W., *Z. Physik* **1972**, 257, 1

Strobel, T.A.; Goncharov, A.F.; Seagle, C.T.; Liu, Z.; Somayazulu, M.; Struzhkin, V.V.; Hemley, R.J., *Phys. Rev.* B83 **2011**, 144102

Stöhr, J.; Schäfer, H., *Z. Naturforsch. B* **1979**, 34, 653

Su, Z.; Ye, J.Y.; Zhou, R.F.; Duan, Y.S., *Rare Met. Mater. Eng.* **2012**, 41, 731

Sugimoto, H.; Fukai, Y., *Acta Mat*. **1992**, 40, 2327

Takamura, H.; Kakuata, H.; Goto, Y.; Kamegawa, A.; Okada, M., *Mater. Trans*. **2001**, 42, 1301

Taketsugu, T.; Gordon, M.S., *J. Phys. Chem*. **1995**, 99, 14597

Tang, W.; Sanville, E.; Henkelman, G., *J. Phys.: Condens. Mat.* **2009**, 49. 084204

Tebbe, K.-F.; von Schnering, H.G.; Rütter, B.; Rabeneck, G., *Z. Naturforsch. B* **1973**, 28, 600

Tkacz, M., *Defect Diffusion Forum* **2002**, 208-209, 107

Tkacz, M.; Litwiniuk, A., *J. Alloys Compd.* **2002**, 330-332, 89

Van Vucht, J.H.N.; Kuijpers, F.A.; Bruning, H.C.A.M., *Philips Res. Rep*. **1970**, 25, 133

Walker D.; Carpenter, M.A.; Hitch, C.M., *A. Mineral*. **1990**, 75, 1020

Wang, L.; Bao, K.; Meng, X.; Wang, X.; Jiang, T.; Cui, T.; Liu, B.; Zou, G., *J. Chem. Phys*. **2011**, 134, 024517

Wang, J.; Ebner, A.D.; Ritter, J.A., *J. Phys. Chem.* **2007**, C111, 4917

Wang, Y.; Hua, W.; Qu, J.; Xie, L.; Li, X., *J. Int. Hydrogen Energy*, **2008**, 33, 7207

Wang, Y.; Perdew, J.P., *Phys. Rev. B* **1991**, 44, 13298

Wannier, G.H., *Phys. Rev*. **1937**, 52, 191

Werner, P.E., *Ark. Kemi* **1969**, 31, 513

Werner, P.E.; Eriksson, L.; Westdahl, M., *J. Appl. Cryst*. **1995**, 18, 367

Wu, H.; Hartman, M.R.; Udovic, T.J.; Rush, J.J.; Zhou, W.; Bowman, R.C.; Vajo, J.J., *Acta Cryst. B* **2007**, 63, 63

Wu, H.; Zhou, W.; Udovic, T.J.; Rush, J.J., *Chem. Mater.* **2007**, 19, 329

Wu, H.; Zhou, W.; Udovic, T.J.; Rush, J.J.; Yilderim, T., *Phys. Rev. B* **2006**, 74, 224101

Wu, H.; Zhou, W.; Udovic, T.J.; Rush, J.J.; Yilderim, T., *Chem. Phys. Lett.* **2008**, 460, 432

Yamawaki, H.; Fujisha, H.; Gotoh, Y.; Nagano, S., *J. Alloys Compd.* **2012**, 514, 111

Yvon, K., *Chimia* **1998**, 52, 613

Yvon, K., *J. Less-Common Met*. **1984**,103, 53

Zarkevich, N.A.; Johnson, D.D., *Phys. Rev. Lett*. **2008**, 100, 040602

Zintl, E.; Brauer, G., *Z. Phys. Chem. B* **1933**, 20, 245

Zintl, E.; Woltersdorf, G., *Z Angew. Phys. Chem* **1935**, 41, 876

APPENDIX A

PXRD OF Li_2Al AND Li_9Al_4

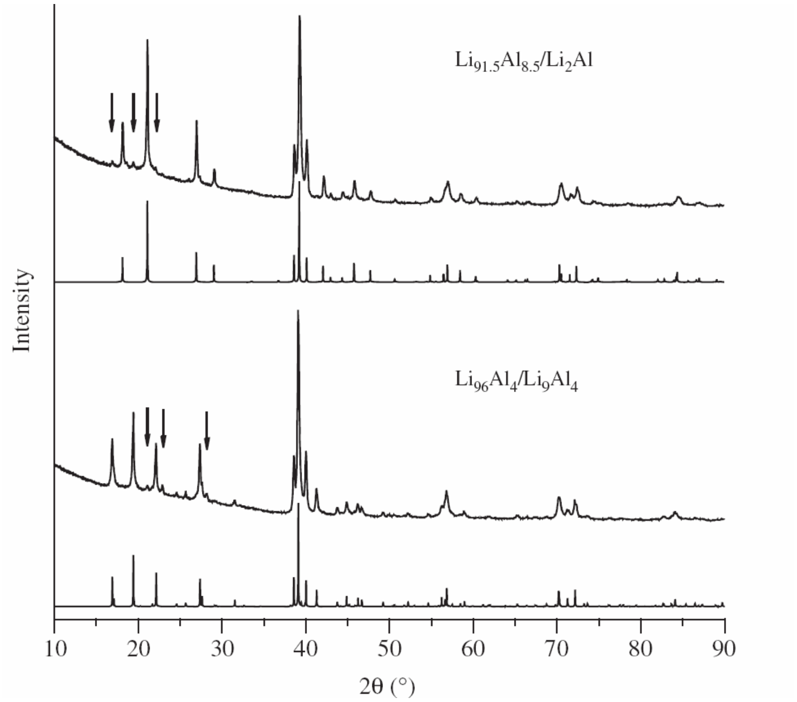

Figure A. PXRD (Cu*K*α) patterns of a new phase Li_2Al and a known Li_9Al_4. Theoretical patterns for both phases underneath the experimental diffractogram.

Additional reflections, which are indicated by arrow, are identified as follows; In orthorhombic Li_2Al, the arrows correspond to a small amount of Li_9Al_4 whereas in monoclinic Li_9Al_4 the arrows indicate the additional weak reflections which remain unidentified. The powder x-ray diffraction confirmed that the bulk sample corresponds to structure found in the single crystal x-ray refinements.

APPENDIX B

SCXRD REFINEMENT FOR Li_2Al AND Li_9Al

Li_2Al and Li_9Al_4

Table B. Atomic coordinates and displacement parameters

	Atom	Wyck.	Occ.	x	y	z	U_{iso} (Å^2)
Li_2Al	Al	4c	1	0	0.07477(9)	¼	0.0186(3)
	Li1	4c	0.95	0	0.7582(5)	¼	0.034(2)
	Al1	4c	0.048(5)				
	Li2	4c	0.96	½	0.4093(5)	¼	0.033(2)
	Al2	4c	0.036(6)				
Li_9Al_4	Al1	4i	1	0.15030(2)	0	0.21378(6)	0.0158(1)
	Al2	4i	1	0.38538(1)	0	0.06429(5)	0.0166(1)
	Li1	2a	1	0	0	0	0.0263(7)
	Li2	4i	1	0.0856(1)	0	0.3590(4)	0.0186(4)
	Li3	4i	1	0.2330(1)	0	0.8431(4)	0.0301(6)
	Li4	4i	1	0.3081(1)	0	0.4764(4)	0.0215(5)
	Li5	4i	1	0.4566(1)	0	0.6745(4)	0.0266(5)

Table B2. Interatomic distances in Li_2Al and Li_9Al_4

Atom pair	Li_2Al	Atom pair	Li_9Al_4	Atom pair	Li_9Al_4
Al-Al × 2	2.678(1)	Al1-Al2 × 2	2.6962(6)	Al2-Al1 × 2	2.6962(6)
-Li1 × 2	2.775(3)	Al1-Li1	2.7748(9)	-Li2 × 2	2.733(1)
-Li2 × 2	2.835(3)	-Li2 × 4	2.797(1)	-Li5	2.788(2)
-Li1 × 2	2.938(2)	-Li3	2.853(2)	-Li3	2.817(2)
-Li1	3.092(5)	-LI2	2.891(2)	-Li5	2.954(2)
-Li2 × 4	3.2386(8)	-Li4	2.951(2)	-Li4	2.975(2)
-Li2	3.268(5)	-Li2	3.027(2)	-Li4	3.140(2)
		-Li4 × 2	3.188(2)	-Li1 × 2	3.2079(5)
		-Li3 × 2	3.224(1)	-Li5	3.231(3)
		-Li3	3.362(2)	-Li3 × 2	3.306(1)
		Li1-Al1 × 2	2.7748(9)		
		-Li2 × 2	2.840(2)		
		-Li5 × 2	2.847(2)		
		-Al2 × 2	3.2079(5)		
		-Li2 × 2	3.430(2)		
Li1-Li2 × 2	2.757(4)	Li2-Li3	2.716(3)	Li4-Li3	2.730(3)
-Al × 2	2.775(3)	-Al2 × 2	2.733(1)	-Li5	2.731(4)
-Li2 × 2	2.778(4)	-Li5 × 2	2.815(2)	-Al1× 2	2.797(1)
-Al × 2	2.938(3)	-Li1	2.840(2)	-Li3× 2	2.824(2)
-Al	3.092(5)	-Al1	2.891(2)	-Al1	2.951(2)
-Li1 × 4	3.239(1)	-Al1	3.027(2)	-Al3	2.975(2)
-Li2	3.408(6)	-Li4 × 2	3.193(2)	-Al2	3.140(2)
		-Li2	3.199(2)	-Li2 × 2	3.193(2)
		-Li5 × 2	3.361(3)	-Li4 × 2	3.203(3)
		-Li1	3.430(2)	-Li3	3.357(3)
Li2-Li1 × 2	2.757(4)	Li3-Li2	2.716(3)	Li5-Li4	2.731(4)
-Li1 × 2	2.778(4)	-Li4	2.730(3)	-Al2	2.788(2)
-Al × 2	2.853(3)	-Li3 × 2	2.794(2)	-Li5	2.814(4)
-Li2 × 2	2.860(6)	-Al2	2.817(2)	-Li2 × 2	2.815(2)
-Al × 4	3.239(1)	-Li4 × 4	2.824(2)	-Li1 × 2	2.847(2)
-Al	3.267(4)	-Al1	2.853(2)	-Al2	2.954(2)
-Li1	3.408(6)	-Al1 × 2	3.224(1)	-Al1× 2	3.188(2)
		-Al2 × 2	3.306(1)	-Al2	3.231(3)
		-Li4	3.357(3)	-Li2 × 2	3.361(3)
		-Al1	3.362(2)	-Li5	3.483(5)

APPENDIX C

THEORETICAL CALCULATIONS OF SILICON HEXAHYDRIDES

Theoretical calculations of the electronic structure were performed using the first- principles all-electron projected augmented wave (PAW) method as implemented by the Vienna Ab Initio Simulation Package (VASP).[1,2] Exchange-correlation effects were treated within the generalized gradient approximation (GGA) using the Perdew-Burke-Ernzerhof (PBE) parameterization.[3,4] The structures were relaxed with respect to volume, lattice parameters, and atomic positions. Forces were converged to better than 1×10^{-3} eV/Å. The equilibrium volume was obtained by fitting to a third order Birch-Murnaghan equation of state.[5] The integration over the Brillioun Zone (BZ) was done on a grid of special k-points with size 11×11×11 (6×6×6 for the equation of state) determined according to the Monkhorst-Pack scheme using Gaussian smearing to determine the partial occupancies for the wavefunctions.[6] For calculations using VASP, the energy cutoff was set to 500 eV (K_2SiH_6 and KH), 550 eV (K_2SiH_6), and 600 eV (Rb_2SiH_6). To obtain the band structure and for Bader analysis[7] charge densities were calculated using the tetrahedron method with Blöchl correction[8] for BZ integration. Bader analysis of the charge densities was performed according to Ref. 9. To achieve a high accuracy for the Bader analysis, the mesh for the augmentation charges was substantially increased. The error of calculated Bader charges is smaller than 0.01 e per atom.

The maximally localized Wannier functions (MLWFs), phonon dispersion relations and thermodynamic functions were calculated via the plane wave code Abinit[10] employing the GGA-PBE as the exchange correlation. Si, H, and F pseudopotentials were obtained from the fhi98PP package.[11] For K and Rb the pseudopotentials according to Goedecker, Teter, and Hutter were used.[12-13] These potentials are optimized for use with GGA-PBE. A 6×6×6 Monkhorst-Pack symmetry-adapted k-point grid was used to calculate the MLWFs; for calculating phonon dispersions a grid composed of 256 k-points was employed. The MLWFs were calculated using a planewave energy cutoff of 50 Hartree (K_2SiH_6), and 60 Hartree (K_2SiF_6). The structural parameters correspond to the relaxed structure obtained from the VASP calculations described above. The MLWFs were calculated using 14 (K_2SiH_6) and 32 (K_2SiF_6) occupied bands. Because the Bloch orbitals are indeterminant in phase and can be degenerate in the band at distinct values of k, the Wannier functions are non-unique.[15-17] For this reason the Wannier functions in Equation (1) below

$$\left|\omega_{n\bar{R}}\right\rangle = \frac{V}{(2\pi)^3}\int_{BZ}\left[\sum_{m=1}^{N} U_{mn}^{\bar{k}}\left|\psi_{m\bar{k}}\right\rangle\right] e^{-i\bar{k}\cdot\bar{R}}\, d\bar{k}$$

at lattice vector R are constructed from a series of unitary transformations U^{K}_{mn} of the Bloch bands $\left|\psi_{n\bar{k}}(\bar{r})\right\rangle$. The unitary matrices U^{K}_{mn} are then chosen so that they minimize the spread Ω of the MLWF's. The spread is defined in Equation (2) below as

$$\Omega = \sum_{n}^{N}\left[\left\langle \omega_{n\bar{0}}\right| r^2 \left|\omega_{n\bar{0}}\right\rangle - \left\langle \omega_{n\bar{0}}\right| r \left|\omega_{n\bar{0}}\right\rangle^2\right]$$

Once the spread is iteratively minimized, using conjugate gradient and steepest descent minimization routines, the resultant orbitals of Eq. (1) are the MLWF's. The miminum of the total spread of the MLWFs was 11.43 Å^2 (K_2SiH_6) and 14.62 Å^2 (K_2SiF_6) with a change in spread from the previous iteration for all MLWFs of less than 1×10^{-12} Å^2. The total number of Wannier functions calculated was 14 for K_2SiH_6 and 32 for K_2SiF_6. For K_2SiH_6, there were six Wannier orbitals along the Si-H bond with a spread of 1.20 Å^2 and eight orbitals located on the K ions with a spread of 0.528 Å^2. For K_2SiF_6, there were six Wannier orbitals along the Si-F bond with a spread of 0.438 Å^2, eight orbitals located on the K ions with a spread of 0.518 Å^2, and 18 orbitals located around the F atoms with a spread of 0.436 Å^2.

The vibrational properties of each system were calculated via the quasiharmonic approximation (QHA) using density functional perturbation theory (DFPT).[18-20] In the QHA, the phonons are harmonic but they depend on the volume of the unit cell. The unit cell was expanded or compressed to a target volume and then structurally relaxed with respect to cell shape and atomic position while keeping the crystal symmetry of the cell. Forces were converged to less than 1x10-4 eV/Å. At this volume a self consistent calculation was performed to obtain the electronic energy of the unit cell, then phonon calculations were executed to obtain thermodynamic functions of the material.[20] The strategy is outlined as follows. The thermodynamic functions (per unit cell) including the Helmholtz free energy Δ*F* (Equation 3) the phonon internal energy ΔE (Equation 4), the constant-volume specific heat C_v (Equation 5), and the entropy S (Equation 6), at temperature *T* are given by:

$$\Delta F = 3nk_BT\int_0^{\omega_L} \ln\left\{2\sinh\frac{\hbar\omega}{2k_BT}\right\}g(\omega)\,d\omega$$

$$\Delta E = 3n\frac{\hbar}{2}\int_0^{\omega_L} \omega\coth\left(\frac{\hbar\omega}{2k_BT}\right)g(\omega)\,d\omega$$

$$C_v = 3nk_B\int_0^{\omega_L}\left(\frac{\hbar\omega}{2k_BT}\right)^2 \operatorname{csch}^2\left(\frac{\hbar\omega}{2k_BT}\right)g(\omega)\,d\omega$$

$$S = 3nk_B\int_0^{\omega_L}\left[\frac{\hbar\omega}{2k_BT}\coth\frac{\hbar\omega}{2k_BT} - \ln\left\{2\sinh\frac{\hbar\omega}{2k_BT}\right\}\right]g(\omega)\,d\omega$$

where k_B is the Boltzmann constant, *ω* is the phonon frequency, ω_L is the maximum frequency and *n* is the number of atoms in the unit cell. The phonon density of states (PDOS) g(ω) is calculated as

$$g(\omega) = \frac{1}{3n}\sum_{\vec{q},l}\delta\left(\omega - \omega(\vec{q},l)\right)$$

where q and l are the phonon wavevector and the mode, respectively.[28] Once the functions (3) to (6) are known it is possible to calculate Helmholtz free energy F (Equation 7), internal energy E (Equation 8), enthalpy H (Equation 9) and Gibbs free energy G (Equation 10).

$$F = E_{elec} + \Delta E - TS$$

$$E = E_{elec} + \Delta E$$

$$H = E_{elec} + \Delta E + pV$$

$$G = E_{elec} + \Delta E - TS + pV$$

To obtain the final thermodynamic functions that are used for calculation of the reaction energies the QHA was applied to each system in the low temperature limit (T → 0). In the low temperature limit the phonon internal energy is equivalent to the zero-point energy is

$$E_{ZP} = \lim_{T\to 0} \Delta E = 3n\frac{\hbar}{2}\int_{0}^{\omega_L} \omega g\left(\omega\right) d\omega$$

The ZP equilibrium volume V^0_{ZP} is then obtained by fitting a third order Birch-Murnaghan equation of state to the Helmholtz free energy *F* in this low temperature limit. The thermodynamic functions of the system are then recalculated at V^0_{ZP} using the harmonic approximation and used to calculate the reaction energies.

Hydrogen is gaseous; therefore its thermodynamic functions cannot be obtained in the same way as the crystalline materials above. Instead, the Gibbs free energy of hydrogen gas molecule is calculated as Equation 11 shows

$$G_{H_2}\left(T\right) = E_{elec,H_2} + E_{ZP,H_2} + pV + \Delta G_{H_2}\left(T\right)$$

Where $E_{elec,H2}$ is the electronic energy of hydrogen obtained from *ab inito* calculations, $E_{ZP,H2}$ *E* is the ZP energy obtained from phonon calculations and ΔG_{H2} (T) is the Gibbs free energy with respect to 0 K. The pressure and volume term is treated with the ideal gas law $pV=Nk_BT$, where *N* is 1 molecule of hydrogen gas and ΔG_{H2} (T) can be calculated using Equation 12 below.[20,21]

$$\Delta G_{H_2}\left(T\right) = \left[H_{H_2}\left(T\right) - H_{H_2}\left(0\right)\right] - T\left[S_{H_2}\left(T\right) - S_{H_2}\left(0\right)\right]$$

For assessing ΔG_{H2} (T) the enthalpy H_{H2} (T) and entropy S_{H2} (T), at temperature *T* of hydrogen at the standard pressure of 1 atm were extracted from the JANAF Thermochemical Tables.[22]

References

1. a) Blöch, P.E., *Phys. Rev. B* **1994**, 50, 17953; b) Kresse, G.; Joubert, J., *Phys. Rev. B* **1999**, 59, 1758

2. a) Kresse, G., *Phys. Rev. B* **1993**, 48, 13115; b) Kresse, G.; Furthmüller, J., *Comput. Mat. Sci.* **1996**, 6, 15

3. a) Wang, Y.; Perdew, J.P., *Phys. Rev. B* **1991**, 44, 13298; b) Perdew, J.P.; *Phys. Rev. B* **1992**, 46, 6671

4. Perdew. J.P.; Burke, K.; Ernzerhof, M., *Phys. Rev. Lett.* **1996**, 77, 3865

5. Birch, J., *Phys. Rev.* **1947**, 71, 809

6. Monkhorst, H.J.; Pack, J.D., *Phys. Rev. B* **1976**, 13, 5188

7. Bader, R.F.W., *Atoms in Molecules: A Quantum Theory*, Oxford University Press, Oxford, **1990**, p. 1-52

8. Blöch, P.E.; Jespen, O.; Anderson, O.K., *Phys. Rev. B* **1994**, 49, 16223

9. a) Armaldsen, A.; Tang, Q.; Henkelman, G., http://theory.cm.utexas.edu/bader/ b) Tang, W.; Sanville, E.; Henkelman, G., *J.Phys.: Condens. Mat.* **2009**, 21, 084204

10. Gonze, X.; Amadond, B.; Anglade, P.M.; Beuken, J.M.; Bottin, F.; Boulanger, P.; Brunevalt, F.; Caliste, D.; Carcas, R.; Cote, M.; Deutsch, T.; Genovese, L.; Ghosen, Ph.; Giantomassi, M.; Goedecker, S.; Hamann, D.R.; Hermet, P.; Jollet, F.; Jomard, G.; Leroux, S.; Mancini, M.; mazevet, S.; Oliveira, M.J.T.; Onida, G.; Pouillon, Y.; Rangel, T.; Rignanese, G.M.; Sangalli, D., Shaltaf, R.; Torrent, M.; Verstraete, M.J.; Zerah, G.; Zwanziger, J.W., *Comput. Phys. Commun.* **2009**, 180, 2582

11. Fuchs, M.; Scheffler, M.; *Comput. Phys. Commun.* **1999**, 119, 67

12. Goedecker, S.; Teter, M.; Hutter, J., *Phys. Rev. B* **1996**, 54, 1703

13. Hartwigsen, C.; Goedecker, S.; Hutter, J.; *Phys. Rev. B* **1998**, 58, 3641

14. Krack, M., *Theor. Chem. Acc.***2005**, 114, 145

15. Marzari, N.; Vanderbilt, D., *Phys. Rev. B* **1997**, 56, 12847

16. Mostofi, A.A.; Yates, J.R.; Lee, Y.S.; Souza, I.; Vanderbilt, D.; Marzari, M., *Comput. Phys. Commun.* **2008**, 178, 685

17. Souza, I, Marzari, N.; Vanderbilt, D., *Phys. Rev. B* **2001**, 65, 035109

18. Gonze, X.; Lee, C., *Phys. Rev. B* **1997**, 55, 10355

19. Gonze, X.; Lee, C., *Phys. Rev. B* **1995**, 51, 8610

20. Ke, X.; Tanaka, I., *Phys. Rev. B* **2005**, 71, 024117

21. Reuter, K.; Scheffler, M., *Phys. Rev. B* **2001**, 65, 035406

22. Chase Jr., M.W.; Davies, C.A.; Downey, J.R.; Frurip, D.J.; McDonald, R.A.; Syverud, A.N., *NIST JANAF THERMOCHEMICAL TABLES*, National Institute of Standards and Technology, Gaithersburg, MD, **1985**

APPENDIX D

PERMISSION: FIG. 1.8

AMERICAN INSTITUTE OF PHYSICS LICENSE
TERMS AND CONDITIONS

License Number 3124961481394

Publisher American Institute of Physics

Publication Journal of Chemical Physics

Article Title Thermal decomposition of ammonia borane at high pressures

Author Johanna Nylén, Toyoto Sato, Emmanuel Soignard, Jeffery L. Yarger, et al.

Online Publication Date Sep 11, 2009

Volume number 131

Issue number 10

Type of Use Thesis/Dissertation

Requestor type Student

Format Print and electronic

Portion Figure/Table Number of figures/tables1

Title of your thesis / dissertation In search of novel metal hydride materials using autoclave and multi-anvil hydrogenations

Expected completion date May 2013

Estimated size (number 120of pages

APPENDIX E

PERMISSION: FIG. 1.9

This is a License Agreement between Kati Puhakainen ("You") and Elsevier ("Elsevier") provided by Copyright Clearance Center ("CCC"). The license consists of your order details, the terms and conditions provided by Elsevier, and the payment terms and conditions.

License number 3124970228601

Licensed content publication Journal of Alloys and Compounds

Licensed content title The structure and phase diagram of M–H systems at high chemical potentials—High pressure and electrochemical synthesis

Licensed content author Y. Fukai

Licensed content volume/pages number 404–406 7-15

Type of Use reuse in a thesis/dissertation

Portion figures/tables/illustrations Format both print and electronic

Are you the author of this Elsevier article? No

Title of your thesis / dissertation In search of novel metal hydride materials using autoclave and multi-anvil hydrogenations

Expected completion date May 2013

Estimated size 120 (number of pages)

APPENDIX F

PERMISSION: FIG. 2.7

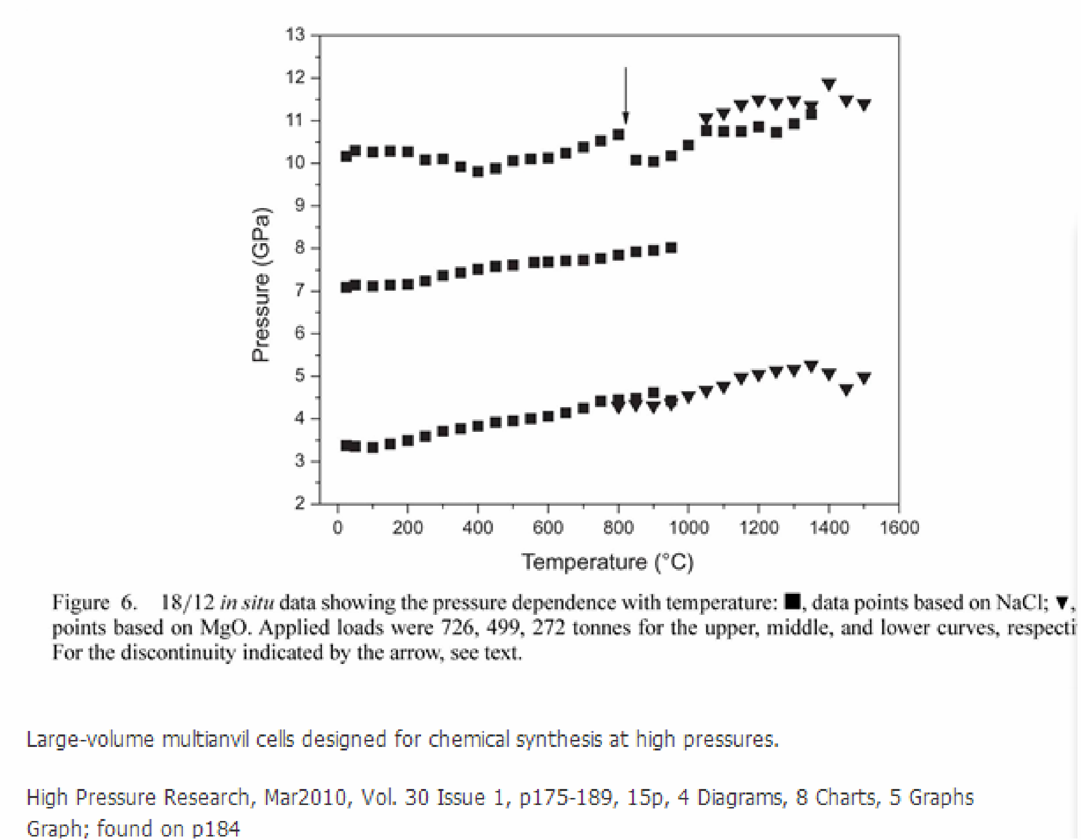

Figure 6. 18/12 *in situ* data showing the pressure dependence with temperature: ■, data points based on NaCl; ▼, points based on MgO. Applied loads were 726, 499, 272 tonnes for the upper, middle, and lower curves, respecti For the discontinuity indicated by the arrow, see text.

Large-volume multianvil cells designed for chemical synthesis at high pressures.

High Pressure Research, Mar2010, Vol. 30 Issue 1, p175-189, 15p, 4 Diagrams, 8 Charts, 5 Graphs
Graph; found on p184

How to Cite Images

When referencing images that come from articles, it is perfectly acceptable to cite the parent art

If you want to specifically cite the image, use the article citation and make the following changes

1. Check the article content for additional source information, such as a photographer or illustrator.
    - If an alternate name is available, use that in place of the article's author(s).
2. If the image has a title or caption, use that in place of the article title.
3. After the article or image title and before the journal title, insert the image type. Image types are: Chart, Diagram, Graph, Illustration, Map, or Photograph.

APPENDIX G

PERMISSION: FIG. 4.6

Licence number 3143800480039

Publication Zeitschrift für anorganische und allgemeine Chemie

Title Darstellung, 195Pt-NMR-, IR- und Raman-Spektren sowie Normalkoordinatenanalyse der Komplexionen $[PtH_nD_{6-n}]^{2-}$, n = 0–6

Author D. Bublitz,G. Peters,W. Preetz,G. Auffermann,W. Bronger

Volume/pages 623 184-190

Portion Figure 4

Type of use Dissertation/Thesis

Requestor type University/Academic

Format Print and electronic

APPENDIX H

PERMISSION: Li_2Al

This is a License Agreement between Kati Puhakainen ("You") and Elsevier ("Elsevier") provided by Copyright Clearance Center ("CCC"). The license consists of your order details, the terms and conditions provided by Elsevier, and the payment terms and conditions.

Registered Company Number 1982084

License number 3115481350118

Licensed content publisher Elsevier

Licensed content publication Journal of Solid State Chemistry

Licensed content title A new phase in the system lithium–aluminum: Characterization of orthorhombic Li2Al

Licensed content author Kati Puhakainen,Magnus Boström,Thomas L. Groy,Ulrich Häussermann

Licensed content date November 2010

Licensed content volume/issue/pages number 183,11, 2528-2533

Type of Use reuse in a thesis/dissertation

Portion full article

Format both print and electronic

Are you the author of this Elsevier article? Yes

Title of your thesis/dissertation In search of novel metal hydride materials using autoclave and multi-anvil hydrogenations

APPENDIX I

PERMISSION: Li_2PtH_6

Registered Company Number 1982084

License number 3115490091717

Licensed content publisher Elsevier

Licensed content publication Journal of Solid State Chemistry

Licensed content title Synthesis of Li_2PtH_6 using high pressure: Completion of the homologous seriesA_2PtH_6 (A=alkali metal)

Licensed content author Kati Puhakainen,Emil Stoyanov,Michael J. Evans,Kurt Leinenweber,Ulrich Häussermann

Licensed content volume/issue/ pages number 183, 8, 1785-1789

Type of Use reuse in a thesis/dissertation

Portion full article

Format both print and electronic

Are you the author of this Elsevier article? Yes

Title of your thesis/dissertation In search of novel metal hydride materials using autoclave and multi-anvil hydrogenations

APPENDIX J

PERMISSION: A_2SiH_6 (A = K OR Rb)

This is a License Agreement between Kati Puhakainen ("You") and John Wiley and Sons ("John Wiley and Sons") provided by Copyright Clearance Center ("CCC"). The license consists of your order details, the terms and conditions provided by John Wiley and Sons, and the payment terms and conditions.

License Number 3115480791286

Licensed content publication Angewandte Chemie International Edition

Copyright © 2012 WILEY-VCH Verlag GmbH & Co. KGaA, Weinheim

Licensed content title Hypervalent Octahedral SiH62− Species from High-Pressure Synthesis

Licensed content author Kati Puhakainen,Daryn Benson,Johanna Nylén,Sumit Konar,Emil Stoyanov,Kurt Leinenweber,Ulrich Häussermann

Licensed content /issue/ pages number 51, 3156-3160

Type of use Dissertation/Thesis

Requestor type Author of this Wiley article

Format Print and electronic

Portion Full article